9

Quantum Metrology

Editors: Richard E. Harris and Jürgen Niemeyer

9.1 Introduction

Richard E. Harris and Jürgen Niemeyer

As thorough readers of this book have begun to discover by this chapter on metrology, the most widely used applications of superconducting electronics involve measurements of electromagnetic phenomena. Unlike most other phenomena used for measurements, superconductivity is also essential for electrical *standards*. Because it is a quantum phenomenon, it can represent voltage in terms of fundamental constants with an amazing precision of a few parts in 10^{19}. In some regards superconducting voltage standards based on arrays of Josephson junctions are the most successful application of superconductivity, considering the numbers of junctions and their worldwide use. While they are conceptually simple, it has taken almost 50 years for their underlying technology to progress from unreliable single junctions to robust, complex, three-dimensional integrated circuits having more than 300,000 junctions and producing precision ac voltages up to 10 V. Here is their story.

As described in other chapters of this book, centimeter-sized superconducting loops can carry a

constant current that remains undiminished for many months or years with no sign of decline. This is a tangible manifestation of a macroscopic quantum state like only a few others in modern physics.

Within the wave function of the superconductor lies the key to using superconductors as voltage standards having incredible precision. While a macroscopic superconductor usually excludes magnetic fields, applying a large enough magnetic field causes magnetic flux to penetrate the superconductor in the form of flux bundles (Type I superconductors) or even tiny flux quanta (Type II superconductors) by destroying the superconductivity in localized regions. These normal regions co-exist with the surrounding superconductor. However as one traces a closed path through the superconductor, and around a normal region, the phase of its wave function must return to the same value plus perhaps a multiple of 2π. If the multiple is one, the normal region contains one flux quantum, Φ_0 or $h/2e$, where h is Planck's constant and $2e$ is the charge of each pair of electrons in the superconductor.

What we find is a remarkable, naturally occurring system of tiny, precisely identical magnets — the flux quanta. If we can manipulate them, we can for example induce voltages in an electrical circuit. The voltage pulse V induced by n flux quanta is

$$V = \frac{d\Phi}{dt},$$

where Φ is the flux inserted into the circuit, and the time-integral of the voltage across the circuit is

$$\int V(t)dt = n \cdot \frac{h}{2e}.$$

The flux quantum $h/2e$ has the value $2.067833667 \times 10^{-15}\mathrm{V}\cdot\mathrm{s}$.[1]

The flux quanta can be coerced into behaving just like a microscopic electrical generator. The difficulty lies in learning how to controllably manipulate them. The method that has been used is to interrupt a superconducting circuit with a weakened region. A flux quantum can be pushed across the weakened region by putting a current, having just the right amplitude, through the weakened region.[2]

Most practical devices now use lithographed Josephson junctions, but other weakened regions have also been used, such as point contacts and lithographed weak links. Sometimes the junctions are interrupted by a normal metal barrier and sometimes by an insulating one.

Even in his original announcement of his discovery of the Josephson effect in 1962, Brian Josephson anticipated voltage standards.[3] But as early experimentalists quickly discovered, a single flux quantum produces a very small voltage pulse. Using a current to force through one flux quantum with each oscillation of a 10 GHz ac current — that is, 10 billion exactly quantized voltage pulses per second — produces a time-averaged dc voltage of only about 20 μV, a value far too small to be useful directly in calibrating typical electrical devices that operate at multiples of one volt.

In the earliest voltage standards, metrologists took advantage of constant voltage steps in the current-voltage characteristics of Josephson junctions that occurred at integral multiples n of $hf/2e$ when driven by an ac current of frequency f. The steps occur when the microwave drive pushes through n quanta in a single period. Looked at a bit more closely, a change in the bias current at the nth step and the nonlinearities in the junction generate the nth harmonic of the microwave supply. Each cycle of that harmonic drove one flux quantum through the junction, giving a total of n

[1] P. J. Mohr, B. N. Taylor, and D. B. Newell, *Rev. Mod. Phys.* 80 (2008) 633. It is illustrative of the care with which metrologists work that the uncertainty in this value is only $0.000000052 \times 10^{-15}\mathrm{V}\cdot\mathrm{s}$. How this uncertainty may change in meaning and value over the second hundred years of superconductivity is difficult to imagine.

[2] Using flux quanta to explain the generation of quantized voltage has not been common in metrology, although Anderson used it to explain the voltage across bulk superconductors. Instead, metrologists have used the simple solution of nonlinear differential equations because they are quantitative and calculable even though perhaps a less intuitive explanation.

[3] B. D. Josephson, *Phys. Lett.* 1 (1962) 251

flux quanta in one cycle of the microwave source. The largest multiple of n that could reliably be achieved was about 250 flux quanta per oscillation of the microwaves. This produced a quantized voltage of about 5 mV. Even with this convenient multiplication of about 250, to compare this precision voltage to practical voltages often required the use of two junctions and a room-temperature bridge called a Hamon network. While single- or double-junction voltage standards of this sort were the state of the art for about a decade, the junctions often failed when cooled to liquid helium temperatures, or warmed back up, and the bridge was susceptible to errors.

It took only a high school education to feel tantalized by the prospect of directly creating higher precision voltages by putting many junctions in series. Unfortunately, that was not easy. It appeared that to create a one volt standard would require hundreds or thousands of junctions. At the time the arrays of junctions did not have sufficient uniformity to be biased by a single source of current. In an impressive effort in 1983, Endo and his colleagues in Japan succeeded in independently biasing 20 junctions in series to create 0.1 volt, as he relates in the next section of this chapter.

A major breakthrough came with lithographic fabrication and robust niobium trilayer junctions. For voltage standards, the levels of integration are still much lower than in semiconductor circuits, but have progressed from a one volt standard having 1500 junctions in 1985 to 300,000 junctions stacked three-high in 2010.

There are now three generations of standards based on arrays. The earliest produced only dc voltages but have progressed from 1 to 10 volt. For these standards, flux quanta were driven at precisely regular intervals through each junction in the array by use of a precision microwave source.

These dc standards were in routine use in standards laboratories beginning in 1985. Many are still functioning today. One that began at Hewlett-Packard's instrument division in Loveland, Colorado still functions in Indonesia in the relocated surviving company Agilent.

Because it was difficult to change the voltage of these arrays, clever people figured out how to produce arrays divided into segments having a binary distribution of numbers of junctions, so that sequentially turning on, and off, the right combination of segments could produce different voltages sufficiently fast for stepwise synthesis of frequencies as high as the kilohertz range. These "programmable" standards required new junction technologies using SINIS (superconductor-insulator-normal-insulator-superconductor junctions in Germany) and SNS (superconductor-normal-superconductor in the USA) to eliminate hysteresis and allow rapid controlled switching. Now these devices are being used for electric power standards.

Nevertheless quantum-based ac standards for synthesizing even higher frequencies required a new concept[4] that was not invented until 1995. In these standards, flux quanta are driven across each junction in a series array by the use of pulses of current. When the pulses recur rapidly, the voltage produced is high; when they recur slowly the voltage is lower. But the voltage is precisely proportional to the rate of pulsing. These standards are not yet in such widespread use as the dc and programmable ones, but as their technology advances, they offer the laboratory-demonstrated promise of a single technology for all quantum voltage standards.

All three types of standards are based on precisely manipulating the flow of flux quanta. Overcoming the technical challenges of superconducting integrated circuit fabrication, carefully designing their microwave properties, and developing easy-to-use room temperature controls has been research that spans fundamental science and practical engineering. The editors of this chapter were lucky enough to lead the two most successful laboratories in developing the technology, Harris at NIST Boulder[5] and Niemeyer at PTB Braunschweig[6]. Indeed the creation of the first one-volt stan-

[4] Ironically, it may be that delay in inventing ac standards had its roots in the common use of differential equations that obscured the intuitive physical ideas about flux motion that were essential to the invention of ac standards. Others believe that the delay resided in the technical difficulty of generating accurately timed pulses.

[5] NIST is the National Institute of Standards and Technology, USA. It was formerly named the National Bureau of Standards (NBS).

[6] PTB is the Physicalisch-Technische Bundesanstalt, Germany

dard was possible only because of an exceptionally successful collaboration between the two institutions that Niemeyer began by visiting NIST for six months in 1982. Unbeknownst to Niemeyer was that his determination to use NIST Boulder lithographic tools for voltage standards broke the institutional tradition that only NIST Gaithersburg worked on voltage standards. At NIST, one of the first contributions of the then-new array standard was to provide a method of verifying the accuracy of the Hamon network, and an error was found. Later NIST and PTB sometimes worked separately but collaborations recurred as new generations of voltage standards were created. Niemeyer's world travels also included ETL[7]. That laboratory also collaborated with NIST. Curiously there were striking differences among approaches to technology at NIST, PTB and ETL. NIST created fabrication technology cheaply, buying used equipment. ETL invested heavily in fabrication to participate in an attempt to construct a Josephson junction computer, although that facility was not initially available for voltage standards. PTB invested in a large clean room for fabrication in 1990. NIST will open a major fabrication facility facility in Boulder in 2012, twenty-two years later.

This section of *100 Years of Superconductivity* contains recollections of some of the pioneers in this technology. Shen Tsai and Jim Lukens tell about the incredible ultimate precision of voltage measurements. Tom Witt relates the experience of introducing the first standard measurement in national measurement institutes. Later in Japan the first arrays, independently biased, were demonstrated by Tadashi Endo. Jürgen Niemeyer describes creating the first singly biased, array as part of his close partnership between PTB and NIST in the US. Attention then turned to more widespread use of arrays as told by Clark Hamilton, a story of great international technological progress, but alas marginal commercial profitability. Subsequently programmable standards were developed as related by Johannes Kohlmann. Most recently Josephson arrays have been used in ac voltage standards and applied to a primary temperature standard that is elecctronically determined through Johnson noise thermometry, as related by Sam Benz. Finally, using large equipment one- to two-stories tall, to complement the tiny Josephson junctions, Ed Williams and Ian Robinson relate their efforts to use superconductivity and Josephson junctions to bring precision electrical measurements to the mechanical units.

This is a story of the second fifty years of superconductivity. It is a story of the technology of the ubiquitous semiconductor industry permeating the field of superconductivity and making remarkable progress possible. It leaves us barely able to fantasize what the next 50 and 100 years will bring.

9.2 Josephson Voltage Standard — The Ultimate Precision

Jaw-Shen Tsai and James E. Lukens

A voltage standard utilizing Josephson junction arrays has been adopted as an effective and convenient international standard for many years. Using specially designed cryogenic chips, laboratories around the world can reproduce voltage consistently with an accuracy of about few parts in a hundred million. The physics behind this standard is based on a very simple relation,

$$V = \frac{h}{2e} f, \tag{9.1}$$

between two macroscopic quantities: the average voltage V (electrochemical potential difference) across the junction and the frequency f of the Josephson oscillation. $h/2e$ is a quantum mechanical

[7] ETL is the Electrotechnical Laboratory, Japan. It is now named AIST, National Institute of Advanced Industrial Science and Technology.

fundamental constant, where h is the Planck constant and e is the electron charge in vacuum. In other words, it equates the quantum energy hf and the classical electrostatic energy $2eV$, both associated with the Cooper-pair dynamics.

In the voltage standard, the Josephson oscillation of relation (9.1) is phase locked to an external microwave signal of frequency f, creating a Shapiro step[8] with voltage V (at the first harmonic). The approximate 10^{-8} accuracy of the voltage standard is limited by the uncertainty in the experimental determination of the quantum mechanical constant. However, there is a more fundamental question: If the fundamental constant is supposedly given with infinite accuracy, do two different Josephson junctions generate exactly the same voltage when they are driven by the same microwave frequency f, just as we expect all atoms of the same species to produce exactly the same energy eigenvalues?

To be sure, a Josephson junction is a complex macroscopic entity that consists of an enormous number of atoms, and it is possible to realize it by very different junction types (i.e., superconductor-insulator-superconductor tunnel (SIS) junctions, superconductor-normal conductor-superconductor (SNS) junctions, superconducting microbridges, and so on) and very different materials. Can such macroscopic solid state devices really behave just like microscopic quantum systems?

Theoretically, the Josephson voltage-frequency relation given above has no known corrections, which is actually quite an extraordinary statement considering the complexity of the Josephson junction. Various arguments based on different physics have pointed out the exactness of this relation, such as arguments based on the fundamental quantum mechanical consideration[9], Faraday's law[10], the exactness of gauge invariance[11], and the topological quantum number[12].

To verify experimentally the extent of the universality of the Josephson voltage-frequency relation, we have carried out a high precision comparison of Josephson voltages created in two different junctions.[13] Such a test has three-fold meaning. Scientifically, it is quite interesting to test how exactly such a macroscopic system behaves according to a quantum mechanical relation (Josephson relation). Technologically, such a test should provide a "confidence assessment" of the ultimate accuracy of the Josephson voltage standard. At the same time, in metrology, to establish a high-precision measurement of a unique physical quantity is always a fascinating subject.

The experimental test was carried out by the use of a circuit set up as a dc superconducting quantum interference device (SQUID) that consists of two Josephson junctions to be compared, imbedded in a superconducting loop. Both Josephson junctions were biased by dc and ac (microwave frequency), and parked near the center of a certain harmonic of the Shapiro constant voltage step for both junctions. At Shapiro steps, the voltages across the junctions are $V = nhf/2e$, where n is the number of the harmonic.

We irradiated both junctions with the same microwave frequency f, generated from a frequency stabilized microwave source, typically at about 10 GHz. Now, suppose Eq. (9.1) is not exact, and at the two junctions, different electrochemical potential differences $V1$ and $V2$ resulted. Then the difference in these, $\Delta V = V1 - V2$, would produce a time varying flux in the superconducting loop, following Faraday's induction law:

$$\Delta V = \frac{d\Phi}{dt}.$$

By monitoring the flux, Φ, linking the SQUID, ΔV can then be detected. This method of comparison was first demonstrated by Clarke.[14] By adopting and improving this experimental scheme, we

[8] S. Shapiro, *Phys. Rev. Lett.* 11 (1963) 80
[9] F. Bloch, *Phys. Rev.* B2 (1970) 109
[10] T. A. Fulton, *Phys. Rev.* B7 (1973) 981
[11] D. G. McDonald, quoting P. W. Anderson, *Physics Today* (July 2001) 46
[12] David J. Thouless, *Topological Quantum Number in Nonrelativistic Physics*, World Scientific, Singapore (1998)
[13] J. S. Tsai, A. K. Jain, and J. E. Lukens, *Phys. Rev. Lett.* 51 (1983) 316
[14] J. Clarke, *Phys. Rev. Lett.* 21 (1968) 1566

have succeeded in achieving an unprecedentedly high precision for Josephson voltage comparison. We monitored Φ using an rf SQUID, which was coupled to the system by a superconducting flux transformer.

The potential sensitivity of the voltage comparison scheme can be estimated as follows. When biased at a voltage step of $V = 1\ \mu$V, and assuming the integration time Δt of the flux to be 1 hour, and the flux noise of the SQUID to be $\Delta\Phi = 10^{-4}\Phi_0$ during this time interval (Φ_0 is the flux quantum), then the resolution of the voltage comparison,

$$\frac{\Delta V}{V} = \frac{\Delta\Phi}{\Delta t \cdot V},$$

will be of the order of 10^{-16}. This simplified estimation illustrates the powerful prospects for this experimental technique.

It is desirable to dc bias the two Josephson junctions at the highest possible Shapiro step (on the same harmonic for both junctions) in order to obtain the highest ΔV for a given $\Delta V/V$ ratio. To do so, it is important to make the properties of the two junctions, such as critical current and normal resistance, as symmetrical as possible. For the same reason, the inductance of two arms of the SQUID, L1 and L2, should be made as symmetrical as possible. In this way, the dc current bias would divide equally into two arms so that it is possible to bias the two junctions at the same (and as high as possible) harmonic order of the Shapiro step while reducing noise due to bias drift.

Another important factor to assure a high precision in the experiment is to secure a long integration time Δt. To do so, the most important factor is to maintain the temperature throughout the experiment as constant as possible, since temperature variations could result in variations in the I-V characteristics that would shift the dc bias point off the Shapiro step, terminating the experiment or, at a minimum, increase the flux noise. It could also cause thermoelectric effects that bring about shifts in Φ or cause phase shifts between the two microwave lines that connect the two junctions, also resulting an undesired shift in Φ.

In the experiment, we phase-locked the junctions on the microwave step, and the output of the rf SQUID was monitored for many hours with a 0.01 Hz time constant. The microwave frequency used was 18 GHz in all cases[13]. Several different types of Josephson junctions were used in the comparison experiments. In comparing two indium microbridges, we were able to bias them at the tenth harmonic step, and verify that the Josephson voltages of the two junctions were equal with a precision, $\Delta V/V$, of $\approx 5 \times 10^{-18}$. For measurements comparing an indium microbridge and a planar niobium/copper/niobium (superconducting/normal/superconducting) junction, because of the much worse symmetry in the two junctions' parameters, the bias was limited to the first step, which resulted in a slightly reduced precision limit: $\approx 2\times10^{-16}$. This result indicated that Eq. 9.1 does not have noticeable material[15] or junction-type dependences. Later, work by others using a similar technique demonstrated that the Josephson junction arrays that are actually used for the real voltage standards

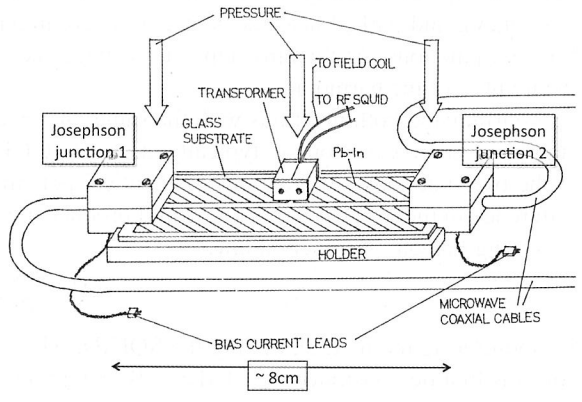

FIGURE 9.1: Schematic of the DC SQUID used for voltage comparison.

[15] K. Nordtvert, *Phys. Rev.* B1 (1970) 81; later theoretically refuted by D.N. Langenberg et al., *Phys. Rev*. B3 (1971) 1776, and J. B. Hurtle et al., *Phys. Rev.* B3 (1971) 1778

produce identical voltages with a precision[16] of $\approx 2\times10^{-17}$. Additional later investigations comparing array accuracy were carried out at PTB.[17,18]

We later compared two very similar lead tunnel junctions, further improving the precision limit[19] to $\approx 3\times10^{-19}$. Since the gravitational red shift in f between two junctions with a vertical separation of about $z = 3$ mm would also be $\approx 3\times10^{-19}$, it would be interesting to see whether one should be concerned with this effect. To test this, we made a SQUID where $z = 70$ mm. We again obtained a null result. This is expected because it is the gravito-electrochemical potential, rather than the electrochemical potential, that should be constant along a superconducting wire, just canceling the effect of the red shift. To our knowledge, this was the first confirmation of this effect.

This series of experiments established the ultimate precision of the voltage standard based on Josephson junctions. No significant dependence on material or type of the junction was found. These results show that we can reproduce the voltage within the accuracy associated with the frequency of the microwave source. It can be understood that in such Josephson junctions, most of the degrees of freedom of conducting electrons are frozen into just one quantity, the macroscopic phase difference of order parameter across the junction. Even with the surrounding quasiparticles, the resulting superconducting state is immune to dissipation and follows the relation (9.1) exactly. The equality established here for Josephson voltage is probably one of the most accurately determined equalities among all the known physical equalities. Although microwave-induced Shapiro steps are dynamical states and not energy eigenstates, the universality of the quantized energy value in this macroscopic system was established with extraordinary accuracy, much better than that confirmed in microscopic systems, such as comparison of atomic levels in two atoms. The work described in this article took place when Tsai was a student of Lukens at the State University of New York, at Stony Brook. Both comment on their personal experiences.

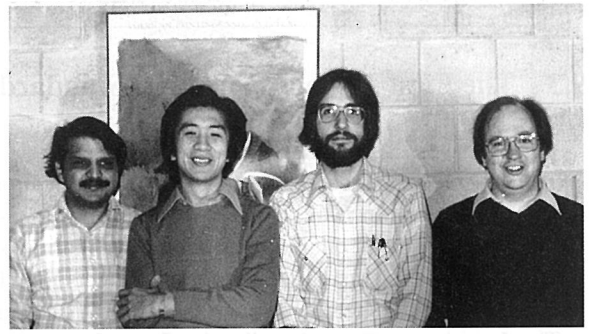

FIGURE 9.2: The group at Stony Brook in about 1983: Aloke Jain, Shen Tsai, Joe Sauvageau, and Jim Lukens.

Lukens: I started thinking about using SQUIDs to detect gravitational effects when I was still working on my thesis in 1966. So, it was very exciting when we finally achieved the sensitivity required for such measurements while testing the universality of the Josephson frequency-voltage relation and were then able to demonstrate that, assuming the gravitational red shift of photons, it was indeed the gravito-electrochemical potential rather than the electrochemical potential that was constant in the superconducting leads of the SQUID.

Tsai: I wrote the draft of this article while trapped in Helsinki Airport for a very long time, due to the eruption of Icelandic volcano Eyjafjallajökull. As I was writing it under a rather unpleasant circumstance, all the excitements and frustrations that took place about 30 years ago came back to me. The experiment was originally designed to observe the gravitational red shift using a SQUID. For this reason, to maximize the signal, the SQUID loop had an unusually large dimension: about 8 cm in length. The idea of the "desktop" gravitational effect experiment really fascinated me in spite

[16] R. L. Kautz and F. L. Lloyd, *Appl. Phys. Lett.* 51 (1987) 2043

[17] J. Niemeyer, Grimm, C. A. Hamilton, R. L. Steiner, *IEEE Electr. Dev. Lett.* EDL-7 (1986) 44

[18] J. Y. Krasnopolin, R. Behr, and J. Niemeyer, *Supercond. Sci. Tech.* 15 (2002) 1034

[19] A. K. Jain, J. E. Lukens, and J. S. Tsai,*Phys. Rev. Lett.* 58 (1987) 1165

of its difficulty. From the null result obtained, we were able to demonstrate the importance of the gravito-electrochemical potential in the superconductor, in addition to the red shift. That is, in the superconductor, it is the gravito-electrochemical potential that is constant, not the electrochemical potential, as usually described in textbooks. In addition to this, as a grand bonus, we were also able to establish the universality of the Josephson frequency-voltage relation with an unprecedentedly extraordinary accuracy. All these took place in the beginning of my long low-temperature-physicist career, while working as a graduate student. Looking back now, I consider myself very fortunate to have been able to work on such challenging and rewarding topics in Jim Lukens's laboratory.

9.3 The First Josephson Voltage Standards

Thomas J. Witt

The Josephson effect is the most fruitful application of superconductivity in metrology (measurement science). In 1962, Brian Josephson, then a 22-year-old graduate student, predicted several phenomena caused by quantum mechanical tunneling of paired electrons through an insulating barrier.[20] In classical physics such tunneling effects may be compared with throwing a ball against a wall and seeing it penetrate through the wall rather than bouncing back.

The Josephson effects describe the flow of current through a Josephson junction consisting of two superconductors separated by a weak link such as a thin (order of 1 nm) insulating barrier. A bulk superconductor can often be described by a "wave function" characterized by a single phase, ϕ_1. Josephson predicted that even in the absence of an applied electromagnetic field a steady supercurrent $I = I_c \sin\phi$ would flow between the superconductors on each side of the barrier, forming a Josephson junction (the dc Josephson effect). ϕ is the difference in phase between the wave functions on the two sides of the barrier. The time dependence of ϕ is given by $\partial\phi/\partial t = (2e/\hbar)V(t)$ where e is the elementary charge, $\hbar$ is the Plank constant divided by 2π and $V(t)$ is the voltage across the junction. The application of a steady voltage V_{dc} across the junction results in the flow of an ac current of frequency $(2e/h)V_{dc}$ (ac Josephson effect). Moreover, superimposing an alternating voltage of frequency f on an applied direct voltage, the ac supercurrent is modulated. This results in constant-voltage steps at integer values $V_n = nhf/2e = nf/K_J$. n is an integer and K_J is the Josephson constant (defined as $2e/h$).

The first observation of the dc Josephson effect was reported in 1963. An account of Josephson's work and of this observation is given by Anderson.[21] Shapiro was the first to observe constant voltage steps produced by irradiating a tunnel junction with microwaves.[22] From 1965 until the early 1970s the group led by D. N. Langenberg at the University of Pennsylvania (Penn) made major contributions to the development of the use of the Josephson effect to measure *2e/h*, to access the impact of their determinations on the ensemble of fundamental constants, and to develop the Josephson effect as a voltage standard. By 1966 they had tested the Josephson frequency-to-voltage relation to 60 parts per million (ppm). In 1967 the Penn group announced a determination of *2e/h* with an uncertainty of 6 ppm and discussed the impact of this new way to measure *2e/h* on other constants.[23] In particular, they deduced a value of the fine structure constant α that was lower than the accepted value of the time. Using the Josephson-effect value of α resolved a 43 ppm discrepancy between the experimental value of the hyperfine splitting in atomic hydrogen and the theoretical value derived

[20] B. D. Josephson, *Phys. Lett.* 1 (1962) 251
[21] P. W. Anderson, *Phys. Today* 23 (1970) 23
[22] S. Shapiro, *Phys. Rev. Lett.* 11 (1963) 80
[23] W. H. Parker, B. N. Taylor and D. N. Langenberg, *Phys. Rev. Lett.* 18 (1967) 287

from quantum electrodynamics. Also that year the Penn group proposed to the metrology community that the ac Josephson effect could be used to maintain standards of electromotive force with an uncertainty of 1 ppm or less.

To illustrate the importance of this, I first describe the limitations of the voltage standards of the time as well as the methods and limitations of the Josephson measurements. In the Système International d'Unités (SI), the modern form of the metric system of units, the base unit for electricity is the ampere, defined by the force between idealized current-carrying wires. The volt, the unit of voltage or electrical potential difference, is derived from the ampere by assuming the equivalence of electrical and mechanical energy. Nearly all voltage measurements reduce to the determination of the ratio of an unknown voltage to some reference voltage (often incorporated in the measurement instrument itself). Calibrations of reference voltages are traceable to the volt. Determinations of the volt were, and still are, difficult to carry out. In 1967 they were limited in uncertainty to a few ppm or more. (This story is brought up to date in the article in this chapter by E. Williams and I. Robinson).

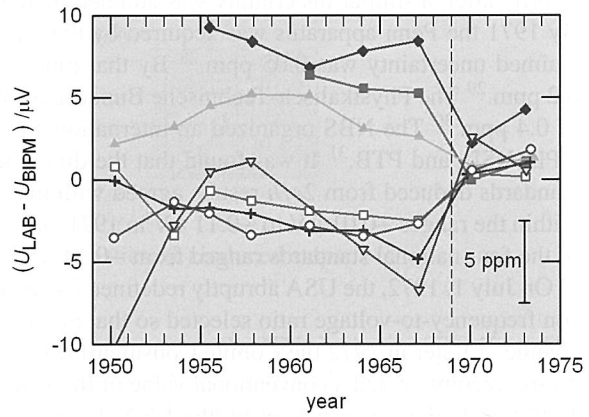

FIGURE 9.3: Comparisons of voltage standards of 7 national laboratories 1950–1973.

Until the early 1970s, voltage standards were maintained in national metrology institutes (NMIs) using groups of Weston standard cells (precision electrochemical cells). Each national group had a somewhat different value of voltage. International traceability was established by periodic comparisons at the Bureau International des Poids et Mesures (BIPM). Figure 9.3 shows the results of these comparisons between 1950 and 1973. Standard cells were only *representations* of the volt (as is the Josephson voltage standard today); their values in SI volts were traceable to determinations of the SI volt. The electromotive force of a standard cell (emf) is the difference in electrical potential between its terminals when no current flows. Standard cells suffer serious stability limitations: large temperature coefficients, sensitivity to shock, drift of electromotive force (emf) in time, occasional small spontaneous changes of emf and sensitivity to accidental charge or discharge. For the international comparisons, standard cells were hand-carried to the BIPM.

For all these reasons NMIs were particularly keen to explore the possibility of using the Josephson effect as a voltage standard. A major challenge in 1967 was the fabrication of adequate Josephson devices. Even good Josephson devices produced output voltages less than 800 μV. An uncertainty of 1 ppm represented only tenths of a nanovolt. To compare such voltages with the emf of a standard cell, a resistance ratio network was needed. Such networks were major sources of measurement uncertainty. The resolution of the voltage detector was of the order of 1 nV. The thermal emfs in the leads from the He cryostat to the room-temperature measurement system should be small in magnitude and stable in time. Since about 1970, little progress has been made to diminish the absolute values of the latter two limitations. Fortunately, the development of large arrays of Josephson junctions[24] (also see other contributions in this chapter) has resulted in the increase in output voltage to 10 V today, reducing an uncertainty of, say, 0.5 nV to a relative uncertainty with respect to the output of 5 parts in 10^{11}. This is roughly the present-day relative uncertainty in the direct comparisons of 10 V Josephson standards. At such output levels a resistance ratio network is not needed.

[24] C. A. Hamilton, *Rev. Sci. Instrum.* 71 (2000) 3600

By 1969 the Penn group achieved a 2.4 ppm uncertainty in $2e/h$ measurements. The same year, the National Physical Laboratory (NPL), UK, announced a measurement of $2e/h$ with an uncertainty of 2.2 ppm and became the first NMI to carry out high-accuracy Josephson measurements.[25] The following year the Penn group announced the first $2e/h$ measurement with sub-ppm uncertainty.[26] Shortly after, a similar uncertainty was attained by the National Standards Laboratory, Australia.[27] By 1971 the Penn apparatus was acquired by the National Bureau of Standards (NBS), USA; the claimed uncertainty was 0.05 ppm.[28] By that time the uncertainty of the NPL measurement was 0.2 ppm.[29] The Physikalisch-Technische Bundesanstalt (PTB), Germany, announced an uncertainty of 0.4 ppm.[30] The NBS organized an international comparison of voltage standards that included NPL, NSL, and PTB.[31] It was found that the differences among the participants' national voltage standards deduced from $2e/h$ results agreed with the differences found via traveling standard cells within the ranges +0.01 μV to −0.11 μV in 1971 and −0.08 μV to −0.38 μV in 1972. The drift rates of the four national standards ranged from −0.14 μV/yr to −0.31 μV/yr.

On July 1, 1972, the USA abruptly redefined its voltage standard in terms of a value of the Josephson frequency-to-voltage ratio selected so that no discontinuity in value occurred on the day of the change.[32] Later in 1972 the Comité Consultatif d'Electricité (CCE), an organ of the Convention du Métre, recommended a conventional value of the Josephson frequency-to-voltage quotient that was 1.20 ppm higher than that set by the USA. Eventually most other nations redefined their voltage standards to be in agreement with the CCE's recommended conventional value, with two other exceptions: France and the USSR. This unfortunate situation lasted until January 1, 1990, when it was universally agreed to apply a new conventional value of the Josephson frequency-to-voltage quotient $K_{J-90} = 483597.9$ GHz/V with an assigned uncertainty of 0.4 ppm.[33] At the time this value was considered to be the best estimate of $2e/h$ expressed in SI units (i.e., traceable to mechanical energy). Notwithstanding progress in the determinations of e and h over the last 20 years, K_{J-90} is consistent with the present estimate of K_J in SI units. K_{J-90} is still used to assign values to the representations of the volt based on the Josephson effect.

My experience with the Josephson effect began in 1969 at the NBS. In 1971 I accepted the job of establishing a Josephson standard at BIPM. I built a voltage comparator based on that of the Penn group. In 1973 Dominique Reymann joined the BIPM Josephson volt project. Our most formidable remaining task was to use makes provided by the NBS to fabricate tunnel junctions capable of producing a 10 mV output. Figure 9.4(a) is a photograph of a 25.2 mm square substrate carrying four Pb-Pb oxide-Pb tunnel junctions connected in series to produce a 10 mV output; (b) is a sketch of the current-voltage characteristics: $I_c = 10$ mA, the voltage $E_g/2e$ gives the value of the energy gap in Pb, ≈ 2.8 mV; and (c) shows a zoomed photograph of the constant voltage steps near 4.5 mV when a junction is irradiated at 9.1 GHz.

By 1975 we had achieved an accuracy of 6 parts in 10^8 in the measurement of $2e/h$ in terms of the BIPM voltage standard. To support this uncertainty claim we transported our entire Josephson system to the PTB and compared the results of our on-site Josephson measurements of standard cells with those of the PTB. The results gave a difference of 5 parts in 10^8 with a combined standard

[25] B. W. Petley and K. Morris, *Phys. Lett.* A 29 (1969) 289

[26] T. F. Finnegan, A. Denenstein, D. N. Langenberg, *Phys. Rev. Lett.*, 24 (1970) 738

[27] I. K. Harvey, J. C. Macfarlane and R. B. Frenkel, *Phys. Rev. Lett.* 25 (1970) 853

[28] T. F. Finnegan, T. J. Witt, B. F. Field and J. Toots, in *Atomic Masses and Fundamental Constants* 4, J. H. Sanders and A. H. Wapstra, Eds., New York, Plenum (1972) 403

[29] J. C. Gallop and B. W. Petley, *Metrologia* 8 (1972) 129

[30] V. Kose, F. Melchert, H. Fack and H.-J. Schrader, *PTB Mitt.* 81 (1971) 8

[31] W. G. Eicke, B. N. Taylor, *IEEE Trans. Instrum. Meas.* IM-21 (1972) 316

[32] B. F. Field, T. F. Finnegan and J. Toots, *Metrologia* 9 (1973) 155

[33] B. N. Taylor and T. J. Witt, *Metrologia* 26 (1989) 47

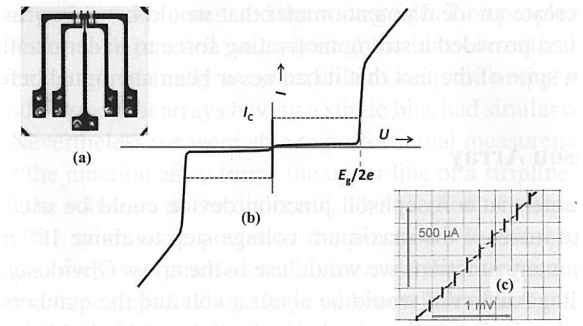

FIGURE 9.4: (a) Tunnel junctions; (b) dc characteristics; (c) induced steps.

uncertainty[34] of 6 parts in 10^8. We transported our equipment to the NPL in April 1978 where for the first time we compared Josephson voltage standards directly, bypassing the use of standard cells and found a difference between our voltage standards of (9 ± 5) parts in 10^8. This was the beginning of an ongoing series of BIPM on-site comparisons of Josephson standards that continues to this day. The later comparisons were carried out at 1 V and eventually at 10 V using arrays of Josephson junctions. Also in 1978, the ETL Japan, announced achieving outputs of 100 mV using arrays of junctions. That story will be related by Tadashi Endo in the following section.

9.4 First Josephson Junction Array Voltage Standard

Tadashi Endo

9.4.1 Introduction

In 1977 at Japan's Electrotechnical Laboratory (ETL),[35] we fabricated and began using a two-junction Josephson voltage standard. Our standard produced a maximum voltage of 12 mV using a 10 GHz microwave source. To compare this small voltage with typical calibration voltages of about 1 V, we used a precision resistance bridge between the standard and the source we wished to calibrate. As a result the voltage could be determined only to 2 parts in 10^8 in spite of the perfect accuracy of the Josephson junctions themselves.[36] Other laboratories were similarly limited.

As a research project after the Josephson voltage standard was introduced, we decided to fabricate an array of Josephson junctions. This work took place between 1977 and 1983 and was primarily done by Tadashi Endo and Masao Koyanagi at ETL. The accuracy of any step voltage developed by a Josephson junction depends only on the relatively simple accurate measurement of the frequency of the microwaves applied to the Josephson junction. We planned to use this superior feature of the

[34] T. J. Witt and D. Reymann, in *Atomic Masses and Fundamental Constants* 5, J. H. Sanders and A. H. Wapstra, Eds., New York, Plenum, (1976) 457

[35] The Electrotechnical Laboratory was reorganized to the present National Institute of Advanced Industrial Science and Technology, Japan (AIST) in 2001.

[36] T. Endo, M. Koyanagi, K. Shimazaki, G. Yonezaki, and A. Nakamura, AMCO-5, *Atomic Masses and Fundamental Constants* 5, Plenum Press, New York (1976) 464

Josephson junction to create an ideal potentiometer that would have, in principle, perfect linearity. The device we envisioned provided a strong motivating force to undertake this development of the first Josephson array, in spite of the fact that it had never been attempted before.

9.4.2 First Josephson Array

In order to demonstrate that a Josephson junction device could be used as a potentiometer in practical use, we had to increase the maximum voltage step to above 100 mV at least.[37] Our first task was to decide how many junctions we would use in the array. Obviously if we could make, say, 1000 junctions, the voltage achieved would be about a volt and the cumbersome bridge would not be needed at all. However each junction needed to be independently biased with a dc current. At that time, junctions differed considerably and each needed a separate bias. We were limited by the practical difficulties of creating many working junctions in series with superconducting connections between them, by supplying microwave power uniformly to the junctions, and by the formidable task of adjusting the bias supplies that were as numerous as the junctions. Because we were obtaining 5 mV from each junction in our conventional standard, we decided that a reasonable choice was an array of 20 junctions.

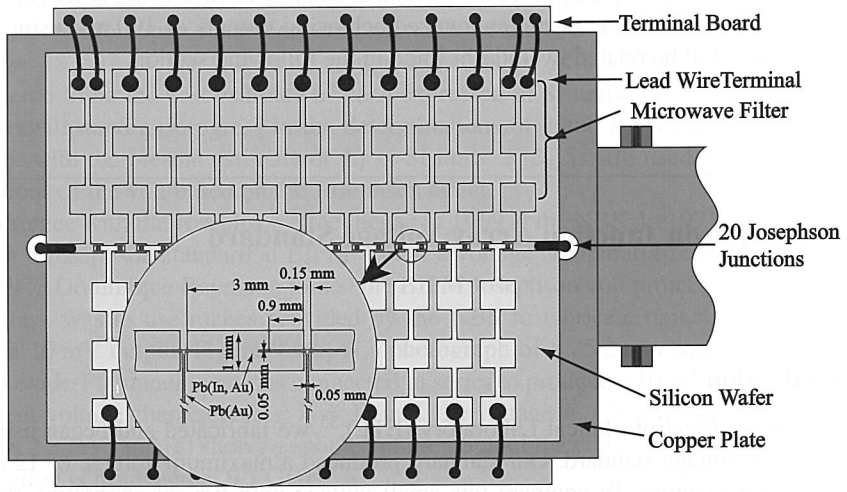

FIGURE 9.5: The multiple Josephson junction is composed of twenty Pb(In, Au)-oxide-Pb(Au) tunnel junctions constructed on the center superconducting strip film with 1 mm width. The overall pattern of the sample is made on a 0.2 mm thick silicon wafer by vacuum-evaporating the superconducting films and patterning them using photolithography. The size and the normal resistance of each tunnel junction are 0.9 mm × 0.05 mm and about 70 mΩ, respectively.

We developed what we called, when we spoke English, the "multiple Josephson junction" as shown in Figure 9.5, and obtained a maximum voltage greater than 100 mV. The array was fabricated in our simple facility that we built based on publications from IBM Research where they were attempting to fabricate a Josephson junction computer. We worked about three years to obtain the first usable 20-junction array in 1980. Then it was necessary to learn how to use it. When using the array we found that the shape of the I-V curve changed with the level of the liquid helium in the

[37] T. Endo, M. Koyanagi and A. Nakamura, *IEEE Trans. Instrum. Meas.* IM-32 (1983) 267

waveguide. To solve that problem we evacuated the waveguide. Two people operated the array: one monitored the I-V curves of each junction and adjusted the bias currents; the other performed the precise voltage measurements. Eventually we were able to keep the output voltage stable for about 15 minutes. Later we understood that arrays having a single bias had similar operational instabilities. (See the next section.) Nevertheless we were able to perform real measurements.

Figure 9.6 shows that the junction array forms the upper line of a stripline with the sample holder as the ground plane and the substrate as the dielectric. This method of microwave coupling allowed us to couple uniformly the microwave power to the junctions. It also enabled us to reduce the normal resistance of each Josephson junction and to increase the current width of the voltage step. For example, the largest voltage steps having a large current width of 200 μA to 300 μA appeared in the voltage range of 3 mV to 8 mV for each junction under microwave irradiation at 9.3 GHz with a power of 120 mW.

9.4.3 Applications of the Multiple Josephson Junction

In order to demonstrate that the multiple Josephson junction could be used practically as a Josephson potentiometer, we demonstrated its use for the following two precise measurements.

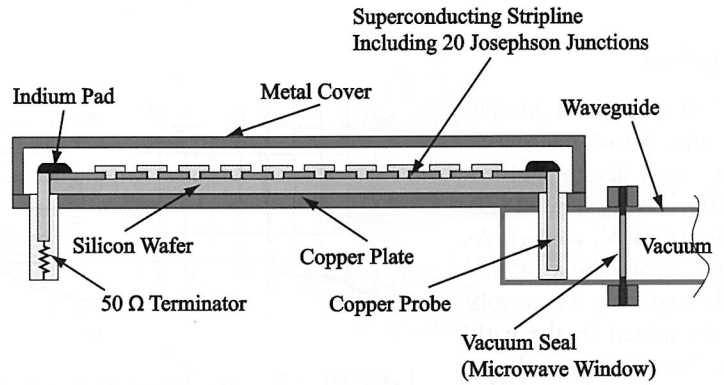

FIGURE 9.6: Cross-sectional view along the center strip film of the sample when the sample is mounted on the sample holder. A parallel plate type microwave stripline of 50 Ω is composed of the center superconducting strip film including the twenty junctions (which acts as the top electrode), the silicon wafer (which acts as the dielectric layer) and the copper plate of the sample holder (which acts as the lower electrode). A 10 GHz microwave source was coupled to the 50 Ω stripline from the waveguide through the copper probe. In order to irradiate all of the junctions by microwave as uniformly as possible, the end of the stripline was terminated by a 50 Ω resistance.

First we measured the emf (electromotive force) of a chemical standard cell using a voltage divider composed of ten 45 Ω resistors connected in series. We were able to confirm that the voltage of nominally 1 V could be measured with a relative uncertainty of 2.5×10^{-9}. Around 1982, this meant that the accuracy was increased by 1 order of magnitude compared with the 10 mV Josephson voltage standard at that time.

Second, we measured the fundamental quantity h/e^2. It was important because a resistance standard had been recently created, based on the quantum Hall effect, by defining the fundamental constant, named after von Klitzing, R_{K-90} ($\approx h/e^2$) with conventional value of $R_{K-90} = 25.812807\ k\Omega$

since January 1990. However, h/e^2 was the quantity to be measured in 1983.[38]

We succeeded in experimentally confirming that the resistance ratio between the fourth plateau of the quantum Hall effect and a 6.45 kΩ standard resistor could be measured with a relative uncertainty of about 1.1 x 10^{-8}. This is about the level of the thermal noise of the standard resistor but not of the Josephson potentiometer.

9.4.4 Conclusion

We demonstrated the multiple Josephson junction and its use as a potentiometer having ultimate linearity by increasing the Josephson step voltage to over 100 mV. If such demonstration would have led to the present Josephson junction array, it is our great pleasure. We are also pleased to note the major advances that have come after our work and are described in the following sections of this chapter on metrology.

9.5 How the DC Array Standards Were Developed

Jürgen Niemeyer

9.5.1 Introduction

By locking a current-driven Josephson junction to an external microwave source with a precisely determined frequency f, constant voltage steps appear in the dc characteristic at $V_n = n\Phi_0 f$. As this voltage is very small (about 145 μV for f = 70 GHz and n = 1), a voltage divider was required in the early days to enhance the reference voltages to the 1 V level for practical use. But the voltage divider limited the precision, and its handling was rather complicated. For these reasons, the advantage of the quantum origin of the voltage could not be fully exploited.

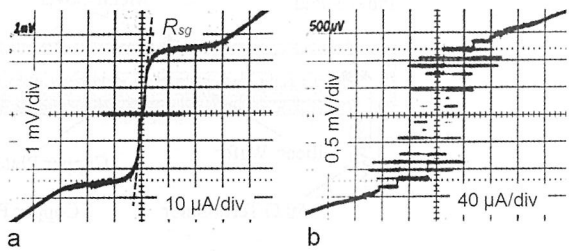

FIGURE 9.7: Dc characteristics of a Pb-alloy tunnel junction. a: without microwaves, b: under microwave radiation of 70 GHz. R_{sg} is the subgap resistance. The rf-power is optimized for the 7th step. The steps in the back-switching part of the dc characteristic cross the zero current axis.

Therefore, the idea developed over time to increase the output voltage by connecting a certain number of Josephson junctions in series. In the 1970s, most people found the idea of preparing arrays of thousands of junctions rather ridiculous because there was no reliable Josephson circuit technology available. Early experiments were therefore restricted to series arrays with a small number of individually biased junctions.

But at the beginning of the 1980s this situation began to change because important progress was achieved in the following fields:

1. IBM developed a Josephson circuit technology for digital computing that was based on lead alloy tunnel junctions, the barrier of which was formed by a plasma oxidation process.[39]

2. Mogens T. Levinsen and coworkers suggested making use of zero-current voltage steps for the realization of large commonly biased arrays.[40] In this way the inevitable junction parameter spread would no longer play an important role because the array could be biased at zero current. Also voltage steps up to the limit of about 1 mV per junction could be used, which considerably reduced the number of junctions for an array with a given output voltage. See Figure 9.7.

3. Tadashi Endo at the Electrotechnical Laboratory[41] (ETL) in Japan successfully operated a series array with 20 individually biased Josephson junctions that were located as an integrated part of a superconducting stripline with the substrate serving as the dielectric.[42] (See the preceding article by T. Endo.)

4. Richard Kautz at the National Bureau of Standards[43] (NBS) in Boulder, CO was working to understand why a 5,000 junction array that NIST fabricated showed no steps at all. Kautz' work threw light on the operating conditions for a chaos-free phase lock between an external microwave source and a Josephson tunnel junction with very low damping.[44] These calculations made it possible to design correctly the single rf-driven tunnel junction.

[38] T. Endo, Y. Murayama, M. Koyanagi, J. Kinoshita, K. Inagaki, C. Yamanouchi and K. Yoshihiro, *IEEE Instrum. Meas.* IM-34 (1985) 323

9.5.2 Single Junction Design

A Josephson junction can be considered a driven nonlinear current oscillator with damping. To obtain zero-current voltage steps one has to use tunnel junctions with very low damping. The mechanical analog of the Josephson oscillator is a driven pendulum in the gravitational field of the earth with viscous damping. In this analog, the external microwave source characterizes the driving force; the junction capacitance, the moment of inertia; the junction conductivity, the viscous damping; and the critical current, the torque in the gravitational field. If such a "pendulum" is to be coupled to an external oscillating "force" — a microwave oscillator — the oscillations easily become chaotic or even catastrophic if the external oscillation frequency approaches the resonance frequency of the Josephson "pendulum".

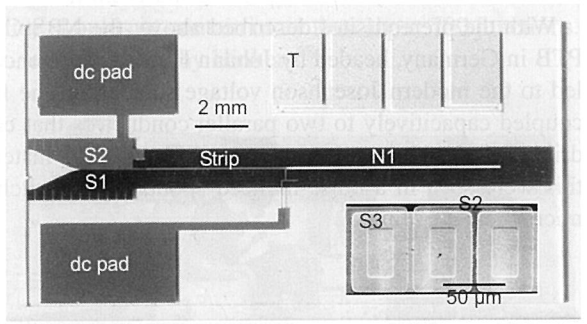

FIGURE 9.8: 102 junction array on a glass substrate. The insert shows 3 junctions of the array stripline. S1: groundplane; S2: base electrode layer; S3: top electrode layer; N1: matched load; T: test circuit for the matched load.

On the basis of the Stewart-McCumber junction model[45], Kautz found that for junctions with small damping, a chaos-free generation of constant voltage steps is possible only if the frequency of

[39] J. H. Greiner et al., *IBM J. Res. Develop.* 53 (1982) 326

[40] M. T. Levinsen, R. Y. Chiao, M. J. Feldman, B. A. Tucker, *Appl. Phys. Lett.* 31 (1977) 776

[41] The Electrotechnical Laboratory in Tsukuba, Japan, has become the National Institute of Advanced Industrial Science and Technology (AIST)

[42] T. Endo, M. Koyanagi, A. Nakamura, *IEEE Trans. Instrum. Meas.* IM-32 (1983) 267

[43] The National Bureau of Standards in the USA has become the National Institute of Standards and Technology (NIST).

[44] R. L. Kautz, *J. Appl. Phys.* 52 (1981) 35283541

[45] W. C. Stewart, *Appl. Phys. Lett.* 12, (1966) 277; D. E. McCumber, *J. Appl. Phys.* 39 (1969) 3113

the external microwave is larger than the resonance frequency of the Josephson junction oscillator. Together with the necessity of restricting the junction area for avoiding an inhomogeneous current distribution over the junction area by the magnetic field, particularly of the large rf-current and by rf-resonances inside the junction, the frequency condition determines a maximum value for the critical current. These restrictions are of great practical importance because they define a maximum current width of the constant voltage steps. The step current width should be as large as possible because the larger the steps are, the less sensitive they are to electromagnetic noise-induced spontaneous switching. At PTB in the 1970s, precision measurements with Josephson junctions often had to be performed during the night because of the reduced level of electromagnetic noise at that time. For typical lead alloy junctions with a maximum area of about 24 μm x 67 μm, the calculated optimum width of the seventh step amounts to about 220 μA, a size large enough for stable standard operation. For a driving oscillator frequency of about 70 GHz, the maximum zero current step voltage lies at the seventh voltage step, the current width of which is therefore a good criterion for the applicability of a certain junction technology for dc array standards.

In real arrays the resulting step width is much smaller than the optimum value for a single junction due to the parameter spread of the junctions and to noise-induced reduction of the step size. We had to learn that the smallest critical current of the array junctions determines the resulting step width. This and the chaos restriction of the maximum critical current made the parameter spread still play a certain role.

9.5.3 Circuit Design and First Realization

With the prerequisites described above, the NBS Cryoelectronics Section and my laboratory at PTB in Germany, headed by Johann Hinken, were encouraged to start the development that finally led to the modern Josephson voltage standards. The first NBS arrays consisted of 100 junctions, coupled capacitively to two parallel conductors that carried the rf-power of a 20 GHz microwave drive.[46] Steps were achieved up to only 27 mV, instead of the expected 80 mV. The reasons for this were seen in a noise-induced spontaneous switching between the steps and inhomogeneous microwave coupling.

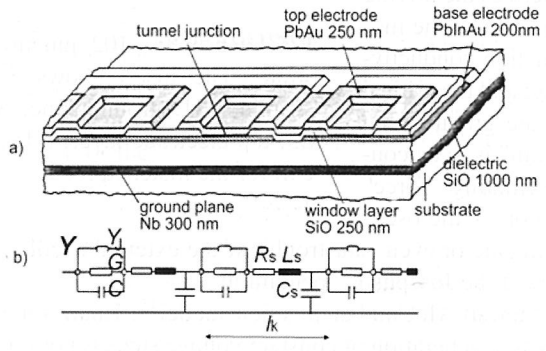

FIGURE 9.9: (a) Cross-sectional view of a portion of the 70 GHz microstripline with (b) the microwave equivalent circuit of the periodic stripline. Y is the total Josephson admittance of a stripline section with the periodic l_k, R_s, L_s, and C_s are the resistance, the inductance and the capacitance of a stripline section within the periodic length l_k.

[46] R. L. Kautz, G. Costabile, *IEEE Trans. Magn.* MAG-17 (1981) 780

PTB had arranged up to 166 junctions parallel to the electric field vector of a standing wave inside a 70 GHz waveguide.[47] For this array, an output Josephson voltage of 120 mV with satisfactory stability was reached. However, in this case, the space with a sufficiently homogeneous field in the standing wave pattern of the waveguide was not large enough for many more junctions. As expected from calculations for the single junction design, these results showed that a high frequency of 70 GHz is more advantageous than 20 GHz, and that a microwave distribution circuit had to be developed that would guarantee the homogeneous feeding of a large number of junctions that excluded to a certain degree standing-wave patterns. This was the reason we arranged a 70 GHz series array as part of a periodic superconducting microstripline with a matched terminating load at the end so that no standing-wave patterns could occur in the structure. The stripline impedance of a few ohms was matched to the much higher impedance of the 70 GHz waveguide by an antipodal finline taper that was inserted in a slit at the end of the waveguide. The first array contained only 102 junctions, but it could easily be extended to a higher number of junctions (Figure 9.8).

The 1.5 nm oxide barrier of the junction is extremely thin. This makes the junction fabrication a real challenge and also the junction capacitance very large so that the total rf-current in the array is mainly capacitive: the current through the capacitance is 20 times larger than that through the sub-gap resistance and 10 times larger than the inductive component of the total current. Because of the capacitive nature of the total junction admittance, the periodic stripline may be considered as a high-pass filter with a cut-off frequency of about 25 GHz. The stripline impedance of about 2.2 Ω is nearly like the impedance of the ideal stripline (Figure 9.9). The attenuation of the line is determined by the quasiparticle tunneling losses and by the resistive rf losses: The total attenuation of one stripline period is about 6×10^{-4} dB/period. If the rf-current amplitude should not be reduced by more than 5 % per stripline path, a single line should not contain more than about 700 junctions. For more details of the stripline circuit design see the review by Hinken.[48]

FIGURE 9.10: From left: Clark Hamilton, Richard Kautz, and Jürgen Niemeyer.

At that time, PTB did not have the lithographic tools to realize such a circuit. Therefore I decided to ask Richard Harris of NBS to help us with preparing the circuits. Fortunately, he invited me to stay at NBS in Boulder for six months, and with the support of the Cryoelectronics Section, the small Pb-alloy circuit (Figures 9.8 and 9.9) was realized at the end of 1983. Richard Harris wrote the following memo on November 17, 1983: "Yesterday Dr. Jürgen Niemeyer, guest worker from PTB in Western Germany, demonstrated constant voltage steps at 0.1 V using a series array of Josephson junctions. Niemeyer is working collaboratively at NBS Boulder with Dr. Richard Kautz. This result exceeds published results by a factor of about 4. It is even more remarkable in that it was achieved with an array of only 102 junctions. Each junction produced about 1 mV, or about the maximum voltage per junction that is thought theoretically possible." This meant that we were on the right path. At that time I deposited the circuits on old-fashioned glass substrates which we had to cut to the size and shape of two-inch silicon wafers. The main difficulty with the Pb-alloy circuits was to hit the correct critical current. The problem was solved by choos-

[47] J. H. Hinken, J. Niemeyer, *Kleinheubacher Berichte* 28 (1985) 81

[48] J. H. Hinken, *Supraleiter-Elektronik*, Springer-Verlag Berlin Heidelberg (1988)

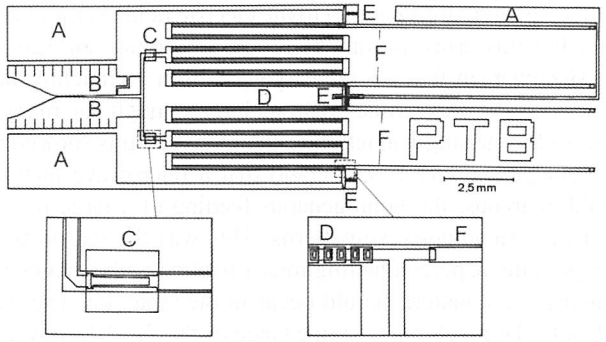

FIGURE 9.11: Series-parallel array with four microwave paths. A: dc pads, B: finline antenna, C: quarter wavelength transformers, D: array, E: bandstop filters, F: matched load.

ing the oxidation parameters in such a way that the critical currents became rather small. Suitable post-fabrication annealing enabled us to increase the small critical currents to the right level. After getting rid of the fabrication problems more or less, we finally had to increase the output voltage. By folding the array several times and simply increasing the number of junctions, step-by-step, to finally 1474 junctions, 1 V steps were generated for the first time.[49] Although the stability of 1 V output was still improvable, we enjoyed the result (Figure 9.10).

9.5.4 1 Volt Circuits

Due to inhomogeneous microwave coupling over the very long folded array stripline with a total attenuation of about 1 dB, spontaneous switching of the 1 V step occurred within a few minutes. Therefore, a new design was developed at PTB in the following year, where a long stripline with 1440 junctions was divided into four folded parallel paths, each of which coupled to the finline antenna via dc blocks and a distribution network. Each path was terminated by a lossy line (Figure 9.11). With respect to the dc bias, the paths remained series-connected. This circuit was fabricated in Pb-alloy technology at PTB and produced stable 1 V reference voltages with a standard deviation of only 3×10^{-10} V. The Cryoelectronics Section at NBS made this circuit type with $Nb/Nb_2O_5/PbInAu$ junctions at about the same time.[50] Later on, this 1 V design was adapted to be used at lower frequencies — 10 GHz at NBS and 35 GHz or 10 GHz at the Institute für Photonische Technologien (IPHT) in Jena — but finally all these versions were given up because of the better performance of the higher-frequency versions.

The main problem that remained was the susceptibility of the lead alloy circuits to damage by humidity and thermal cycling. This was the reason why IBM stopped the development of computer circuits just at the moment when we succeeded with the voltage standard circuit — although there was already a new, more robust junction technology available: M. Gurvitch and coworkers at Bell Laboratories had developed stable Nb junctions with an Al-oxide barrier.[51] On this technological basis, the Josephson computer group at ETL, headed by Hisao Hayakawa, was developing a digital circuit technology which I also found suitable for a more robust voltage standard. Besides the stability of $Nb/Al_2O_3/Nb$ junctions to destructive agents, with a current width of the seventh step

[49] J. Niemeyer, J. H. Hinken, R. L. Kautz, *Appl. Phys. Lett.* 45 (1984) 478

[50] J. Niemeyer, L. Grimm, W. Meier, J. H. Hinken, E. Vollmer, *Appl. Phys. Lett.* 47 (1985) 1222; C. A. Hamilton, R. L. Kautz, R. L Steiner, F. L. Lloyd, *IEEE Elect. Dev. Lett.* EDL-6 (1985) 623

[51] M. Gurvitch, M. A. Washington, H. A. Huggins, J. M. Rowell, *IEEE Trans. Magn.* 19 (1983) 79

of about 420 μA, this technology was the absolute optimum, compared to all other junction types. For the microstrip design, practically no modifications were required because at 70 GHz the surface resistance of Nb films is very similar to that of Pb films. The main difference lay in the large maximum critical current of the Nb/Al junctions, which made the size of the voltage steps nearly twice as large as for the lead alloy junctions. This is not relevant for the circuit design but facilitates the standard operation very much.

Therefore we slightly modified the Pb-alloy design, adapting it to the specific data of the Nb/Al-technology. The design looked very similar to that shown in Figure 9.11. I found support for preparing the lithographic masks at NBS and was invited by Hisao Hayakawa to realize the circuits at ETL at the beginning of 1986. Supported by ETL's Josephson computer group and by the voltage metrology group with T. Endo, M. Koyanagi, and Y. Sakamoto, we succeeded in preparing the first 1 V Nb/Al voltage standard within three months.[52] For this effort we had to modify the ETL fabrication technology because the array junction critical current density was about two orders of magnitude smaller than that for the digital circuits. In addition, the array chip size was considerably larger than that of the digital circuit chips.The NbN/MgO/NbN version was not so successful. Due to the large London penetration depth of NbN, the value of the seventh voltage step, 165 μA, is much smaller than the one for the Nb/Al junctions. Together with the larger spread of the critical currents — caused by non-uniform sputtering of the MgO barrier — this makes the reference voltages unstable. This problem is irrelevant for the naturally grown aluminum oxide barriers of the $Nb/Al_2O_3/Nb$ junctions. ETL's Akira Shoji had developed the sophisticated NbN/MgO fabrication system. The thickness of the extremely thin MgO barrier was precisely determined by counting the cycles of a rotating shutter with a small opening that uncovered the substrate only for a short time per cycle. The result became somewhat better by backing the NbN-layer with Nb, so that the junction sandwich gets the layer sequence NbN/Nb/MgO /Nb/NbN. But in this case, the advantage of the higher operating temperature of NbN — the main reason for implementing the complex technology — becomes questionable. Figure 9.12 shows members of ETL's Josephson computer group and metrology group at my farewell meeting.

FIGURE 9.12: ETL farewell meeting after having fabricated the first 1 V full Nb dc array standards. Clockwise from left: from the computer group Masao Koyanagi and from the metrology group Itaro Kurosawa, Masaskazu Nakanishi, Shin Kosaka, Jürgen Niemeyer, and between the young students, Akira Shoji.

9.5.5 10 Volt Circuits

After having developed the 1 V arrays, we often received requests for 10 V arrays because the direct output voltage of electronic Zener voltage references is 10 V, so that the calibration of these devices would become very simple. With the technologies in the middle of the 1980s this was, however, a real challenge — if one keeps in mind that the sum of the junction areas of a 15,000-

[52] J. Niemeyer, Y. Sakamoto, E. Vollmer, J. H. Hinken, A. Shoji, H. Nakagawa, S. Takada, S. Kosaka, Jpn. *J. Appl. Phys.* 25 (1986) L343

junction array of the described type amounts to about 15 mm^2. This required a 15 mm^2 oxide barrier with a thickness of only 1.5 nm, totally free of defects.

It was clear that with the lead-alloy technology, this was impossible to achieve. Therefore we tried to prepare 10 V Nb/Al circuits at ETL in 1988, but we failed. Although the dc characteristic of the array was good, we found that the available rf-power was not large enough to drive the circuit to 10 V. We therefore tried to replace the SiO of the dielectric layer by high quality SiO_2 that was deposited by means of a low temperature silane PECVD process. However, after having torched a forepump we had to stop the dangerous experiments. At that time, Susumu Takada was guiding the Josephson computer group (Figure 9.13). Unfortunately he passed away in 2008.

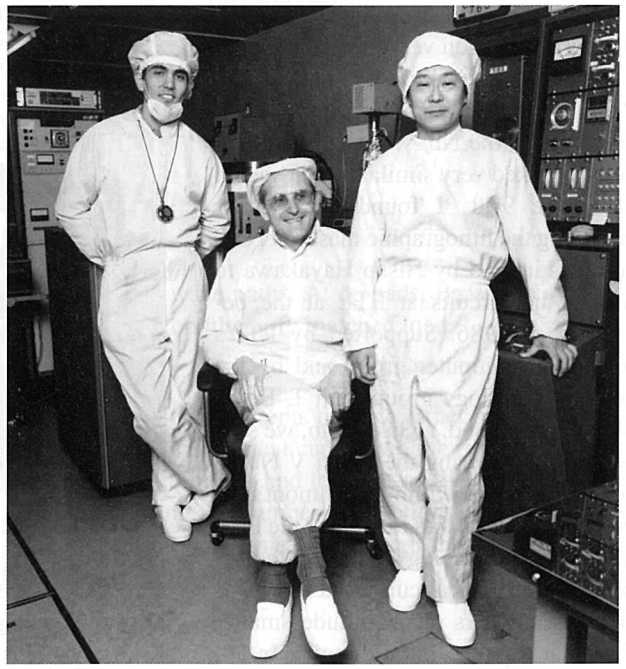

FIGURE 9.13: From left: Yasuhiko Sakamoto, Jürgen Niemeyer and Susumu Takada in the clean room facilities of the Josephson computer group at ETL. I had to sit because of an injury I had received during Kendo lessons.

At NBS in 1983, some circuits $Nb/Nb_2O_5/PbInAu$ were already being prepared from sandwiches which had a much better performance against deterioration from cycling and humidity than the pure Pb-alloy circuits. In 1987, after a long-lasting effort, the NBS group succeeded in preparing a 14,184 junction series array with 16 parallel microwave paths, the first Josephson voltage standard with reference voltages up to 12 V[53] as shown in Figure 9.14. After having implemented a Nb/Al fabrication line, my group at PTB needed another two years until 10 V $Nb/Al_2O_3/Nb$ arrays with up to 20,160 junctions and output voltages of up to 14.5 V could be realized.[54] Because a few problems were left with the sensitivity of the Pb-alloy top electrode layer to humidity, NIST also established Nb/Al technology and produced 10 V all-refractory metal circuits with 20,208 junctions at that time.[55]

Today, the $Nb/Al_2O_3/Nb$ technology is commonly used by the commercial producers of dc array standards as is described in the next section by Clark Hamilton. For an overview on the development of the dc voltage standard array see especially two references.[56,57]

The final success was possible only because all collaborators were willing to share their knowledge, accept different ways of thinking and living, and avoid complex bureaucratic procedures. While working in this way, the dc array standard was introduced as the primary voltage standard worldwide within a few years. In my opinion, the development of the dc array voltage standard is a convincing example of a fruitful international collaboration.

[53] F. L. Lloyd, C. A. Hamilton, J. A. Beall, D. Go, R. H. Ono, R. E. Harris, *IEEE Electron. Device Lett.* EDL-8 (1987) 449

[54] R. Pöpel, J. Niemeyer, R. Fromknecht, W. Meier, L. Grimm, *J. Appl. Phys.* 68 (1990) 4294

[55] C. A. Hamilton, C. J. Burroughs, *IEEE Trans. Instrum. Meas.* 44 (1995) 23

[56] R. L. Kautz, *Rep. Prog. Phys.* 59, 935–992, 1996

[57] J. Niemeyer, in *Handbook of Applied Superconductivity*, Vol. 2, ed. by B.Seeber, IOP Publishing, Bristol and Philadelphia (1998) 1813

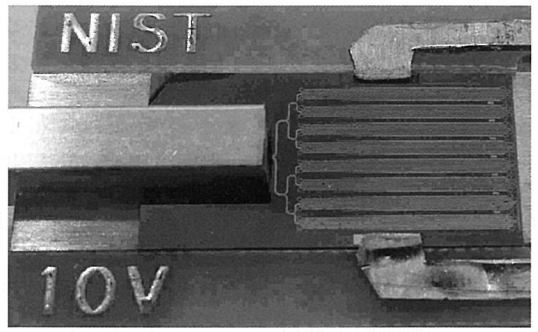

FIGURE 9.14: First 10 V chip in $Nb/Nb_xO_y/Pb$ alloy junction technology. The finline taper is inserted into the end of a 70 GHz waveguide. Dc contact is made by the two lead foils in the right part of the figure. The single junction area is 15 μm × 30 μm. (Courtesy of Clark Hamilton, NIST).

9.6 Making the Josephson Voltage Standard Practical

Clark A. Hamilton

A key element in the development of the first Josephson standard above one volt was the realization by Levinson[58] in 1977 that the zero crossing constant voltage steps of highly capacitive Josephson junctions provided the means to bias thousands of junctions into a quantized voltage state with a single bias current — namely zero bias current. My first observation of zero-crossing steps occurred as a graduate student of Sidney Shapiro. Shapiro was the first to confirm Josephson's prediction of rf-induced constant voltage steps in the I-V curve of a superconductive tunnel junction.[59] He suggested a thesis project to measure the detailed behavior of these steps as a function of applied microwave frequency and power. Theory predicted an oscillatory Bessel function behavior with increasing power and with a sharp deviation from Bessel behavior when the rf voltage across the junction exceeded the superconductive energy gap voltage (the Riedel peak). So, in 1969, I was making Sn-SnO-Sn

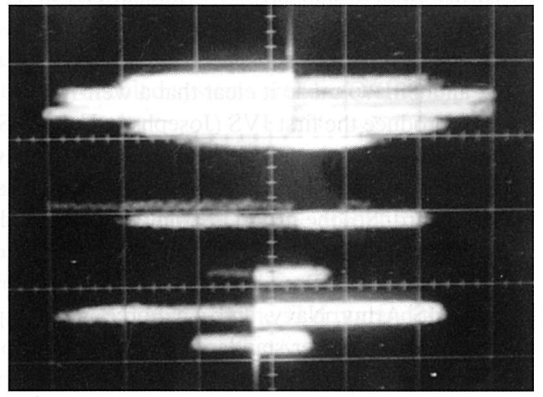

FIGURE 9.15: An early observation of zero-crossing constant voltage steps in a single tin-tin oxide-tin Josephson junction with a 10 GHz microwave bias. The steps occur at precise voltage multiples of $hf/2e \approx 21\ \mu V$, where f is the microwave frequency, h is Planck's constant and e is the electron charge. The scales are 100 μV/div. vertical, 5 μA/div. horizontal. 18 December, 1969.

[58] M. T. Levinson, R. Y. Chiao, M. J. Feldman and B. A. Tucker, *Appl. Phys. Lett.*, 32 (1977) 776

[59] S. Shapiro, *Phys. Rev. Lett.* vol. 11 (1963) 80

junctions and observing their microwave-induced constant voltage steps. Somewhat accidentally the early results showed zero-crossing steps as in Figure 9.15.

The behavior of these steps did not match the theory because the junctions were too big and the microwave power and frequency were too small. After a year of work, I successfully suppressed those pesky zero-crossing steps and wrote my thesis confirming an obscure detail of superconductivity theory while completely ignoring the zero-crossing steps that would become, 30 years later, the basis for the most important and widespread practical use of superconductive microcircuits. So much for lost opportunities.

Sixteen years later in the early 1980s, I found myself in a group in the Cryogenics Division at NBS[60] in Boulder, Colorado. The group mission was to develop superconductor integrated circuit technology for the purpose of advancing electrical metrology. Catalyzing this research was a large program at IBM to develop superconductive logic for the next generation of ultra-fast computers. The IBM program pioneered the development of a superconductive integrated circuit process and this process was reproduced at NBS. This new technology opened the possibility to exploit Levinson's suggestion to put thousands of junctions on one chip and thus realize a Josephson standard at 1 V or more. The first attempts to do this were largely a failure owing to nonuniform distribution of microwave power and a lack of understanding of the chaotic nature of the microwave-driven Josephson junction and the consequences for stability. Eventually the microwave distribution problem was solved by Jürgen Niemeyer and Johann Hinken at PTB, and the stability problem was solved by Richard Kautz at NIST. A joint NIST/PTB effort brought these solutions together and culminated in the fabrication of the first successful 1474-junction array at NBS, in 1984.[61]

My entry into the development of the series array Josephson array voltage standard began shortly after Niemeyer and Kautz demonstrated the first 1 V chip. During the next year both PTB and NBS developed improved chips and the hardware and software required to implement the Josephson series array voltage standard.[62,63] Soon after 1985, NBS and PTB made array chips available to other national standards laboratories, and those labs developed their own measurement systems based on these chips. Early Josephson array voltage standards developed in the mid 1980s at NBS, PTB, NPL, and CSIRO made it clear that a well-funded standards lab with a highly trained research staff could reproduce the first JVS (Josephson Voltage Standard) systems built at NBS and PTB. In 1987, the NBS Boulder lab and the PTB lab in Braunschweig were the only two places in the world where these chips could be fabricated, and there was considerable interest from other labs in obtaining the new standard. So, the group in Boulder proceeded to develop a Josephson voltage standard system that could readily be reproduced and used by metrology technicians in many standards laboratories. By 1992, the NIST Boulder group had sold complete JVS systems to Lockheed, Hewlett Packard, and the US Army, Navy, and Air Force, and supplied chips and provided advice on constructing systems to many other standards laboratories throughout the world. Commercial sources were developed for every component of the system. The chip design and fabrication details were transferred to Hypres, Inc., a small company in New York that focused on practical applications of Josephson technology. Hypres became and continues today as a key supplier of JVS chips as well as complete turn-key systems. In the same way, PTB carried over its technology to the Institut für Photonische Technologien (IPHT) in Jena, Germany, and the IPHT founded a small company Supracon which delivers circuits and systems, too.

The design problem does not end with the completion of a practical and convenient voltage standard. A system like the JVS with a very small demand (at most a few systems/year) necessarily depends on components that are widely used for other purposes. As technology advances some of

[60] NBS became the National Institute of Standards and Technology, NIST, in 1989.

[61] J. Niemeyer, J. H. Hinken, R. L. Kautz, *Appl. Phys. Lett* 45 (1984) 478

[62] C. A. Hamilton, R. L. Kautz, R. L. Steiner, F. L. Lloyd, *IEEE Elec. Dev. Lett.* EDL-6 (1985) 623

[63] J Niemeyer, L. Grimm, W. Meier, J. H. Hinken, E. Vollmer, *Appl. Phys. Lett.* 47 (1985) 1222

these components become obsolete and unavailable. When this happens, the JVS design must be modified to use currently available hardware and software. This is an ongoing development process that is unlikely to end anytime soon. The remainder of this article focuses on the details of the JVS system and how the solutions to a variety of practical problems have evolved to make its dissemination possible. Since the author is most familiar with the NIST development, that is the story that will be told here.

Before delving into the details of the system design, one must ask what this system will be used to accomplish. The great majority of standards labs wanted a JVS system to calibrate secondary Zener-based dc reference standards[64]. Since the best Zener standards are stable at a few parts in 10^8, a JVS system with an uncertainty of a few parts in 10^9 would be perfectly adequate. A few customers wanted Josephson systems to calibrate and measure the linearity of high end digital voltmeters (DVMs), requiring about the same level of uncertainty. And then there are the metrology purists who are interested in verifying the underlying physics and uncovering system design flaws by comparing one JVS system to another with the smallest possible uncertainty. The NIST design emphasizes automation and convenience aimed at the first two classes of customers without precluding direct system-to-system comparisons at state-of-the-art accuracy.

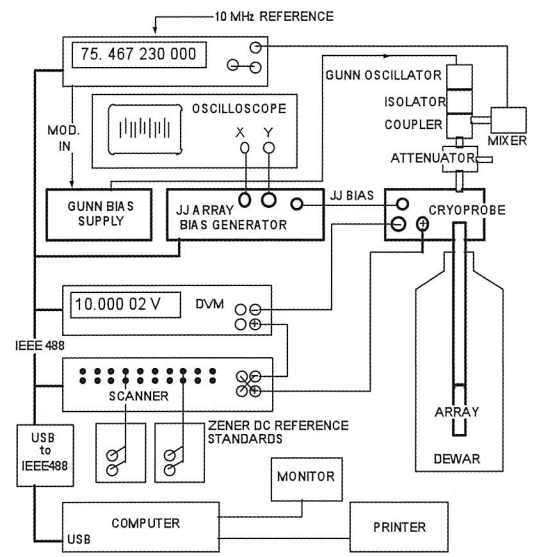

FIGURE 9.16: A typical JVS system. The figure shows a "dipper" system where the chip is cooled in a liquid helium Dewar. Liquid-helium-free cryocooled systems are also available.

The basic architecture of the system, shown in Figure 9.16, is fairly obvious, and essentially similar systems were developed at NIST and PTB. The system includes a means for cooling the chip to approximately 4.2 K in a magnetically and electrically shielded environment, supplying dc bias current for the Josephson junction (JJ) array and an accurately known microwave frequency (typically near 75 GHz), and transmitting the generated voltage to room temperature with a minimum of corruption from noise and thermal emf effects. Calibration of Zener standards is accomplished by placing the JJ array and the Zener in series opposition and measuring the difference voltage with a sensitive voltmeter. A reversing switch allows the computation of and correction for thermal voltages in the measurement loop. This reversing switch is usually a scanner that can select and reverse any one of 16 or more devices. An oscilloscope is usually required to find optimal operating conditions. Bias current for the JJ array is supplied from a variable impedance source that allows the display of I-V curves and computer control of the operating point.

The items shown in bold are specially designed for the JVS system. Over the years several small companies have made these devices, usually from designs developed at NIST or PTB. The remaining items are standard laboratory instruments that can be purchased commercially.

The computer hardware and software have seen the greatest need for updates to keep pace with advancing technology. The original system of 1989 operated under the DOS operating system using a QBasic program and communicated through the parallel port, an IEEE interface card and a special purpose digital/analog ISA card. Some of these first-generation systems are still in operation. In

[64] A semiconductor reversed-biased Zener diode is commonly used as the basis of commercial voltage references.

the meantime, the system has evolved to operate under Windows with much more capable control software written in Visual Basic and all communication to the DVM, microwave system, scanner and system controller through a single USB connector.

A software package (NISTVolt^{TM}) originally started at NIST has evolved over more than 20 years with contributions from many individuals. Its most used function is the automated calibration of a specified set of Zener dc reference standards. The basic algorithm of measuring the voltage difference between the Zener standard and the JJ array sounds simple enough, but when all contingencies are accounted for, this one function has about 2500 lines of code.

Software validation: How can a user be certain (and prove to an auditor) that the computer code is free from errors that could corrupt calibration results? NISTVolt addresses this with a simulation mode in which the JJ array, DVM, microwave system, and cable connections are all replaced by simulated devices that can be configured to include real-life defects, for example, an unstable JJ array voltage, measurement noise, thermal emfs, spurious DVM readings, DVM gain error, etc. By running the software in this simulation mode it is possible to quantify the effect of all these defects on the final calibration result and its computed uncertainty budget. When the simulation results are combined with regular check standard measurements, systematic uncertainty evaluations, and interlaboratory comparisons, a JVS system achieves a very high level of confidence.

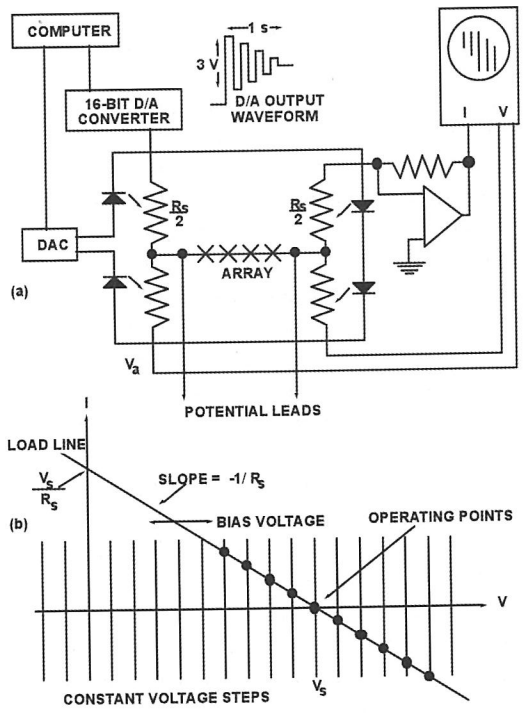

FIGURE 9.17: (a) Array bias system; (b) I-V curve and load line.

The array bias system shown in Figure 9.17(a) facilitates the process of setting the Josephson array on a constant-voltage step close to a specific voltage. It consists of a computer-controlled DAC and a circuit for controlling the bias impedance. Figure 9.17(b) shows the superimposed I-V characteristics of the Josephson array and the bias system. The vertical lines are the constant-voltage steps. The diagonal line is the bias-source load line. Its position and slope are computer controlled. The intersections of the load line and steps represent all of the possible operating points. If the load line is steep enough, then just one step will be selected. Unfortunately this solution is unstable and usually results in an oscillation among two or more steps. A better approach is to select a load line slope that intersects 10 to 40 steps and then bring the load line V-axis intercept to the desired voltage with a "ringing" waveform, as shown in the inset.

FIGURE 9.18: A commercially available cryoprobe for a Josephson voltage system. Compliments of High Precision Devices Inc.

This usually results in the selection of a very stable step that is at, or very close to, the desired voltage. Once a suitable step is found, the four opto-isolators (shown as LED-controlled resistors)

are turned off to establish the zero-current bias set point and to isolate the JJ array from any noise or disturbance in the bias system.

The microwave subsystem shown in Figure 9.16 is based on a Gunn oscillator and microwave source locking counter. This arrangement has been the most commonly used microwave source. As of this writing (2010) the availability and reliability of Gunn oscillators is on the wane and new sources based on a low-frequency (~ 10 GHz) synthesizer followed by a frequency multiplier/amplifier chain will likely become the dominant source in the future.

A typical cryoprobe is shown in Figure 9.18. Its function is to provide a means to cool the JJ array chip to approximately 4 K, deliver dc and microwave bias current, and to bring the precision voltage out to room temperature. The 75 GHz waveguide from room temperature to the JJ chip is a good example of how a critical component evolved over the years to improve performance and adjust to commercial availability. The initial solution was a standard bronze waveguide. About 1990, the Gore Company developed a flexible dielectric waveguide with lower attenuation and much lower thermal conductivity. With sales of only a few per year, Gore soon lost interest and priced the part beyond reach. At this point, NIST developed a rigid dielectric waveguide consisting of a 25 mm Teflon tube with a 2.5 × 5 mm rectangular core. About the same time PTB developed a tube waveguide that proved to be more durable. The original tube waveguide was made of German silver and later improved by using an internally silver-plated stainless steel tube. This evolution of system design is typical of many parts of the system and highlights the need for continuing technical support for users of JVS systems.

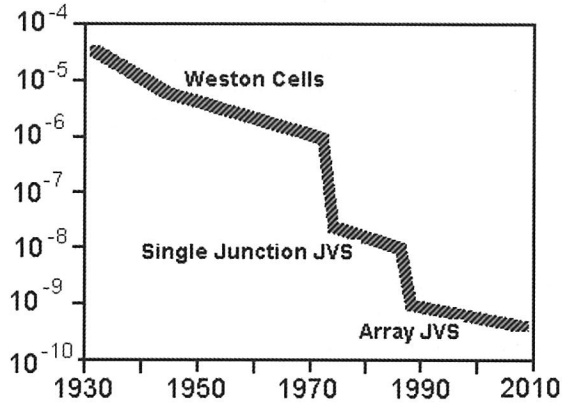

FIGURE 9.19: The approximate level of agreement in dc voltage measurements among standards laboratories through the years 1930 to 2010. The figure illustrates the major improvements that occurred as the technology evolved from Weston cells to single Josephson junction standards and finally to large arrays of Josephson junctions.

Figure 9.19 shows how the development of Josephson standards has improved the agreement among voltage standards laboratories around the world. Figure 9.20 illustrates the dissemination of these standards around the world. Although the Josephson series-array voltage standard based on zero-crossing steps has greatly advanced the state of the art in voltage metrology, it is not without its defects. First among these are the difficulty of rapidly setting a specified voltage and the tendency of noise to cause random jumps between the quantized voltage levels. As discussed in the following articles in this chapter by Johannes Kohlmann and Samuel Benz, new advances in chip design and fabrication, and very fast bias electronics now provide solutions to both of these problems.

FIGURE 9.20: The black dots show the distribution of Josephson standards around the world in 2010.

9.7 Programmable Josephson Voltage Standards: from DC to AC

Johannes Kohlmann

9.7.1 Introduction

As described in previous sections, conventional Josephson voltage standards have been operated very successfully for dc applications since the mid 1980s. Some experts therefore already assumed in the early 1990s that the development of Josephson voltage standards would be completed. This estimation was then completely revised by new ideas. What is behind all this? Conventional Josephson array voltage standards do not enable switching rapidly and reliably between different specific voltage levels, due to their overlapping, metastable constant-voltage steps. The increasing interest in rapidly switching arrays and in highly precise ac voltages has stimulated several research activities to develop measurement tools based on Josephson arrays to meet these requirements. One approach is the programmable Josephson voltage standard (PJVS) first suggested by Hamilton et al. at NIST in 1995.[65] In principle, it is a Josephson multi-bit digital-to-analog converter based on a series array of overdamped Josephson junctions divided into a binary sequence of independently biased smaller arrays. While 2,048 junctions delivered nearly 300 mV in the first realization, modern versions contain more than 100,000 junctions for output voltages up to 10 V. Some of these fascinating developments are summarized in this contribution.

9.7.2 Principles and Fundamentals of PJVS

PJVS are intended to extend the use of high-precision Josephson voltage standards from dc to ac. This promising expectation of the suggestion by Hamilton et al. in 1995 did directly bring us to launch our own research work at PTB. PJVS are based on series arrays of overdamped Josephson junctions showing a non-hysteretic current-voltage characteristic. The current-voltage characteristic remains single-valued under microwave operation (Figure 9.21(b)). A PJVS is operated as a multi-bit digital-to-analog converter. The series array of M total junctions is divided into smaller independently biased programmable segments; see Figure 9.21(a). The number of junctions per segment often follows a binary sequence, the so-called binary-divided arrays. The output voltage $V = n \cdot M \cdot \Phi_0 \cdot f$ is given by digitally programming the junction step number n for the junctions in each segment (typically is n = -1, 0, +1); $\Phi_0 = h/2e \approx 2.07\ \mu V/GHz$ denotes the flux quantum, h Planck's constant, e the elementary charge, and f the frequency of an external microwave. Each constant-voltage step between $-M$ and $+M$ can be selected by suitable programming of the different segments. A fast bias electronics enables switching times of a few tens of nanoseconds.[66] The number of junctions necessary to attain a given voltage is increased by a factor of five compared with conventional SIS[67] arrays, as PJVS are typically operated on the first-order constant-voltage step instead of the fifth one for SIS arrays.

9.7.3 Overdamped Josephson Junctions for PJVS

Overdamped Josephson junctions are needed for PJVS. Hamilton et al. demonstrated a PJVS for the first time using externally shunted SIS junctions.[65] In an array consisting of 8,192, 2048

[65] C. A. Hamilton, C. J. Burroughs, and R. L. Kautz, *IEEE Trans. Instrum. Meas.* 44 (1995) 223

[66] J. Lee, R. Behr, A. S. Katkov, and L. Palafox, *IEEE Trans. Instrum. Meas.* 58 (2009) 803

[67] Layered films are described by S: Superconductor, I: Insulator, N: Normal metal, I': doped semiconductor

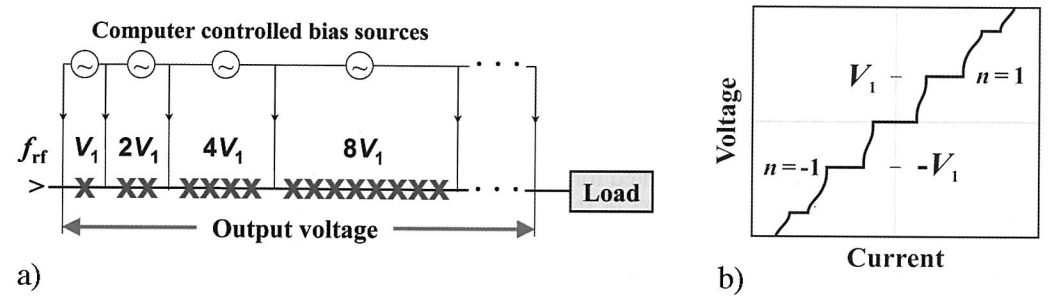

FIGURE 9.21: (a) Schematic design of a programmable Josephson voltage standard based on a binary-divided series array of Josephson junctions shown as '×'; (b) Current-voltage characteristic of an overdamped Josephson junction under microwave irradiation. The microwave power is set to equalize the widths of the zeroth and first constant-voltage steps.

junctions were operated at 75 GHz and delivered an output voltage of about 300 mV. As a design for externally shunted SIS junctions is rather complex and challenging, and the critical current and consequently the step width of these arrays are limited to a few hundred microamperes because of design restrictions, other junction types have subsequently been investigated. Calculations by Kautz gave important hints for the realization of optimized metallic-barrier Josephson junctions.[68]

Most currently fabricated series arrays are based on one of three different junction types: SNS junctions, SINIS junctions, and SI'S junctions, the barrier of which consists of a semiconductor such as Si doped with a metal and being near a metal-insulator transition. The low characteristic voltage $V_c = I_c \cdot R_n$ of SNS junctions leads to operating frequencies around 15 GHz (I_c denotes the critical current and R_n the normal state resistance). The characteristic voltage of SINIS and SI'S junctions can be tuned on the other hand over a wide range, enabling operation at frequencies either around 15 GHz or around 70 GHz. The latter is of special interest, from our point of view at PTB, as conventional Josephson voltage standards are also operated around 70 GHz and therefore the same microwave set-up can be used, and as the fabrication technology is less challenging due to the lower number of junctions necessary to reach a certain voltage level.

The first practical 1 V PJVS were realized at NIST by Benz et al. in 1997.[69] A total of 32,768 SNS junctions were embedded into the middle of a coplanar waveguide transmission line (CPW) and contained PdAu as the normal metal. The arrays were operated around 16 GHz and showed wide constant-voltage steps. The low resistivity of PdAu requires junctions of very high critical current densities around 200 kA/cm^2 in order to reach characteristic voltages of about 25 μV. This makes the technology very challenging, especially at the via contacts between the Nb top electrode and the Nb wiring. Different materials have been investigated at NIST in order to increase the resistivity of the normal metal and thus to make the technology more simple. An additional drawback arises from the low microwave frequency: To reach the 10 V level, more than 300,000 junctions are needed. An idea to handle this huge number is the use of stacked junctions. Silicide-based junctions were hence investigated at NIST. Voltages up to 3.9 V were generated by arrays of double- and triple-stacked junctions containing $MoSi_2$ barriers.[70] The huge number of junctions causes enormous challenges for microwave design and for the fabrication.

[68] R. L. Kautz, J. *Appl. Phys.* 78 (1995) 5811

[69] S. P. Benz, C. A. Hamilton, C. J. Burroughs, T. E. Harvey, and L. A. Christian, *Appl. Phys. Lett.* 71 (1997) 1866

[70] Y. Chong, C.J. Burroughs, P.D. Dresselhaus, N. Hadacek, H. Yamamori, and S.P. Benz, *IEEE Trans. Appl. Supercond.* 15 (2005) 461

Therefore, shortly after the first successful experiments at 16 GHz, we discussed in our group at PTB, whether practical PJVS could also be operated at frequencies around 70 GHz, which would result in a significant reduction of the number of junctions. In order to realize corresponding high values of 150 μV for the characteristic voltage, we needed materials showing a high electrical resistivity. We were still investigating etching processes for different metals, when the use of a very promising kind of junctions was presented for electronic applications at the International Superconductive Electronics Conference in 1997 in Berlin.[71] We subsequently investigated these junctions consisting of a SINIS multilayer in our group at PTB and fabricated our first small series arrays within a few months.[72] 1 V arrays were realized shortly after,[73] but nobody believed in 10 V arrays. Nevertheless, we gave 10 V a try and directly succeeded in 10 V arrays for the first time in spring 2000.[74] This success was partly caused by the use of 70 GHz junctions and by an active contribution of the junctions embedded into low-impedance microstriplines. We fabricated the SINIS arrays in a technology similar to that which is used for fabrication of conventional SIS junctions. The arrays consisted of 8,192 junctions (1 V) and 69,120 junctions (10 V), respectively.

In spite of their successful use, a serious drawback of SINIS junctions became visible in the course of time. Measurements of many arrays showed that a few junctions of SINIS series arrays are often missing, i.e., they exhibit a superconducting short (typically between 0 and 10 of 10,000 junctions). SINIS junctions seem to be very sensitive to some particular steps during fabrication, probably due to their very thin insulating oxide layers. This problem drives the search for more robust barrier materials. A very promising material was investigated at NIST consisting of an amorphous silicon layer doped with a metal such as niobium.[75] The niobium content is tuned to a value near the metal-insulator transition. This region combines a high resistivity and a sufficient conductivity needed for Josephson junctions. Nb_xSi_{1-x} barriers were initially used at NIST for pulse-driven arrays. We investigated at PTB in 2008 the use of junctions based on Nb_xSi_{1-x} barriers for operation at 70 GHz in close cooperation with NIST. The characteristic voltage was tuned to about 150 μV by adjusting the Nb content and the thickness of the barrier at NIST. 1 V and even 10 V arrays were then fabricated in our group at PTB.[76] Our first measurements confirmed that these new junctions are really more robust than SINIS junctions; fabrication is possible with a better yield, as the number of shorted junctions is significantly reduced. For the first time, programmable 10 V arrays consisting of 69,632 junctions were realized without any shorted junctions. These outstanding results were made possible by the close cooperation between our groups at NIST and PTB. This junction type presently enables the most reliable fabrication process.

Some other junction types were additionally studied recently. The advantage of array operation at higher temperatures than 4 K has been investigated at the National Institute of Industrial Science and Technology (AIST) in Japan, partly in collaboration with NIST.[77] Arrays were operated in a cryocooler at temperatures around 10 K by using NbN for the superconducting layers and TiN for the barrier. Yamamori et al. realized corresponding arrays, which consist of more than 500,000 junctions for operation at 16 GHz, generating voltages up to 17 V.[78] First steps were made toward fabrication of series arrays on a commerical basis. Hassel et al. (at the Technical Research Center of Finland (VTT)) exceeded the 1 V level using an improved design of 3315 externally shunted

[71] M. Maezawa and A. Shoji, *Appl. Phys. Lett.* 70 (1997) 3603; H. Sugiyama, A. Yanada, M. Ota, A. Fujimaki, and H. Hayakawa, *Jap. J. Appl. Physics*, 36 (1997) L1157

[72] H. Schulze, R. Behr, F. Müller, and J. Niemeyer, *Appl. Phys. Lett.* 73 (1998) 996

[73] R. Behr, H. Schulze, F. Müller, J. Kohlmann, and J. Niemeyer, *IEEE Trans. Instrum. Meas.* 48 (1999) 270

[74] H. Schulze, R. Behr, J. Kohlmann, F. Müller, and J. Niemeyer, *Supercond. Sci. Technol.* 13 (2000) 1293

[75] B. Baek, P. D. Dresselhaus, and S. P. Benz, *IEEE Trans. Appl. Supercond.* 16 (2006) 1966

[76] F. Müller, R. Behr, T. Weimann, L. Palafox, D. Olaya, P. D. Dresselhaus, and S. P. Benz, *IEEE Trans. Appl. Supercond.* 19 (2009) 981

[77] H. Yamamori, M. Ishizake, A. Shoji, P. D. Dresselhaus, and S. P. Benz, *Appl. Phys. Lett.* 88 (2006) 042503

[78] H. Yamamori, T. Yamada, H. Sasaki, and A. Shoji, *Supercond. Sci. Technol.* 21 (2008) 105007

SIS junctions operated at 70 GHz on the third order constant-voltage step.[79] Lacquaniti et al. (at the Instituto Nazionale di Recerca Metrologia (INRIM) in Italy) developed SNIS junctions based on a thick Al layer (up to 100 nm), which is slightly oxidized. 1 V SNIS arrays were subsequently fabricated within a cooperation between INRIM and PTB.[80]

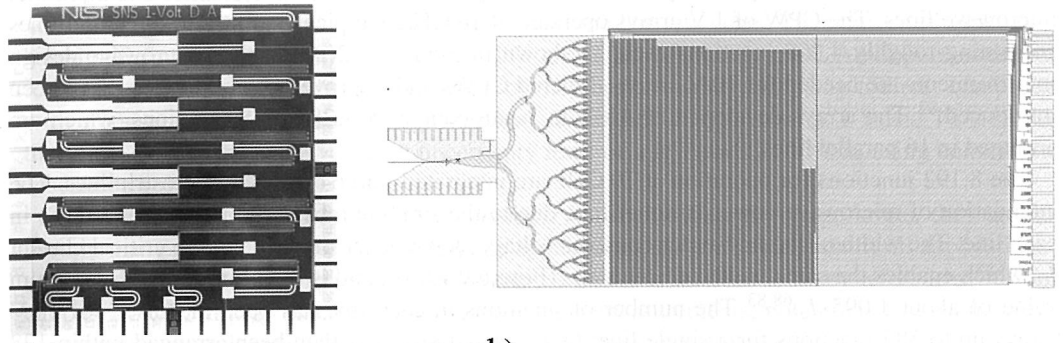

FIGURE 9.22: Examples of PJVS designs: (a) 1 V design for operation at 16 GHz. 32,768 SNS junctions are arranged in the middle of 8 parallel coplanar waveguide transmission lines. The chip size is 10 mm × 10 mm. (Courtesy of S.P. Benz, NIST); (b) 10 V design for operation at 70 GHz. 69,632 SI'S junctions are embedded into 128 parallel low-impedance microstriplines. The chip size is 24 mm × 10 mm.

9.7.4 Realization of Series Arrays

The thin-film fabrication process for PJVS is based on the Nb technology of conventional Josephson voltage standards. Significant improvements at all technological levels in the last two decades enable the fabrication of series arrays containing a huge number of junctions with acceptable yield. This technological progress has been a major prerequisite for the development of PJVS. While the Josephson junctions are embedded into a low-impedance microstripline for arrays operated at 70 GHz similar to conventional SIS arrays, the junctions are integrated into the middle of a coplanar waveguide (CPW) transmission line for 16 GHz arrays. The ratio of the low junction impedance to the typical impedance of these CPWs of about 50 Ω leads to a similar situation as the microstripline for conventional SIS arrays. Attenuation of the microwave power is low because the junctions are loosely linked to the CPW. In contrast, overdamped junctions in a low-impedance microstripline attenuate microwave power at a much higher rate than for SIS arrays. The large attenuation follows from the fact that the resistive impedance of the junctions plays an important role, so that a major part of the microwave power is dissipated resistively. The high attenuation is, however, compensated in part by an active contribution of the junctions; the junctions act as oscillators.[81] Fortunately, we were unconcerned about high attenuation and active contribution when starting the development of SINIS junctions. We designed and fabricated the arrays, and they did work very well. Only later did

[79] J. Hassel, P. Helistö, L. Grönberg, H. Seppä, J. Nissilä, and A. Kemppinen, *IEEE Trans. Instrum. Meas.* 54 (2005) 632

[80] V. Lacquaniti, N. De Leo, M. Fretto, A. Sosso, F. Müller, and J. Kohlmann, *Precision Electromagn. Meas. Conf. Digest* (2010) 145

[81] H. Schulze, F. Müller, R. Behr, J. Kohlmann, J. Niemeyer, and D. Balashov, *IEEE Trans. Appl. Supercond.* 9 (1999) 4241

we realize the microwave behavior of overdamped Josephson junctions.

The main challenge for the design of PJVS is the homogeneous distribution of microwave power among the junctions. While this request is reasonably possible for 1 V arrays typically consisting of 8,192 junctions (70 GHz) and around 33,000 junctions (16 GHz), respectively, the requirements significantly increase for 10 V arrays containing nearly 70,000 junctions (70 GHz) and even more than 300,000 (16 GHz), respectively. The series arrays are therefore arranged in several parallel microwave lines. The CPW of 1 V arrays operated at 16 GHz is typically split into 8 parallel lines containing roughly 4,000 junctions each, as shown in Figure 9.22(a). Further microwave design improvements are needed for 10 V arrays. Tapered CPWs and improved power dividers have been introduced.[82] The arrays developed at AIST in Japan contain 524,288 SNS junctions, which are arranged in 16 parallel lines.[78]

The 8,192 junctions for operation at 70 GHz are integrated into 64 parallel microstriplines. The attenuation of microwave power is rather low, due to the small number of junctions (only 128) in each line. The width of the first-order constant-voltage step reaches the value of the critical current I_c, which enables the same width of both steps (Figure 9.23(a)), and is therefore near its maximum value of about $1.095 \cdot I_c$.[68,83] The number of junctions in each line has been increased for 10 V arrays up to 582 junctions for a single line; 69,632 junctions have then been arranged within 128 parallel lines as shown in Figure 9.22(b)[76] and Figure 9.23(b).

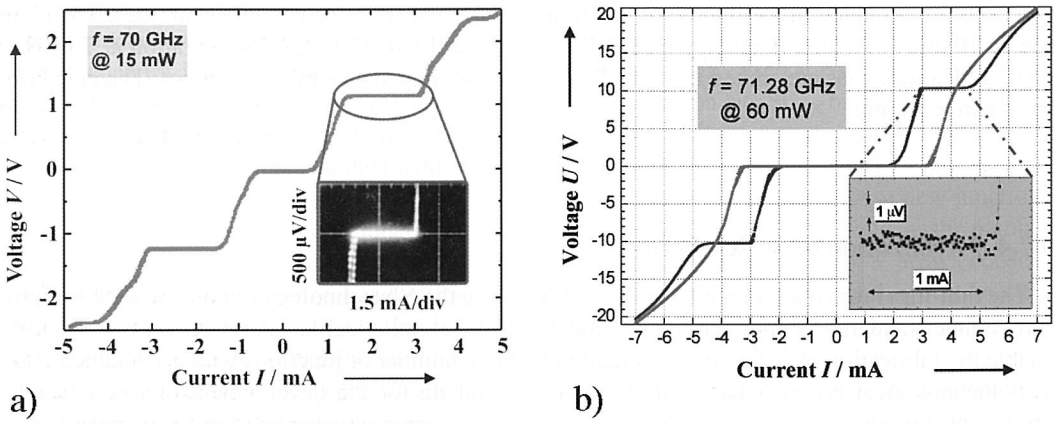

FIGURE 9.23: Current-voltage characteristics (IVC) of PJVS under 70 GHz microwave irradiation showing constant-voltage steps. The insets show the steps at high resolution: (a) 1 V array consisting of 8192 SINIS junctions. Zeroth and first-order steps reach the same width above 1 mA; (b) 10 V array consisting of 69,632 SI'S junctions. The graph also shows the IVC without microwave irradiation.

The dimensions of the junctions should be at the order of the Josephson penetration depth at most, as calculations have shown.[68] As the Josephson penetration depth is determined mainly by the critical current density of the junctions, their lateral size therefore ranges from a few micrometers for SNS junctions with critical current density above 100 kA/cm^2 to about 20 µm x 50 µm for SINIS junctions with a current density below 1 kA/cm^2. As the step width of the constant-voltage step at

[82] M. M. Elsbury, P. D. Dresselhaus, N. F. Bergren, C. J. Burroughs, S. P. Benz, and Z. Popovic, *IEEE Trans. Microwave Theory Tech.* 57 (2009) 2055

[83] O. Kieler, R. Behr, F. Müller, H. Schulze, J. Kohlmann, and J. Niemeyer, *Physica C* 372 (2002) 309

1 V or 10 V should be about at least 1 mA for applications, the junction size is chosen such that the critical current ranges between 1 mA and 10 mA at most.

9.7.5 Applications

Good and reliable 1 V PJVS arrays have been available since the late 1990s; the availability of 10 V arrays has been considerably improved within the last few years. The number of applications has significantly increased in parallel, with 1 V arrays being initially used. An important first test for different junction types is the validation of the constant-voltage steps by a direct comparison with a conventional Josephson voltage standard. Several dc comparisons at 1 V and 10 V showed that PJVS enable the same very low uncertainty level of a few parts in 10^{11} as using conventional Josephson voltage standards.[73,76]

Since PJVS allow rapid and reliable switching between different voltage levels, they are now used in many different high-precision voltage applications. As the description of all applications is not possible within this brief survey, the interested reader is referred to many references.[84] Applications include, among others, calibrations, linearity measurements, potentiometers, watt balance experiments, metrological triangle experiments, and quantum voltmeters.

The synthesis of stepwise-approximated ac waveforms was an early promise connected with the development of PJVS. But initial precision measurements already revealed the difficulties in generating ac waveforms with low uncertainty due to the transients occurring during the switching between constant-voltage steps. Besides these errors, the accuracy of the rms voltage is limited by higher harmonics resulting from the digital nature of the generated waveform. The synthesis of waveforms is therefore restricted to low frequencies, such as power applications at 50 Hz or 60 Hz.[66,85] The use of sampling voltmeters additionally improves measurements at low frequencies by discarding those data points acquired in the transient regions. These investigations are partly discussed in more detail in the next article by Sam Benz.

9.7.6 Conclusions and Outlook

Programmable Josephson voltage standards have been the next step in the exciting story of applications of the Josephson effect in metrology. PJVS have now achieved a high level of maturity after roughly one and a half decades of development. The significant progress of the fabrication technology within this period has been a major prerequisite for the development of series arrays for PJVS. While 1 V arrays are routinely fabricated, first 10 V arrays containing tens or even hundreds of thousands of Josephson junctions are available by now. These arrays belong to the most complex circuits in superconducting electronics. The circuits have been used for several different applications demanding rapid and reliable switching between different specific voltage levels or highly precise ac voltages, respectively. Some of these exciting results have been achieved within the framework of fruitful cooperations and projects. PJVS will significantly improve applications like conventional Josephson voltage standards did for dc applications. I expect that PJVS will therefore be commercially available soon. They will then replace more and more conventional Josephson voltage standards, as PJVS are easier to operate and provide exciting additional possibilities and applications.

[84] For example, B. Jeanneret and S.P. Benz, *Eur. Phys. J. Special Topics* 172 (2009) 181, or in the special issues of the biennial Conference on Precision Electromagnetic Measurements (CPEM) in *IEEE Trans. Instrum. Meas.*

[85] C. J. Burroughs, A. Rüfenacht, S. P. Benz, and P. D. Dresselhaus, *IEEE Trans. Instrum. Meas.* 58 (2009) 761

9.8 Quantum-Based Voltage Waveform Synthesis

Samuel P. Benz

More than a decade of research and development was required to practically exploit the quantum behavior of superconducting Josephson junctions for ac applications. Sine waves and arbitrary waveforms had to be synthesized with sufficiently large voltage amplitudes; and measurement techniques with appropriate accuracy had to be developed. Two waveform synthesis methods, pulse-driven and stepwise-approximation, have now been implemented in a number of practical systems that are presently being used to calibrate audio-frequency ac voltages and power meters, characterize the stability and linearity of analog components, and as an arbitrary waveform source at the heart of an electronic primary thermometer. Some of the important milestones from these efforts, from my perspective, portray the importance of collaboration as well as the challenges that are typical of technology development. Most importantly, these events have shown how important it is to ensure the accuracy of electrical measurements, even when using quantum-based systems.

The first method that successfully synthesized quantum-based voltage waveforms was the programmable Josephson voltage standard (PJVS), which was conceived by Clark Hamilton in 1991. He proposed synthesizing step-wise approximated sine waves, similar to a multi-bit digital-to-analog converter (DAC), by independently current biasing series-connected arrays on different quantized voltage steps (Shapiro steps). During my postdoc at NIST in September of that year, Clark asked me to research prototype circuit designs. I based the circuit designs on aluminum-oxide-barrier tunnel junctions with external shunt resistors. At the time, many labs, including NIST, were using this junction technology for single-flux-quantum logic circuits, because the junctions were the most reproducible and they were non-hysteretic. PJVS operation required single-valued, stable, constant-voltage steps that were possible with such shunted junctions, which had electrical characteristics very different from those used in the conventional Josephson voltage standard (JVS). I simulated a number of prototype circuits for Clark's PJVS, including circuits in which the microwave bias was inductively coupled to series junctions or series SQUIDs. I chose not to fabricate series arrays with these inductively coupled circuits, since they would have required multilayered wiring, significant chip area per junction, and complicated microwave designs.

The first PJVS prototype circuit that I fabricated used direct-driven series arrays of junctions. In order to further simplify the layout, I chose to shunt each pair of junctions with a single shunt resistor. Although this circuit appeared to work correctly in simulation, the measured current-voltage characteristics (I-V curves) of the prototype circuit showed only half the expected voltage, indicating that only one junction in each shunted pair entered the voltage state. This result taught me the importance of including stability analysis in simulations and the importance of measuring real circuits! Three years later, and after much more research, Clark, Charlie Burroughs and Richard Kautz made and measured the first PJVS circuit with multiple arrays and with all (individually-shunted) junctions contributing to the output voltage. In research and development there usually are many false starts and lessons learned before the correct approach is apparent, as will be seen throughout this chapter.

During the early 1990s, a number of laboratories around the world were working on intrinsically shunted junctions with high-temperature superconductors (HTS). It was clear that the PJVS circuit would be much simpler and have higher junction density if the junctions were intrinsically rather than externally shunted. At that time, and it remains so today, it was difficult in HTS technology to fabricate a large number of junctions with sufficient uniformity to produce practical voltages. During my graduate research with Chris Lobb and Mike Tinkham, I had gained experience

with superconductor-normal-superconductor (SNS) junctions. With the help of Martin Forrester and Horst Rogalla, I fabricated two-dimensional (2D) arrays of SNS in-line Josephson junctions with thin-film niobium islands patterned on top of a copper film. The Nb was deposited with a magnetron sputtering head that Horst built in Giessen. The Nb islands were patterned using a custom-made reactive-ion etching chamber. Having observed interesting quantum effects in these 2D circuits with planar SNS junctions, which were not particularly uniform, I was optimistic that planar trilayer SNS junctions might produce sufficiently uniform series arrays for the PJVS because the barrier would be defined by the normal-metal film thickness instead of a lithographically defined Nb gap having length of about 1 μm. However, most of my more experienced colleagues, including Richard Harris, were much less optimistic, and one expert insisted that SNS junctions simply would not work. This pessimism was well founded because the current density of SNS junctions depends exponentially on the barrier thickness.

Richard Kautz calculated in April, 1994, that SNS junctions would be feasible with regard to appropriate electrical characteristics. He showed that high I_cR_n products would be difficult to achieve with AuPd and noted that higher resistivity materials would be needed for operation at frequencies of at least 70 GHz, the frequency typically used for the conventional JVS. I used AuPd as the barrier material in my first Nb-based SNS junctions, because I had recently implemented it as the resistor material for our single-flux-quantum (SFQ) digital circuits, because it had higher resistivity than that of InAu. Two challenges with producing these junctions were (a) modifying the wet aqua regia[86] gold etch to adequately remove the Pd, and (b) increasing the current density of the Nb wiring contacts to the junction's Nb counter electrode. By November, 1994, I successfully fabricated a wafer of test chips that had series arrays of junctions with different areas and uniform electrical characteristics. Figure 9.24 shows I-V curves of the first uniform arrays that produced constant voltage steps with an applied microwave bias. The Shapiro steps are greater than 1 mA and are surprisingly flat[87], even though the junctions were not embedded within a microwave circuit and the microwaves were radiatively coupled to the test circuit with a wire coil in close proximity. Sometimes research and development produces unexpectedly favorable results.

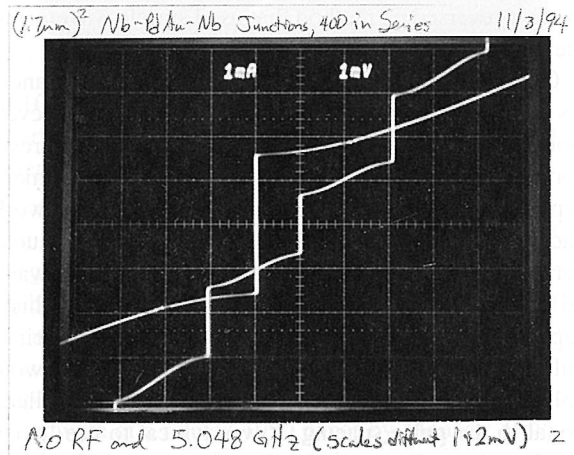

FIGURE 9.24: 1994 photo of the oscilloscope I-V curves of the first "uniform" 400-junction SNS array of Nb-AuPd-Nb trilayer junctions with (2 mV/div) and without (1 mV/div) microwave bias. The I-V curve without microwaves was exposed after moving the origin and changing voltage scale (1 mV/div). I_c = 1.5 mA, R = 5.5 mΩ/JJ, (1.7 μm)², and 43 nm thick AuPd.

The first 1 V PJVS circuit based on SNS junctions was demonstrated in 1995. It contained 32,768 junctions and implemented coplanar waveguide microwave designs, including filters and impedance-matching elements, and custom DAC bias electronics. The intrinsically stable steps were a unique feature, which allowed us to conceive, for the first time, of a turn-key Josephson voltage standard that could be fully automated to produce arbitrary voltages. For the next ten years at NIST,

[86] Aqua regia is a highly corrosive mixture of nitric and hydrochloric acids.

[87] Flat means constant in voltage over a large current range, which is called the "operating margin".

we applied the PJVS primarily to applications requiring stable and accurate dc voltages, such as supporting the watt balance experiment for measuring Planck's constant (see the next section) and helping Yi-Hua Tang build a new dc voltage dissemination chain, which allowed NIST to retire its traditional electrochemical standard cells.

With regard to ac synthesis with the PJVS, continued research on the SNS and the resistively shunted junction circuits showed that the slow ~300 ns rise times of the transitions between the quantized voltage steps limited the uncertainty of root-mean-square (rms) voltage measurements with the PJVS multi-bit stepwise-approximated waveforms, especially for the target frequencies above 1 kHz that were of primary interest for ac-metrology. However, interesting and useful rms measurements were performed at lower frequencies by Hitoshi Sasaki and Burroughs and separately by PTB researchers, who used SINIS-junction PJVS circuits[88] (see the preceeding section by Kohlmann). Both experiments characterized the frequency response of a thermal converter[89] with the fast-reversed dc method that used simple waveforms with only three voltages, which minimized the transient effects.

On the morning of July 26, 1995, John Przybysz and Hodge Worsham, superconducting electronics colleagues from Westinghouse Research and Development Center in Pittsburgh, visited NIST, Boulder. They presented to Clark and me their interests in developing DACs and analog-to-digital converters (ADCs) for U.S. Navy applications. I remember that the discussion began with the concept of waveform synthesis by switching between two Josephson voltage levels, similar to what we had demonstrated with the PJVS system, but with much faster sampling rates. We already knew that perfect quantization was compromised in stepwise waveforms, due to transients. However, we were all involved in research on SFQ digital circuits, which controlled the movement of SFQ through superconducting integrated circuits and changed their quantum states with properly timed junction pulses. Clark pointed out that waveform synthesis would be intrinsically accurate if the quantized voltage pulses of the junctions were exactly controlled and the resulting voltage would be proportional to the pulse spacing. It was typical to use "average voltage" measurements to characterize the time-dependent pulsed-voltage outputs of SFQ circuits. Semiconductor pattern generators were suggested as a possible bias signal because they could produce pulse waveforms by programming either of two voltages, depending on a digital pattern stored in memory. We realized that Josephson arrays could produce quantum-accurate waveforms by biasing them with a digitally controlled pulse waveform.

I was thrilled to have participated in this creative process, which required complementary expertise from all parties, and generated a potentially useful and important new idea. That afternoon I hunted for and found an HP8082A pulse generator[90] with an appropriately short, 2 to 10 ns pulse width that was capable of 10 to 250 MHz pulse repetition rates. The next morning I successfully produced quantum-accurate dc voltages with 100 μA margins by pulse biasing an SNS array circuit from a prototype PJVS design. It was very exciting to have experimentally realized the pulse-driven bias technique within 24 hours of conception. This was a critical first step toward demonstrating accurate ac waveform synthesis. I was also able to show that the step voltage changed with pulse period and that the current range of the step decreased with wider pulses, due to the frequency response of the junctions. Only the smallest array (the PJVS least significant bit) with 512 junctions (each having I_c = 1.9 mA, R = 4.4 mΩ, and (2 μm)^2 area) showed steps because of insufficient uniformity of the pulse signal in the longer arrays.

[88] A SINIS junction is formed with layers of superconductor-insulator-normal metal-insulator-superconductor.

[89] Thermal converters are rms detectors that determine the equivalence between alternating current (ac) signals and direct current (dc) signals by measuring the difference in their heating values.

[90] Commercial instruments are identified in this paper only to adequately specify the experimental procedure. Such identification does not imply recommendation or endorsement by the NIST, nor does it imply that the equipment identified is necessarily the best available for the purpose.

Figure 9.25 shows the first 265 μV voltage step that was produced with the pulse-driven array at the fastest 250 MHz pulse rate. The pulse amplitude was adjusted to center the first constant-voltage step on the zero-current axis. The voltage was correct for the number of junctions and the pulse frequency, and corresponded to exactly one quantized Josephson voltage pulse for every input pulse. The higher voltage steps are for higher order quantization (n = 2 and 3 Josephson pulses for every input pulse).

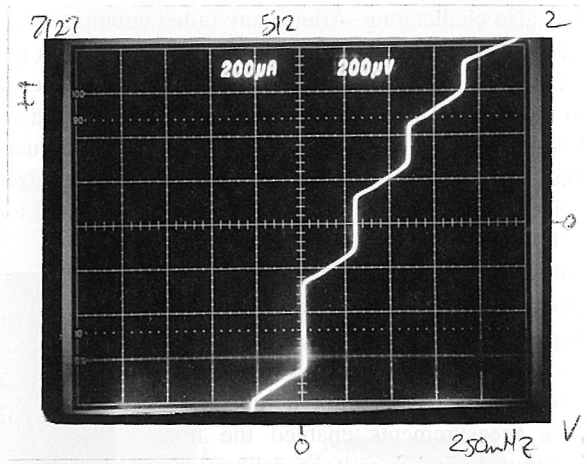

FIGURE 9.25: First pulse-biased SNS array I-V curve of 512 series-connected junctions showing flat steps that indicated reasonable pulse uniformity.

Flat steps were larger than expected, for two reasons. First, the 250 MHz pulse frequency was much slower than the 4 GHz junction characteristic frequency, so that the current ranges of the steps were inherently small, due to the junction response. Second, the pulse waveform reaching each junction was probably not uniform because the PJVS circuit had multiple bias taps with filters designed for 11 GHz. This PJVS circuit was intentionally chosen because it didn't contain on-chip blocking capacitors, which would have blocked the low-speed pulse drive. Sometimes your best available resources (such as the circuits and pulse equipment, in this case), can still produce useful results.

A few days later, I discovered the 1996 paper by Maggi that showed his simulations of pulse-driven junctions. For many months, we were unaware of a related 1990 paper by Monaco. Both of these researchers were interested in "step-width" enhancement of zero-crossing steps, not waveform synthesis, for increasing the current range of dc voltages. Maggi's simulations gave us confidence that our experimental results were reasonable. I began my own simulation investigation of pulse-driven junction dynamics by modifying one of Kautz' FORTRAN programs[91] and characterizing the junction response with different pulse-drive and junction parameters, including different pulse shapes. Research then shifted to understanding digital waveform synthesis (with Richard Schreier's delta-sigma modulator Matlab programs) and oversampling techniques, and characterizing the performance of state-of-the-art commercial pattern generators. This research gave me an acute appreciation of the broadband nature of our pulse-drive waveforms and how significantly more challenging it would be to ensure that all junctions receive the same pulse bias as compared with the single-frequency continuous-wave (CW) biases of both the PJVS and conventional JVS. It became necessary to develop lumped-element filters and other microwave circuit techniques that were appropriate for broadband waveforms and our specific applications.

Increasing the rms voltage to at least 100 mV was the greatest challenge to making the ACJVS a useful system. At lunch one day in the NIST cafeteria, Charlie Burroughs and I were discussing different schemes to produce bipolar pulses. On a napkin we sketched I-V curves and pulse waveforms. We considered combining the two-level pattern generator signal with a CW microwave signal and speculated that pulses of both polarities might be possible if the CW frequency were 3/2 that of the pattern generator's clock. Charlie arrived the next morning with calculated combined waveforms that showed bipolar pulses. Experimentally combining the two bias waveforms required creativity, such as minimizing attenuation of the two-level pattern generator signal by using a microwave coupler (in reverse). Developing techniques to optimize the phase and amplitude of the two bias signals

[91] FORTRAN is a programming language widely used for scientific computing, especially in the previous century.

was also challenging. After many failed attempts to achieve operating margins, we finally synthesized the first bipolar pulse-driven sine wave with quantum-based accuracy, as shown in Figure 9.26. We found that the −52.7 dBc second harmonic and lower-amplitude third harmonic were due to nonlinearities of the differential preamplifier and spectrum analyzer measurement instruments. Every junction in this array produced exactly one quantized voltage pulse for every input pulse, so that the first perfect bipolar sine wave was synthesized with no measureable distortion above the noise floor (more than 90 dB below the fundamental tone).

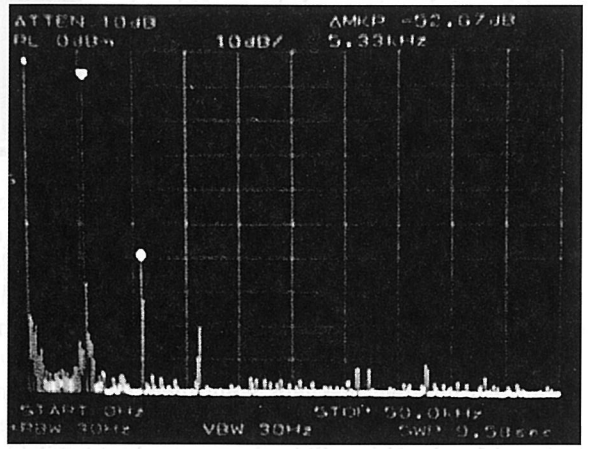

FIGURE 9.26: First spectrum (2/25/1998) that demonstrated operating margins of an ACJVS-synthesized bipolar sine wave and with the largest amplitude to date of 13.4 mV rms — 95 % of peak amplitude waveform, 1000 junctions biased with a 6.44 GHz clock and 9.66 GHz microwave drive.

It took many more years of technology development in fabrication, microwave circuit design, and bias techniques before circuits were able to produce useful 100 mV sine waves. Automating the ACJVS for ac-dc difference measurements enabled the first quantum-based ac voltage calibrations in 2007. Also during these many years of development Paul Dresselhaus, Yonuk Chong, Nicolas Hadacek, and many other collaborators helped improve the fabrication process and experimented with new barrier materials. The barriers we found that produced the most uniform and reproducible junctions were high-resistivity metal-silicides. These barriers enabled us to increase output voltage for both the ACJVS and PJVS circuits. The maximum rms output voltage of the ACJVS is currently 275 mV. We also worked with a number of collaborators and companies to produce custom pattern generators that had more memory and performance optimized for the ACJVS. A German company, Sympuls LLC, now makes a ternary pulse pattern generator that directly generates bipolar pulse waveforms, which they developed in collaboration with our metrology colleagues at the NMi Van Swinden Laboratory in The Netherlands.

Understanding the limitations (and especially the systematic errors) of Josephson voltage standard systems is extremely important, and influences the measurement techniques used for a particular application. The most important step in ensuring that a Josephson system is producing an accurate voltage is demonstrating that it produces the same voltage for a range of values for every bias parameter. Even if a measured voltage appears repeatable and can attain a low uncertainty, it can still be inaccurate! The accuracy also depends on systematic errors, such as thermal voltages (for dc signals) and ac signals from other sources (electromagnetic interference or bias-related signals) or unexpected circuit paths (especially for frequencies greater than 100 kHz). Other effects that compromise the accuracy of measured voltage waveforms include the frequency response of the output transmission line, voltages induced from bias signals driving the inductance of the superconducting wiring between the junctions, nonlinearities from wiring connections (that produce distortion), and signals produced by the digitization process, which are particularly detrimental in rms measurements.

Some of the above challenges to measurement accuracy were reinvestigated beginning in 2005 as researchers again attempted to make rms measurements of PJVS stepwise waveforms at frequencies up to 2 kHz. It was hoped that a bias source with a faster 100 ns rise time that enabled shorter transients would reduce rms measurement uncertainties. Burroughs and other NIST colleagues showed

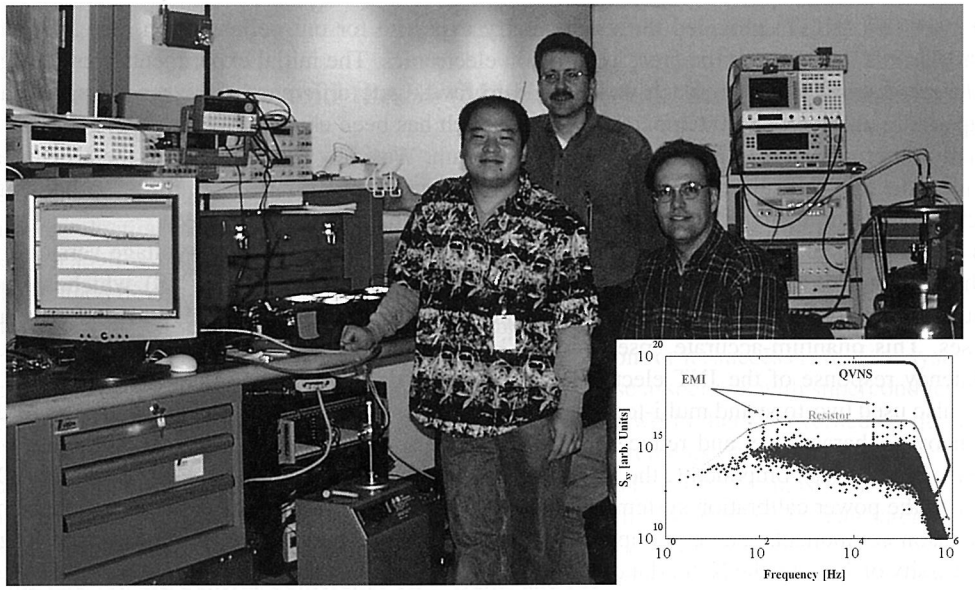

FIGURE 9.27: First (November, 2001) cross-correlation measurement (left monitor display) with NIST Johnson noise thermometry electronics (on bench). Pictured are Sae Woo Nam, Wes Tew, and Sam Benz. The sense resistor probe is in the water cell inside the thermoelectric cooler (on the floor). The ACJVS system is in the upper right. Inset shows the first published spectra of the resistor and QVNS signals and challenges with EMI.

that the uncertainty of rms measurements of stepwise waveforms, even with rise times as short as 20 ns, was still limited by bias offsets and also by other bias parameters that influence the shape of an array's I-V curve, such as the applied microwave power. These "flat spot" measurement results convinced most researchers to focus on sampling measurement techniques, which can eliminate transient and bias-related errors when stepwise waveforms are measured.

In parallel with the rms investigations, Waldemar Kürten Ihlenfeld and Luis Palafox and colleagues used stepwise waveforms and direct sampling to calibrate the digital voltmeter and demonstrated the technique for power calibration. In 2005, Ralf Behr et al. proposed a differential sampling method with a PJVS voltage reference. Alain Rüfenacht and collaborators optimized and demonstrated this differential sampling technique by characterizing ac sources. At frequencies up to 200 Hz, the lowest uncertainty for a commonly used commercial voltage source was a few parts in 10^7, which was limited by the stability of that source. An order of magnitude lower uncertainty was found when comparing the multilevel stepwise waveforms of two PJVS signals (one source and one reference). In 2008, Waltrip et al. developed a new power calibration system for NIST that used differential sampling and an integrated PJVS as the voltage reference. The most challenging research aspects for this system were developing the stable semiconductor synthesized source, the permuting dividers, and the differential measurement technique. Frequently, when implementing a quantum system in a new application, the challenges may lie in integration or other instruments or components required for the measurement.

Finally, I would like to mention my favorite application of quantum-based waveform synthesis. It is my favorite because it has been and continues to be challenging, has required many smart and capable collaborators, and exploits quantum-accurate waveform synthesis in a completely new area for me, namely thermometry. In 2000, John Martinis conceived of improving Johnson noise thermometry (JNT) with quantum-based waveforms because they could provide a calculable, accurate, pseudo-noise voltage reference. Rod White (Measurement Standards Laboratory, New Zealand)

and Wes Tew (NIST) provided the thermometry expertise for our collaboration. Sae Woo Nam, with Martinis, constructed the cross-correlation electronics. The initial experiments were designed to demonstrate the new approach to JNT and to investigate differences between thermodynamic temperature and the ITS-90 temperature scale, which has been characterized primarily by gas and radiation thermometry. In Figure 9.27, Sae Woo Nam, Wes Tew and I pose with the JNT apparatus after the first measurements. More recently, we focused our JNT research toward producing an electronic measurement of Boltzmann's constant k_B at parts in 10^6 uncertainty.

The unique aspect of our JNT measurement technique is the use of a low-voltage version (only eight junctions) of the ACJVS, called a "quantized voltage noise source" (QVNS), which is used to synthesize a waveform constructed from harmonic tones of identical amplitudes and random relative phases. This quantum-accurate "pseudo-noise" waveform is used to characterize the amplitude-frequency response of the JNT electronics over its 1 MHz Nyquist measurement bandwidth. We have also used two-tone and multi-tone waveforms synthesized with both the QVNS and the ACJVS to uncover, characterize, and reduce nonlinearities by revealing the distortion in both active and passive electronics components, the input transmission lines and wiring, and the sampling ADCs. As with the power calibration system, the most difficult aspects of the JNT experiment are the non-Josephson components, namely, improving the low-noise measurement electronics. Horst Rogalla (University of Twente, the Netherlands), Jifeng Qu (National Institute of Metrology, China), Alessio Polarollo (Istituto Nazionale di Ricerca Metrologica, iNRiM) and Chiharu Urano (AIST/National Metrology Institute of Japan) are recent guest researchers working on the NIST JNT experiment and their improvements are now yielding a measurement of Boltzmann's constant with an uncertainty less than 12 μK/K.

In conclusion, there are two different quantum-based ac voltage sources that produce either step-wise approximated waveforms (PJVS) or perfect digital-to-analog conversion (ACJVS). New measurement techniques that use these systems have been developed and demonstrated for ac voltage and power applications. These systems and measurement techniques have the potential to shift the paradigm for measuring ac signals from one based on rms detectors to one based on intrinsically accurate voltage sources. The present region of impact in ac voltage metrology for each of the two systems is indicated in Figure 9.28. The uncertainties displayed in this plot, which are based primarily on rms detection with thermal converters, are those offered in 2010 by the NIST ac voltage calibration service, which is used for calibrating thermal converters and voltage sources. The Josephson systems should be able to improve upon these uncertainties by at least an order of magnitude, and this has already been demonstrated at a number of frequencies and voltages. In order to fully realize the paradigm shift to quantum-based voltage sources, additional technology development will be required to improve the Josephson systems and measurement techniques, particularly in bias electronics and system automation. I am optimistic that the remaining technical challenges will be overcome, as usual, through collaborative interactions between the metrology and superconducting electronics researchers working in this field.

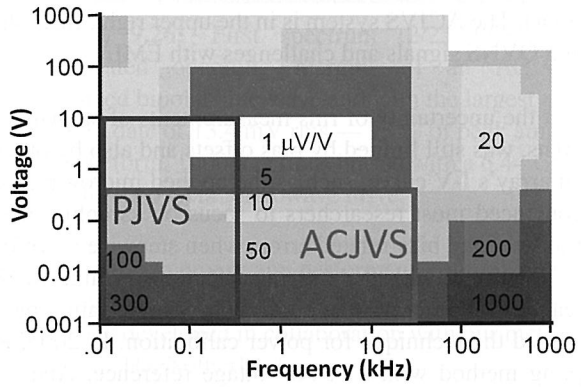

FIGURE 9.28: Voltage vs. frequency plot showing the uncertainty boundaries (in units of μV/V) for ac voltage calibrations at NIST (courtesy of T. Lipe and J. Kinard, NIST). Boxes indicate regions presently impacted by the PJVS and ACJVS quantum-based voltage sources.

9.9 Superconductivity and the SI (Metric) System Based on Fundamental Constants

Edwin Williams and Ian Robinson

Superconducting measurements that help connect the unit of mass, the kilogram, to the Planck constant h are bringing the time when the scale for all units in the International System of Units (SI) can be defined directly through fundamental and atomic constants. The metric system, now known as the SI, has served science, engineering and commerce very well since it was adopted internationally at the signing of the Treaty of the Meter in 1875. One reason for its success is that the system is adaptive to change. New science and technologies, such as those associated with superconductivity, have provided scientists with a connection between the atomic world that is governed by quantum mechanics and the more familiar world of macroscopic measurements of voltage and current. We need to extend this link to the kilogram, which is defined as the macroscopic mass of a metal cylinder made of platinum-iridium that, since 1889, has been kept in a vault at the Bureau International des Poids et Mesures, BIPM, in Sèvres, a suburb of Paris. In 1967 developments in atomic timekeeping allowed the General Conference on Weights and Measures (CGPM), an intergovernmental organization which oversees the SI, to set the scale for the second by fixing the value of the ground-state hyperfine transition frequency of the cesium 133 atom. Likewise in 1983, advancements in optical frequency measurements allowed the CGPM to fix the value of the speed of light, c, which, in conjunction with the previously defined second, sets the scale for the meter. In this section we describe experimental progress of "watt balance determinations" that measure, in terms of the current definition of the meter, kilogram and second, accurate values of the Planck constant, h; from which can be derived both the electron charge, e; and the Avogadro constant, N_A. Sufficiently accurate measurements of h, e, and N_A will allow the scale of the units kilogram, ampere, and mole to be set by fixing the value of these three constants.[92,93] Then, the watt balance experiment, or similar ones, will be used to realize or maintain the unit of mass, much like atomic clocks presently maintain the unit of time. Of course, as in the past, we will ensure that the values chosen for these constants will minimize any discontinuity with the existing scale of the units. One clear advantage of this new SI is that the constants controlling the voltage and resistance scales will have fixed values.

Worldwide voltage measurements can be traced back to calibrations made using the Josephson effect, which produces a voltage dependent only on the Josephson constant $2e/h$ and frequency, as has been discussed earlier in this book. Likewise, accurate resistance measurements are calibrated against a quantum of conductance e^2/h (the inverse of the von Klitzing constant h/e^2), using the quantum Hall effect[94]. A current can be measured as the number of elementary charges, e, flowing per second via the voltage drop across a resistance measured in terms of the values of the Josephson and von Klitzing constants, respectively. However, in the SI, the unit of current is defined by the force between two wires and therefore must be related to the macroscopic kilogram mass standard. Experiments that presently measure the values of h or N_A in terms of the kilogram, if sufficiently accurate, can easily be reversed to measure mass in terms of fixed values of these constants. As the constants h and N_A are related by an expression that is more accurate than the present uncertainties of either h or N_A, one set of experiments can be used to provide a check on the other. At present, the two techniques display similar accuracies with the promise of even better accuracy in the future. A number of laboratories in the world are building, and will be operating, independent watt balance experiments; this will provide the significant advantage that results can be compared, and

[92] I. M. Mills, P. J. Mohr, T. J. Quinn, B. N. Taylor, and E. R. Williams, *Metrologia* 43 (2006) 227.
[93] E. R. Williams, *IEEE Trans. Instrum. Meas.* 56 (2007) 646
[94] K. von Klitzing, G. Dorda, and M. Pepper, *Phys. Rev. Lett.* 45 (1980) 494

then combined, to maintain the global mass scale with greater accuracy than any of the individual experiments.

The watt balance uses the quantum Hall resistance and the Josephson volt to measure virtual electrical power in an experiment that equates virtual mechanical (SI) power to virtual electrical power. This is accomplished in a two-stage process, one stage using a balance that compares the force on a coil in a magnetic field to the force of gravity on a kilogram mass. The second stage is a clever technique suggested by Bryan Kibble[95], which allows us to measure the quantity that relates the force and the current in the first part of the experiment, which depends on the magnetic field and geometry of the coil, by moving the coil in the field at a measured velocity and measuring the induced voltage. The heart of the apparatus is a coil of wire of effective length l, which is suspended in a strong magnetic flux density B that is arranged to produce a vertical force $F = Bli$ when a current i is passed through it. This force is compared to the weight, mg, of a mass m by suspending the coil and mass from one arm of a precise balance. The product Bl is measured by moving the coil vertically with a velocity u and measuring the generated voltage $v_m = Blu$. By combining the two measurements, the virtual electrical power $v_m i$ can be equated to the virtual mechanical power mgu. These measurements can be used to calculate the Planck constant (see Eq. (5) in Williams et al.[96]), or the Introduction in Robinson[97]) and thereby reduce the uncertainties of many other fundamental constants, including the values of the SI elementary charge and the mass of the electron. The NIST watt balance apparatus will be used to illustrate a few details.

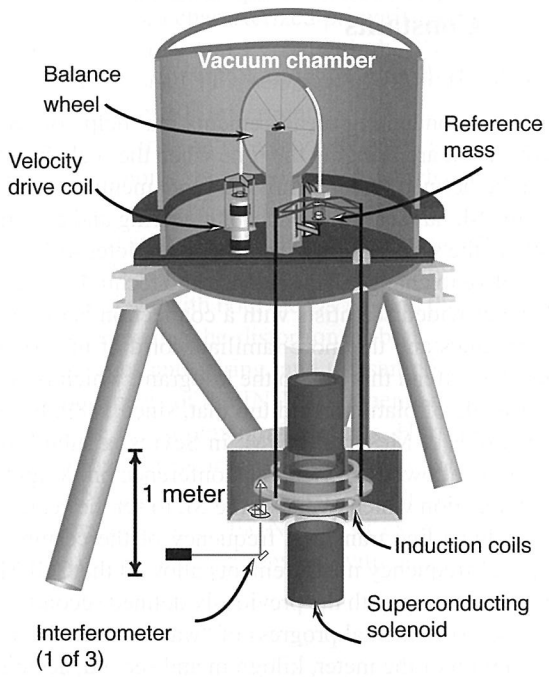

FIGURE 9.29: This two-story apparatus, the NIST watt balance, is used to measure h and calculate the electron mass and other atomic masses and constants.

Figure 9.29 shows the configuration of the experiment. The axial force on a loop of wire in a purely radial field ($\mathbf{B} = [B_a(z)/r]\hat{\mathbf{r}}$, where $B_a(z)$ is nearly constant with vertical displacement, z, and time) is independent of the wire shape. A superconducting magnet consisting of two solenoid sections (shown in blue) wound in opposition produces a 0.1 T radial field outside the magnet Dewar. $B_a(z)$ varies by +150 μT/T from the center over a ± 40 mm vertical displacement, maintaining this variation over days. Because the field, and not the flux, must be constant, the magnet is operated in a constant-current mode with 5.6 A flowing in the series-connected solenoid sections.

The magnet has 200,000 turns and an inductance of 5000 H. Three induction coils, the center coil with 2376 turns and the upper and lower coil each having half that number, are located in the radial

[95] B.P. Kibble, in *Atomic Masses and Fundamental Constants*, J. H. Sanders and A. H. Wapstra, Eds., vol. 5. New York: Plenum (1976) 541

[96] E. R. Williams, R. L. Steiner, D. B. Newell, and P. T. Olsen, *Phys. Rev. Lett.* 81 (1998) 2404

[97] I. A. Robinson, *IEEE Trans. Instrum. Meas.* 58 (2009) 942

field. The lower and upper induction coils are fixed to the support structure of the balance, and the center moving induction coil is attached to a wheel balance located above the Dewar. The wheel balance, induction coils and their connecting rods are all in one vacuum system that is separate from the Dewar vacuum. Aligning the magnetic field perpendicular to gravity, and the inductive coils to the field, is essential, so that all forces and velocities measured are vertical. Thus, the balance is a 31 cm radius wheel that operates like a pulley, where the inductive coils, mass standards, and countermass hang from flat bands of 50 strands of wire rolling on the wheel, allowing the coil to move strictly vertically for 100 mm as the wheel rotates ±10 degrees. The five degrees of freedom for the induction coil, other than vertical, are monitored, and excitations are damped. This monitoring of coil motion plus some mutual inductance techniques are used to align the experiment and to estimate the alignment errors.

For the velocity phase of the measurement, no mass standards are on the pans, and a small force on the countermass side is applied, via an auxiliary coil and permanent magnet, to produce a velocity u of about 2 mm/s that generates a constant voltage v_m (1.018 ± 0.001) V across the moving induction coil. We synchronously measure the time, the voltage difference between the moving and fixed induction coils, and the distance between these coils, eliminating voltage and motion common to both. Three interferometers, spaced equally apart on the coils, record the coil center-of-mass position, while three digital voltmeters integrate voltage against a Josephson volt standard between successive position readings with less than 200 ns dead time. The interferometry is performed in vacuum. The resulting v_m/u ratio has a vibration related noise of about 0.002 % and must be extensively averaged. The $B_a(z)/B_a(z = 0)$ variation is measured with 650 v_m/u measurements timed uniformly over 85 mm travel. The field's z-dependence is modeled with an eighth order orthogonal polynomial from hundreds of curves measured daily, which is then used in calculating the temporal changes ($\pm 0.1\ (\mu B_a/B_a)/h$) for each v_m/u ratio at the position where the weighings are made. A set of 10 up and 10 down velocities takes 30 minutes.

In the balance phase, a tare weight of 500 g placed on the countermass pan is balanced by a −10.18 mA servo current in the induction coil. As the 1 kg PtIr standard mass is placed on and off the pan, the moving induction coil current is reversed whilst causing minimal rotation of the balance. The reversal of the flow of the current through the 100 Ω standard resistor causes the voltage across its potential terminals to change between ± 1.018 V. The change is measured by comparison to voltages generated by a Josephson junction array. The four-terminal value of the resistor is known via calibration against a quantum Hall resistance standard. Five mass on-off sequences take 30 minutes. The result of each weighing phase is combined with the results of the before and after moving phases to produce a single measurement of the Planck constant or equivalently SI power. Both phases of the measurement have equivalent relative statistical uncertainties of 0.02 μW/W.

There are eight active experiments in progress in the world today that are planned to measure h, e, and N_A accurately. Six are watt balance type experiments: five at national measurement institutes, NMIs, of Canada (transferred from Great Britain in 2009), US, Switzerland, France and New Zealand, and one is at the BIPM. These six watt balance experiments each involve significant differences in design from the others, and we refer the reader to a summary report.[98] The most accurate watt balance measurement to date was reported by NIST,[99] but others may soon report even better results. The NMI of China is designing an energy balance experiment that measures the magnetic field and geometry by measuring mutual inductance gradients rather than measuring the voltage and velocity of a moving coil.[100] The eighth approach does not involve superconductivity or accurate electrical measurements. The AVOGADRO Project, an international collaboration involving research laboratories in Germany, Italy, Australia, Japan, Belgium, and the US, is measuring the

[98] I. A. Robinson, *IEEE Trans. Instrum. Meas.* 58 (2009) 942

[99] R. L. Steiner, E. R. Williams, R. Liu, and D. B. Newell, *IEEE Trans. Instrum. Meas.* 56 (2007) 592

[100] Z. Zhang, Q. He, and Z. Li, in *Proc. Conf. Precision Electromagn. Meas. Dig.* (2006) 126

number of atoms in a kilogram sphere made from an isotopically pure ^{28}Si crystal.[101,102] Agreement between the AVOGADRO Project and the seven experiments that involve superconductivity will demonstrate the universality of the measurements. At present, the AVOGADO project and the watt balance method display similar accuracies with the promise of even better accuracy in the future. A number of laboratories in the world are building, and will be operating, independent watt balance experiments; this will provide the significant advantage that results can be compared, and then combined, to maintain the global mass scale with greater accuracy than any of the individual experiments.

Figure 9.30 shows the results of a number of measurements, which have been transformed to yield the measured value of the Planck constant normalized to the value of the Planck constant h_{90} derived from the conventional values of the Josephson and von Klitzing constants K_{J-90} and R_{K-90}. There have been inconsistencies between the NIST watt balance, the NPL (National Physical Laboratory, Great Britain) watt balance, and the Avogadro results, but results presented at conferences but as yet unpublished (shown with a * in Figure 9.30) indicate that better agreement is being reached as possible sources of error are investigated in each of these experiments. Further results are expected and consistency will be the key to when a redefinition will occur. You will notice that the h_{90} value used to maintain the volt will not need a large adjustment when a redefinition occurs. The 1990 value h_{90} was a weighted average, and the breakthrough measurement at NPL[103] had the dominant weight. Figure 9.31 compares the changes in the sister copies of the International Prototype of the Kilogram, IPK, with a few hundred measures of the Planck constant made over four years, using the NIST watt balance. The IPK has been compared with its sister copies just twice in the last century. The Planck constant data uses a one kilogram Pt-Ir mass standard that was made and measured at the BIPM in 2004 and is periodically measured against the NIST Pt-Ir mass standard to provide a link back to the IPK. Tests are continuing at NIST to detect any systematic errors in the results. The vertical scale has the same sensitivity for both, but the IPK data cover 100 years, while the NIST data cover 4 years. The IPK data are not statistical noise, but are a measure of real differences between the IPK and its sisters. These differences, plus the fact that we must wait a half-century between calibrations of the world's mass standards against the IPK, are a driving force behind the move to an SI that includes fixed values of the three constants h, e, and N_A.

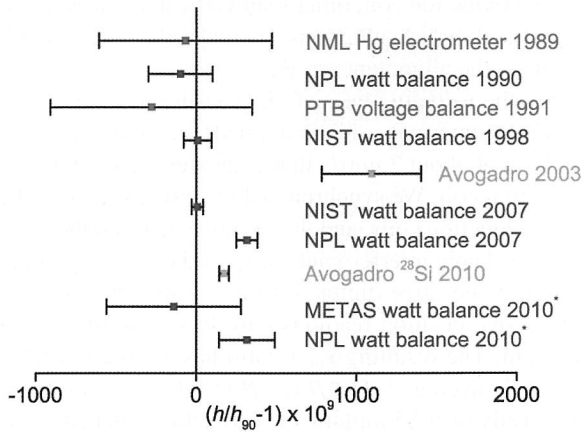

FIGURE 9.30: Measurements of the Planck constant h (Federal Office of Metrology, Switzerland).

The connection between the quantum phenomena and the electrical measurements was first discovered 100 years ago. We are still learning new ways of using these phenomena to make our scientific world a better, more accurate community. The CGPM has the final authority to change the

[101] K. Fujii, A. Waseda, N. Kuramoto, S. Mizushima, P. Becker, H. Bettin, A. Nicolaus, U. Kuetgens, S. Valkiers, P. Taylor, P. De Biévre, G. Mana, E. Massa, R. Matyi, E. G. Kessler, Jr., and M. Hanke, *IEEE Trans. Instrum. Meas.* 54 (2005) 854

[102] B. Andreas, Y. Azuma, G. Bartl, P. Becker, H. Bettin, M. Borys, I. Busch, M. Gray, P. Fuchs, K. Fujii, H. Fujimoto, E. Kessler, M. Krumrey, U. Kuetgens, N. Kuramoto, G. Mana, P. Manson, E. Massa, S. Mizushima, A. Nicolaus, A. Picard, A. Pramann, O. Rienitz, D. Schiel, S. Valkiers, and A. Waseda,"An accurate determination of the Avogadro constant by counting the atoms in a ^{28}Si crystal," (2010) published on the web at http://arXiv.org/abs/1010.2317v1

[103] B. P. Kibble, I. A. Robinson and J. H. Belliss, *Metrologia*, vol. 27, pp. 173-192, 1990.

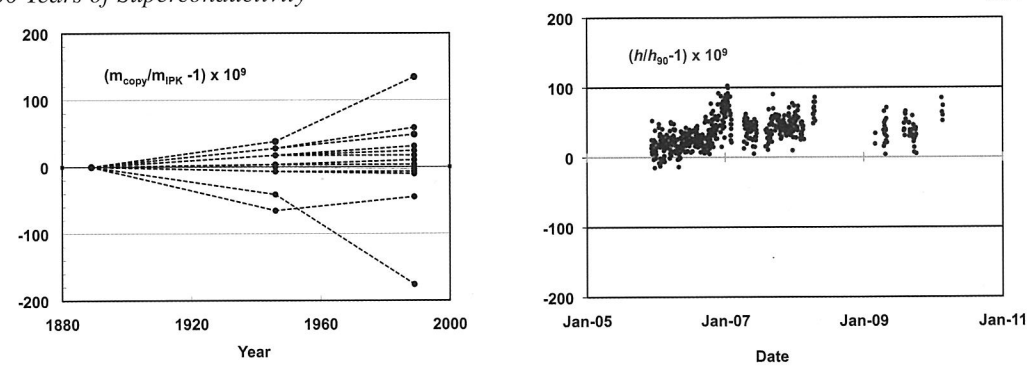

FIGURE 9.31: Historic comparisons of Pt-Ir kilograms (left) and a series of measurements of the Planck constant at NIST (right).

SI, and the scientific committees that advise them are recommending that e, h, and N_A be used as the constants to be fixed, but they have not yet recommended a timetable.[104] The CGPM meets every four years, and late 2011 will be the next one. The advantages of an SI based only on the constants of nature were foreseen by J. C. Maxwell in 1870, and, with the help of the quantum properties of superconductors, we are only now on the brink of achieving this goal.

9.10 Further Reading

For readers interested in more detailed discussion of metrology using quantum effects in superconductors, the following review papers may be helpful. They also contain many additional references to original literature.

1. R. A. Kamper, Superconducting devices for metrology and standards, in *Superconductor Applications: SQUIDs and Machines*, edited by Brian B. Schwartz and Simon Foner, Plenum Press (1976) 189.

2. J. Niemeyer, Josephson voltage standards, in *Handbook of Applied Superconductivity*, edited by B. Seeber, vol. 2, Institute of Physics, Philadelphia, PA (1998) 1813.

3. C. A. Hamilton, Josephson voltage standards, *Rev. Sci. Instrum.* 71 (2000) 3611.

4. R. L. Kautz, Design and operation of series-array Josephson voltage standards, in *Metrology at the Frontier of Physics and Technology*, edited by L. Crovini, T.J. Quinn, North-Holland, Amsterdam (1992) 259.

5. S. P. Benz and C. A. Hamilton, Application of the Josephson effect to voltage metrology, *Proc. of the IEEE* 92 (2004) 1617.

6. B. Jeanneret and S. P. Benz, Application of the Josephson effect in electrical metrology, in *Proceedings of the International School on Quantum Metrology and Fundamental Constants*, Les Houches, France (2007), edited by F. Piquemal and B. Jeckelmann, published jointly by EDP Sciences and Springer Verlag in *The European Physical Journal Special Topics* 172 (2009) 181.

[104] Andrew Wallard, *Metrologia* 47 (2009) 103

10

Medical Applications

Editor: Harold Weinstock

10.1 Introduction

Harold Weinstock

Of the many applications of superconductivity that are found in this volume, there is only one with which the general population in developed countries has any major contact. I refer, of course, to magnetic resonance imaging, or as it has become generally known, MRI. By some estimates, this is a greater than $5B per year enterprise with companies in Europe, Asia and the US involved in marketing their MRI systems to the medical community. There are other biomedical applications of superconductivity that will be covered in this section, some that have been around for as long as (or even longer than) MRI has. However, for reasons that are mostly nontechnical, these other applications have had rather limited success in developing a significant market. In some instances, these markets may never develop because of continuing improvements in other technologies that are less expensive and/or that require less training of medical technicians. Yet there is one application, namely magnetocardiography, that surely will find widespread use as a diagnostic tool for routine screening of otherwise undetected heart ailments and for triage in hospital emergency rooms when patients appear with chest pain. The only caveat to this prediction is that the development of other non-cryogenic, less expensive and equally sensitive magnetometers could replace SQUID-based magnetocardiography. Nevertheless, it is the use of SQUID magnetometry that has opened the door to magnetocardiography and that has served to prove its effectiveness in numerous clinical studies

around the world. Furthermore, the introduction of closed-cycle refrigeration should make SQUID-based magnetometry more user friendly. In the end, reliable operation and overall cost (including shielded enclosures for the non-cryogenic systems) will determine which form of magnetometry becomes universally adopted. There have been many previous attempts to preempt SQUID technology with non-cryogenic forms of magnetometry, but, thus far, SQUID systems have maintained a clear advantage for sensitivity and reliability.

For the most part, biomedical applications can be divided into 2 major categories, those that are based upon (1) superconducting magnets, e.g., MRI and particle accelerators for cancer therapy, and (2) SQUID-based magnetic gradiometers, e.g., magnetoencephalography (MEG) and magnetocardiography (MCG). There is yet another application that uses superconducting pick-up coils to produce sharper MRI images when applied to human limbs. Finally, in this introduction, it is worth noting that there is a new form of MRI that operates at low magnetic fields (not requiring superconducting magnets), but that utilizes SQUID magnetometry to yield images that are competitive in some instances with those produced by conventional high-field MRI.

In this introduction focus on some extraordinary individuals whose vision gave rise to these biomedical applications of superconductivity. First, I would like to acknowledge 2 gentlemen who were in large measure responsible for the development of the superconducting magnet industry. I doubt whether either of them would have considered that one day the companies they founded would be characterized as "big business." I refer to Sir Martin Wood, who, along with his wife Audrey, founded Oxford Instruments (OI) in 1959 in their garden shed, and Carl Rosner, who with Paul Swartz, was "spun off" by General Electric (GE) to form Intermagnetics General Corporation (IGC) in 1971 to work primarily on construction of superconducting magnets. At the time of formation of these companies, the main customer base for superconducting magnets was university and government laboratories engaging in mostly basic and some applied research. The advent of MRI in the late 1970s changed all that dramatically. You can read about the development of MRI in the section of this chapter written by Jim Bray and Kathleen Amm. You will note their mention of the skepticism of some GE scientists regarding the penetration of the magnetic field into the human body. It was assumed that inside the body the field would be less than at the surface and perhaps somewhat distorted. Carl Rosner has recently confirmed that IGC's first order in 1979 for a superconducting magnet that was large enough for a human body to fit into its bore, came from the University of Wisconsin Medical School. IGC ultimately delivered the requested magnet, but Carl stated that at a price of $50,000 IGC probably lost money on the deal. In June of 2006 IGC was sold to Royal Philips Electronics for $1,300,000,000. In 1982 OI spun off its large-magnet manufacturing division into Oxford Magnet Technology (OMT), and in 1989 Siemens purchased 51% of OMT from OI. In November 2003 Siemens purchased the remaining 49% of OMT, and renamed the company Siemens Magnet Technology in June 2004. The first whole-body magnet built by OI in 1979 was a conventional resistive electromagnet, and just a year later it manufactured its first superconducting whole-body magnet. I recall a plenary talk that Sir Martin Wood gave at the 1994 Applied Superconductivity Conference in Boston. He recounted a profile of him and OI by a financial newspaper. The article he quoted referred to him as a rather odd CEO who wore sandals on his feet and drove an 11-year-old automobile. He then said he still wears sandals and that the car he drives was then 18 years old. He concluded by listing about 5 or 6 well-known international companies and concluded by saying that the previous year OI had declared a profit that was greater than that of all of the companies listed combined.

In citing people who have made a difference, I would like to mention Ed Edelsack, an Office of Naval Research (ONR) program manager who in the late 1960s had initiated programs in superconducting electronics and biophysics. In doing so, he was the catalyst that brought Jim Zimmerman together with David Cohen. At that time Jim was a scientist employed by the Philco-Ford Corporation, although he left shortly thereafter to help form a company, SHE (standing for Superconducting Helium Electronics), and he then moved to the National Bureau of Standards (now NIST) in 1970. Ed was funding David Cohen at MIT's Francis Bitter National Magnet Laboratory under his biophysics program, and was funding Jim Zimmerman under his superconducting electronics program. The son of a medical doctor, Ed had a keen interest in trying to employ the then-new SQUID sensors to detect signals emanating from the human body. In late December of 1969, Cohen, Zimmerman and Edelsack came together to test the ability of Zimmerman's RF SQUID (co-invented with Arnold Silver) to detect signals from the human heart and the human brain under the favorable conditions created inside the magnetically-shielded room recently constructed by Cohen. The ability to detect a magnetic signal from the human heart using a SQUID was accomplished on December 31, 1969. Later, other signals from the brain were observed using either the same shielded room at MIT by Cohen or a SQUID-based magnetic gradiometer as initially developed by Jim Zimmerman and N. V. Frederick.

Ed Edelsack continued his interest in exploring medical applications of SQUID gradiometry and arranged for the purchase of a commercial (single-channel) second-derivative SQUID-based gradiometer by the Naval Research Laboratory (NRL) in the hope that he and Marty Nisenoff at NRL could take it to some nearby medical center. Somehow they could not make the right connections with the medical community. Meanwhile, I had started to work for ONR part-time from Chicago in late 1979, and after some time, Ed provided funding that helped me take sabbatical leave at NRL from my academic position in Chicago. While the primary goal of the planned research with the SQUID gradiometer was in other areas, Ed encouraged me to seek interest from the National Institutes of Health. After a couple of abortive attempts I made contact with the Director of the Epilepsy Branch of the National Institute for Neurological Diseases and Stroke (NINDS). He saw the potential of the SQUID to move forward in locating "interictal spikes" noninvasively, as opposed to removing part of the skull and inserting numerous electrodes for several days. Over a period of a few months I worked with NINDS scientist/physicians and support engineers to help establish the potential for evaluation of epileptic patients. As my sabbatical year was ending, NINDS placed an order with BTi (the new name for SHE) for the first 7-channel system to be built. It will become clear from reading the section of this chapter on magnetoencephalography (MEG) that working with a 7-channel system unshielded, one reduces the time required to produce a magnetic map of the brain, but it is not at all close to what can be done with systems with over 200 channels operating in a shielded room. Nevertheless, an employee of BTi told me the order from NINDS brought new life to that company and to the field of MEG more generally.

Finally, I wish to cite an individual who made an enormous contribution to the field of MEG, namely Sam Williamson of New York University (NYU). Sam had a remarkable career in a variety of areas of physics, but his greatest influence was in MEG. He pioneered this field somewhat by accident, as his training was in low temperature condensed matter physics. At NYU at some faculty social event he met Lloyd Kaufman, a cognitive psychologist. From this chance meeting, the field of MEG emerged. Working with a single-channel system in a building sitting above an underground train line and without shielding, Williamson and Kaufman gave birth to MEG. One of Sam's favorite lines was that if they could obtain valid measurements at NYU, then it could be done anywhere. As their results became known, visiting scholars from around the globe came to engage in research at NYU and then returned to their home institutions to set-up their own MEG systems. Within a short time Sam had a joint appointment in the NYU Medical School. Sam looked for other neurological SQUID applications and mentioned the possibility of using MEG to learn more about Alzheimer's Disease. Sadly he was diagnosed with this disease when he was approaching 60 years of age. He had enough foresight to take early retirement. His collaborator, Lloyd Kaufman, himself recently retired then, arranged a 60th birthday, retirement event that drew dozens of senior scientists and former students from everywhere that MEG was being done. It was a truly stirring tribute. One of his former students spoke of how much Sam had meant to him, and not knowing of Sam's affliction, pleaded for him not to retire.

To end on a happier note, I wish to mention one of Sam Williamson's more amusing achievements. It seems that an acupuncturist realized that one of his needles had broken and that part of it was in his patient's body, although he didn't know exactly where. X-rays and MRI scans were

of no help. Finally, someone recalled the work being done at NYU. Surveying the patient's body with the SQUID gradiometer, the embedded needle was located. It had to be removed by a surgeon. Afterwards a short article was prepared for publication in which the patient was referred to as Mr. Haystack.

I offer one final observation. In editing the various sections of this chapter, I realized that a considerable amount of the text involved medical terminology, some of which was foreign to me, even though I've had significant contact with the medical community. Since most of the readers of this book will be physical scientists and engineers, I either removed some of the more esoteric sections or provided some explanatory addenda. I somewhat suspect that this does not endear me to the authors, nor will it endear me to the readers without a strong connection to the biomedical community. Such is the nature of compromises. Despite this caveat, I invite the readers to enjoy the wonderful biomedical applications of superconductivity. Some have yet to reach their full potential, but all of them are quite interesting in my humble opinion.

10.2 Medical Applications of Magnetoencephalography

Cosimo Del Gratta, Stefania Della Penna, Vittorio Pizzella and Gian-Luca Romani

10.2.1 Introduction: The Origin of Magnetoencephalography

The first successful attempts to reveal magnetic signals generated by neural activity in the human brain were performed in the mid 1960s, and were carried out using a non-superconducting detector. The quality of those signals was, however, very poor and certainly inadequate for any possible medical use. The first measurement of a good-quality magnetic signal associated with human cerebral spontaneous activity (alpha rhythm) was carried out only at the very end of 1969. What had happened in that four-year time span? Indeed, in 1969 there were two important developments: i) Jim Zimmerman, a leading physicist in the field of low temperature physics and superconductivity, had invented (with Arnold Silver) the radiofrequency (RF) biased SQUID[1], creating the most sensitive magnetometer of its time; ii) David Cohen had built an efficient 5-layer magnetically-shielded room at MIT, thus providing a dedicated and necessary environment to detect the weak magnetic signals associated with bioelectric currents in the human heart and eventually in the brain. Cohen and Zimmerman were brought together by Ed Edelsack, a program manager at the Office of Naval Research with programs in superconductivity and biophysics. As a result, in late December 1969, the first superconductivity-based human magnetocardiogram was obtained, and a related paper was published a few months later[2] (see Figure 10.1).

At that time few people other than the 3 authors of that article would have imagined that this measurement had marked a milestone, opening a new avenue to the study of the brain. This, however, became more evident less than 2 years later, when David Cohen recorded the first good quality magnetoencephalogram (MEG) inside the same shielded room (see Figure 10.1c) using a commercial SQUID[3]. After this second paper, the interest of several scientists — mostly physicists — was aroused, and a number of laboratories started studying the brain with this new tool.

After this brief historical overview, it is appropriate to dwell a little on the reasons that made the detection of cerebral magnetic signals so challenging in view of the fact that its electric counterpart,

[1] J.E. Zimmerman et al., *J. Appl. Phys.* 41 (1970) 1572.

[2] D. Cohen, E.A. Edelsack, J.E. Zimmerman, *Appl. Phys. Lett.* 16(1970) 278.

[3] D. Cohen, *Science* 175 (1972) 664

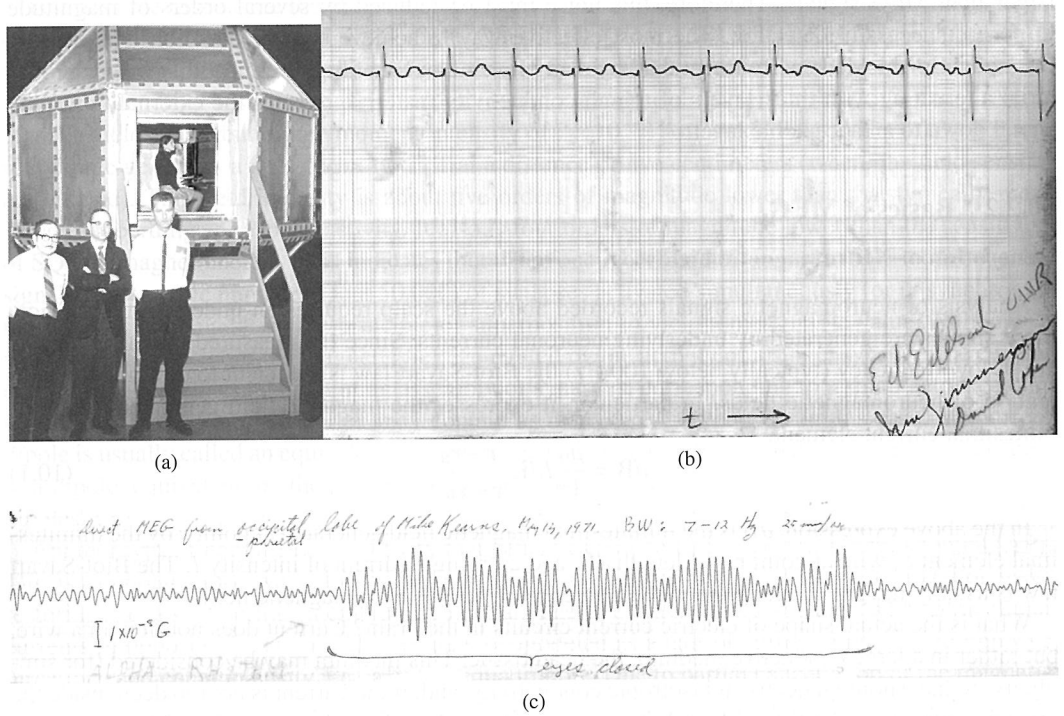

(a) (b) (c)

FIGURE 10.1: (a) Ed Edelsack, David Cohen and Jim Zimmerman in front of the MIT shielded room in December 1969. The first low-noise magnetocardiogram had been recorded therein using Zimmerman's SQUID. The long-tail glass dewar which contained the SQUID, is visible inside the room. (b) The first magnetocardiogram recorded in the MIT shielded room. It is signed by Edelsack, Zimmerman and Cohen. (Courtesy of David Cohen) (c) First MEG measured with a commercial SQUID, in the MIT shielded room (May, 1971). The subject's eyes were open at the beginning of the trace, then closed, resulting in the high amplitude alpha rhythm, then open again. (Courtesy of David Cohen)

the electroencephalogram (EEG), had first been recorded forty years earlier. As we shall see in the following paragraph, intracellular currents flowing inside neurons, the primary source of the magnetic signals, are indeed quite small, and the intensity of the generated fields strongly decrease with distance. Since detection occurs outside the scalp, the effective intensity of the field generated by a single neuron is extremely small, being of the order of a few attoteslas. Fortunately, the actual signals that are measured are generated by coherent activity of many thousands (or more) of neurons, and the overall field intensity reaches values of tens to hundreds of femtoteslas. An extremely sensitive detector is required to reveal such tiny fields, and no room-temperature device can provide such performance. The SQUID, however, immediately demonstrated an unrivaled sensitivity (as detailed elsewhere in this book) and, equally important, a wide operational bandwidth extending down to quite low frequencies, thus permitting satisfactory detection of the magnetic signals associated with cerebral activity, the frequency bandwidth of which typically spans from 0.1 to 100 Hz.

The existence of a sufficiently sensitive detector was only a partial solution to a two-fold problem, since one typically is required to measure this extremely small MEG signal in an extremely noisy environment. As will be seen, the amplitude of ambient magnetic noise is relatively quite large in a typical laboratory or hospital. For example, the earth's magnetic field, which is of the order of 50 μT, undergoes fluctuations in the low frequency range that can be several orders of magnitude

larger than MEG signals. Therefore, this noise must be reduced by several orders of magnitude to permit successful detection. The most effective way to achieve such a reduction is to build a magnetically-shielded environment that, by using several layers of high-permeability magnetic material alternating with thick layers of a high-conductivity material, reduces the external unwanted signal down to an acceptable level.

10.2.2 Basics of MEG

Generation of Neuromagnetic Fields

Analysis of neuromagnetic signals recorded above the scalp requires an understanding of how these signals are generated by underlying neuronal currents. Since the measured magnetic signals are of low frequency (typically below 100 Hz) the Biot-Savart law is sufficient to describe the generation of neuromagnetic fields. In particular, it expresses the magnetic field generated by an infinitesimal current element.

$$d\mathbf{B} = \frac{\mu_0}{4\pi} I d\mathbf{L} \frac{\mathbf{r} - \mathbf{r_0}}{|\mathbf{r} - \mathbf{r_0}|^3}. \tag{10.1}$$

In the above expression, dB is the infinitesimal magnetic field generated at point $\mathbf{r}$ by the infinitesimal element of wire at point $\mathbf{r_0}$, of length $d\mathbf{L}$, and carrying a current of intensity I. The Biot-Savart law is usually integrated along the wire in order to obtain the total magnetic field.

What is the actual shape of electric current circuits in the brain? Current does not flow in a wire, but rather in a large conductive medium, the head tissue. This medium may be considered (for simplicity) to have homogeneous and isotropic conductivity, and, if the current is not too deep inside the brain, we may consider the medium boundary, i.e., the scalp, where the magnetic field is measured, to be plane and infinite, while more accurate models of the conductive medium will be described later. The current carriers are, on one hand, ions driven by neural activity in the intracellular space or across the cell membrane, and, on the other hand, free ions moving in the extracellular space in response to an electric field. We view the first type of ion flow as an active current, directly related to neural signaling. This current is usually called the impressed current. The other type of ion flow is a passive current, generated by the electric field resulting from charge distribution over the cell membrane. This current is usually called the volume current. Together, the impressed and volume currents close the loop to satisfy the principle of conservation of charge.

Given this complex current pattern, finding an expression for the neuromagnetic field appears to be a difficult task. Fortunately, to a good approximation, the magnetic field generated by volume currents is tangential to the scalp surface, while the magnetic field generated by impressed currents is orthogonal to the scalp surface. This property is rigorously true if the conductive medium is plane or spherical, as will be seen later, but it only approximates a real head. The contribution of volume currents can be neglected if one measures only the magnetic field component orthogonal to the scalp. Then one only needs to calculate the field of the impressed current. In the simplest case, that of a post-synaptic potential (PSP), the impressed current is the minute current flowing in a neuron dendrite due to membrane depolarization (or hyperpolarization) after neurotransmitter intake at the synapse. The PSP may be modeled as a small current element similar to the infinitesimal current element in the Biot-Savart law. Such a current element is called a current dipole and is represented by a vector, the current dipole moment, the direction of which is the current direction, and the magnitude of which is the product of length and current intensity (usually expressed as Am):

$$\mathbf{Q} = I\mathbf{L}. \tag{10.2}$$

According to the Biot-Savart law, the magnetic field generated by a current dipole is then

$$d\mathbf{B} = \frac{\mu_0}{4\pi} \frac{\mathbf{Q} \times (\mathbf{r} - \mathbf{r_0})}{|\mathbf{r} - \mathbf{r_0}|^3}. \tag{10.3}$$

Is it possible to measure the magnetic field of a PSP? First, one must estimate the intensity of the corresponding current dipole moment. From Ohm's law, $Q = \sigma A \Delta\Phi$, where σ is the conductivity of the intracellular medium, A is the cross-section of the dendrite, and $\Delta\Phi$ is the potential difference along the dendrite. Inserting typical values (1 μm = dendrite diameter, $\sigma = 0.25\,\Omega^{-1}\mathrm{m}^{-1}$, $\Delta\Phi$ = 10 mV) yields a current dipole moment intensity of 2×10^{-15} Am. According to Eq. 10.3, this current dipole generates a field of 3×10^{-19} T at a distance of five centimeters (where the field sensors are located). This field intensity is about five orders of magnitude lower than that typically measured in recordings of evoked activity. It also is four orders of magnitude lower than the sensitivity of SQUID magnetometers. This indicates that when one records neuromagnetic fields, one receives signals from a large number (about 50,000) of synapses activated simultaneously (or in synchrony), the fields of which add via the principle of superposition to yield a measurable value. Although it is not possible to record the magnetic field generated by the activity of a single synapse, the current dipole is still useful as a model of an assembly of synapses, corresponding to a small activated cortical patch, since 1 mm^2 of cortex may contain as many as 10^8 synapses. In this case, the current dipole is usually called an equivalent current dipole (ECD) to emphasize that it is a macroscopic current dipole, equivalent, by the principle of superposition, to a large number of microscopic current dipoles.

Another type of neural electric activity that generates magnetic fields is the action potential (AP). This is a depolarization wave flowing along the axon of a neuron, followed by a repolarization wave restoring the rest state transmembrane potential. The two waves are associated with intracellular currents in opposite directions. The AP may be modeled as a pair of current dipoles with opposite directions and equal intensity, i.e., a current quadrupole. Due to partial cancellation of the magnetic fields generated by the two current dipoles, the current quadrupole generates a total magnetic field an order of magnitude smaller than that of the current dipole. Although it is possible to detect the magnetic field of an AP from a single exposed axon in an animal model, as well as of APs from nerve fibers in the human noninvasively (e.g., above the arm), magnetic fields of APs from cortico-cortical or cortico-spinal connections have never been observed, likely due to weak signals and a lack of synchronicity. In summary, with MEG one is mostly sensitive to synaptic activity, and it requires several tens of thousands of synapses to be active synchronously to detect them. This large number of synapses may be modeled as an ECD. Therefore, the ECD is the basic current pattern in the brain with regard to MEG measurements.

What does the magnetic field of a current dipole look like? One may use the above equation for the magnetic field of a current dipole to calculate the orthogonal component of the magnetic field over the plane boundary of the conductive medium described earlier. Note that, if the current dipole is orthogonal to the boundary, its magnetic field will be parallel to the boundary and therefore will have no orthogonal component. In fact, for an orthogonal current dipole, the total magnetic field, including the field of volume currents, vanishes, as may be shown using Ampère's theorem applied to a circular loop centered over the current dipole and parallel to the boundary. This shows that MEG is mostly sensitive to currents flowing parallel to the scalp, while it is weakly sensitive to currents flowing orthogonally to the scalp. We shall comment on this in a later section, but for now we calculate the orthogonal component of the magnetic field of a current dipole parallel to the plane boundary. We use an orthonormal coordinate system with its origin on the boundary, the z axis orthogonal to the boundary, pointing outwards, and the x and y axes on the boundary. Let the current dipole Q lie on the z axis at a depth d below the boundary, and oriented parallel to the x axis. The 2D map of the orthogonal component of the magnetic field over the boundary is obtained from Eq. (10.3):

$$B_\perp = \frac{\mu_0}{4\pi} \frac{Qy}{(x^2 + y^2 + d^2)^{3/2}} \tag{10.4}$$

where x and y are the coordinates of a point on the boundary, and the current dipole lies at a depth d below the origin. This map is shown in Figure 10.2. Note that the magnetic field map has a maximum

and a minimum for $x = 0$ and $y = d/\sqrt{2}$, and for $x = 0$ and $y = -d/\sqrt{2}$, respectively. The distance between these extrema is $d\sqrt{2}$, so it is proportional to current dipole depth, and is independent of the current dipole moment. Both extrema lie on the y axis, so that the current dipole is at right angles to the straight line joining the extrema, and lies halfway between the extrema. This shows that, given the position of the extrema, one can readily find the location of the current dipole. The intensity of the current dipole may then be calculated from the value of the field at the extrema, which is proportional to Q/d^2. Note also from Eq. (10.4) that the magnetic field above the current dipole vanishes, while its spatial derivative along the line joining the extrema is maximal. In summary, from an analysis of the magnetic field map over the scalp, one can infer the location of the currents in the brain.

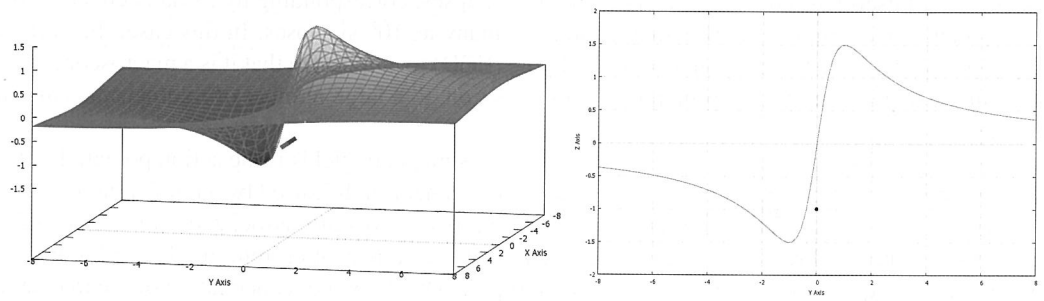

(a) (b)

FIGURE 10.2: Map of the orthogonal component of the magnetic field of a current dipole in a homogeneously conducting half-space. The boundary is in the xy-plane at z = 0, and is not shown on the figure. Units are arbitrary. The coordinates of the dipole are (0,0,-1). Left: 3D representation of the graph of function (2.4). Right: the same function along the y-axis.

Although the procedure is more complex than indicated in this simple account, as will be described later, the above equations provide the principle of 3D localization of neural activity using MEG.

Instrumentation

Detection Coils

Usually, the MEG field is measured by means of a superconducting detection coil (made of Nb) coupled to a low T_c SQUID. The main reasons for not using SQUIDs alone are:

i) The SQUID inductance should be as small as possible since its energy resolution is proportional to it — the energy resolution is $\epsilon \approx 9kTL_{\mathrm{SQUID}}/R$ for a typical low-T_c SQUID.

ii) The geometry of the detection coil can define the spatial sensitivity of the instrument.

The first issue suggests that the SQUID loop should be as small as possible ($\approx$ 100 pH), but this strategy is not adequate to measure MEG signals since the sensitivity to sources in the human brain would be dramatically reduced. Indeed, if the magnetic field generated by a current dipole is measured, the flux sensitivity of a loop is $\Phi = CA_1Q/r^2$, where Q is the source strength, r is the distance of the source from the loop, A_1 is the loop area and C is a constant. For typical values, loops with a diameter of the order of a centimeter should be used to increase the device effective area and

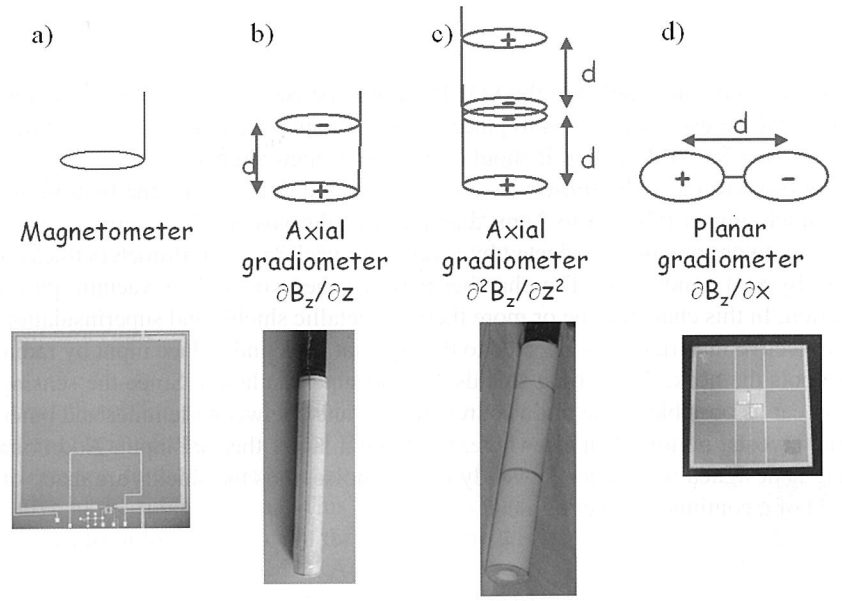

FIGURE 10.3: Schematic drawing and related pictures of a) magnetometer integrated on the same chip as a SQUID; b) wire-wound, first-order axial gradiometer; c) wire-wound, second-order axial gradiometer; d) two orthogonal planar gradiometers integrated on the same chip as the SQUID.

thus obtain a signal above device noise. The second issue suggests that the geometry of a MEG channel can be arranged to be sensitive to brain sources while rejecting background noise at the same time. Typical coils used to detect MEG signals are simple magnetometers, axial gradiometers and planar gradiometers, as shown in Figure 10.3. The magnetometer is a single or multi-turn loop whose flux sensitivity (as discussed above) indicates that this detection coil measures the signal generated by near and far sources, including environmental noise. Gradiometers are made of two or more magnetometers wound in opposite directions and displaced by a baseline d. Specifically, the loops of axial gradiometers are displaced along the loop axis, whereas in planar gradiometers the displacement is coplanar with the loops. Gradiometers provide reduced sensitivity to faraway sources, such as environmental and subject's noise (i.e., the heart signal). If we consider a first-order gradiometer as an example (Figure 10.3 b), the total signal is the difference between the flux detected by the lower coil (closer to the MEG source than to the noise source) and the flux detected by the upper one (far from both the MEG source and noise sources). The gradiometer principle is that noise has virtually the same value in both coils, with opposite signs, and therefore cancels. On the contrary, the source signal is much lower in the farther-away coil, due to the decay of signal with distance, and therefore does not cancel. How does one select the proper geometry for the MEG channels? The answer depends on the specific environment, since magnetometers pick up the signal of shallow and deep sources in the brain together with environmental noise, whereas gradiometers reject ambient noise, but suffer from a reduction of sensitivity to deep brain sources[4]. Magnetometers and planar gradiometers can be integrated on the same chip containing the SQUID, whereas axial gradiometers are made of Nb wire wound on a non-magnetic support (usually MACOR).

[4] Romani et al., 1982, NATO ASI series, for an extensive review.

Cryogenics

The MEG detection coil coupled to the SQUID should be cooled below the critical temperature of Nb (9.3 K), and the usual strategy is to place them in a bath of liquid helium at 4.2 K. The main feature of a cryostat for MEG is that it should be made of non-magnetic material, e.g., fiberglass. In addition, in order to place the sensors as close as possible to the scalp, the bottom of the cryostat must be much thinner (about 1 to 2 cm) than for typical cryostats. The cryostat consists of one reservoir and an outer container connected by a very thin neck (a few millimeters thick), to reduce thermal input by heat conduction. The chamber between the two shells is vacuum-pumped to reduce convection. In this chamber one or more thermal metallic shields and superinsulation made of blankets of reflective material are connected to the cryostat neck and reduce input by radiation. The boil-off gas cools the neck, the thermal shields and the superinsulation. Since the sensing channel should be as near as possible to the brain source, the distance between the inner and outer shells is smaller at the cryostat bottom than elsewhere, implying a larger thermal input. Additionally, thermal shielding is designed to produce low eddy-current noise, thus the shields are made of metallic stripes instead of a continuous sheet of metal.

Shielding

Since environmental noise can be up to 6 orders of magnitude higher than the brain's magnetic field, the use of magnetometers would be impaired and the operation of gradiometers would be troublesome. Additionally, RF interference could prevent the SQUID from being stable. To overcome this issue a MEG channel can be operated inside a magnetic shield. RF interference can be locally shielded by copper sheets wrapped around individual channels or around the cryostat itself. Alternately, since local shields can introduce eddy-current noise, a channel may be placed inside an RF-shielded room made of aluminum walls placed far from the sensor. Low-frequency shielding is based on high-permeability magnetic sheets, such as μ-metal, forming a room containing the MEG sensor and the subject to be investigated. The shape of the room determines the shielding factor, which is better for spherical rooms than for cubic ones, the latter being easier to fabricate. Additionally, the larger the number of concentric layers comprising the room, the better is the shielding. In summary, a shielding factor greater than 10^5 above 100 Hz and 10^2 at 0.01 Hz can be constructed using concentric layers of high-permeability materials and one layer for RF shielding. Magnetometers can be effective only with the use of high-quality shielding, e.g., a shielding factor greater than 200 at 0.01 Hz.

Read-out Electronics

The common scheme to drive the SQUID of a MEG channel is the flux locked loop (FLL), used to obtain a linear output from the SQUID. Negative feedback is used to stabilize the operating point of the SQUID. Many variants of the FLL scheme have been adopted, each aimed at improving the noise, dynamic range and/or bandwidth. Flux modulation has been used extensively in MEG sensors. Generally, a modulating flux with an amplitude about $\Phi_0/4$ is applied to the SQUID, the output of which is amplified and processed by means of a lock-in detector, utilizing the flux modulation frequency as the reference frequency. The resulting signal, which is the feedback signal, is a linear function of the flux difference $\Phi_{err} = \Phi_e - n\Phi_0/2$. The bandwidth required for MEG recordings is from DC up to a few kHz, whereas environmental background determines dynamic range, which may be as large as tens of nanoteslas.

Acquisition system

The read-out electronic unit is interfaced to an A/D converter (ADC) driven by a personal computer. Usually the ADC input range is matched to the sensor output, and ADCs with 20 to 24 bits are used to provide quantization noise[5] that is less than SQUID noise. The ADC includes a low-pass filter applied to sensor output to avoid aliasing, i.e., the passband of the sensor should be at most one half of the sampling frequency. Additionally, signal preconditioning, such as bandpass filtering, decimation and rejection of power-line noise, are available and can be applied by the operator.

Measurement procedure

One critical factor for practical MEG recording is subject positioning. It is necessary to know the position of the subject with respect to the sensor to co-register a reference system relative to the subject's head. This allows the operator to locate the physiological source of the magnetic field in the subject's brain with the aid of MRI. A typical set-up for subject positioning consists of a set of small coils—at least 3—placed on the subject's head at known positions, typically corresponding to anatomical landmarks. The coils are energized by an AC current before and after the recording session or even during it, provided that the frequency of the driving current is well above the band of cerebral signals. During the recording of the coil signals and the related brain signal, the subject is cautioned to keep his/her head stationary.

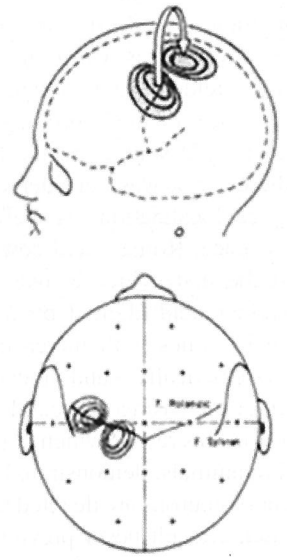

FIGURE 10.4: First attempt to measure a somatosensory magnetic field, evoked by electric stimulation of the thumb of the right hand. Note the spatial field distribution and the field direction over the somatosensory cortex. (modified from Brenner et al. [8])

10.2.3 First MEG Studies

Following the initial results described in Section 1, many groups worldwide began to study the brain using these newly developed SQUID-based detectors. Foremost among them was the neuromagnetism group at New York University (NYU) led by Sam Williamson, a physicist, and Lloyd Kaufman, a cognitive psychologist. That group produced several important publications, not only in basic research, but also in the area of modeling. Indeed, in 1975—almost contemporaneous with Cohen's group[6]—the first visually-evoked fields were detected by Brenner and coworkers[7] at NYU, using a 10-Hz flickering grid as a stimulus. Some years later the same authors measured somatotopically-evoked fields under steady-state stimulation of the thumb and of the little finger, providing a first hint of a possible somatotopy of the corresponding sources in the contralateral primary somatosensory cortex[8]—see Figure 10.4.

---

5 A.V. Oppenheim and R.W. Schafer. *Digital Signal Processing*, Prentice-Hall, Inc.: Englewood Cliffs, NJ, 1975.

6 D. Cohen D, *IEEE Trans. Magnetics*. MAG-11 (1975) 694

7 D. Brenner et al., *Science* 190 (1975) 480

8 D. Brenner et al., Science 199 (1978) 81

In 1978 the first auditory-evoked magnetic field was measured by Martin Reite and coworkers[9], and in the two following years some progress in the field was achieved by Farrell and coworkers in Detroit[10], and by Elberling and coworkers in Denmark[11].

It is worth stressing that this first decade of MEG measurements was characterized by studies that substantially replicated, from a magnetic point of view, studies that had been carried out earlier using EEG, thus demonstrating the existence of the magnetic "counterpart" of an electric cerebral signal associated with neuronal activity. This last statement is not meant to diminish the value of those first MEG findings; rather it is meant to indicate that the potential of the magnetic approach was not yet fully understood. Advances were made shortly thereafter by Williamson and Kaufman[12], who provided a theoretical analysis of the origin of neuromagnetic fields, their properties, and how they affect source localization.

It was only after this theoretical advance that in 1982 Romani, Williamson and Kaufman were able to demonstrate the existence of tonotopic organization of the human auditory cortex. It is worth noting that this research yielded the first demonstration of the capability of the neuromagnetic method to identify 3D sources in the human brain, and therefore it was considered a milestone in source localization, as well as in basic neuroscience. Romani and coworkers[13] presented the first evidence that the source of the evoked field elicited by auditory stimulation by tones with increasing frequency are systematically—and logarithmically—located at increasing cortical depth (see Figure 10.5). This result, which is similar to that found in animals, demonstrated that an equal number of neurons are devoted to each octave of sound, a result never previously obtained with EEG. Now researchers are accustomed to whole-head multichannel systems. Back in the early 1980s, in order to obtain data with a single-channel instrument in an unshielded environment and produce a signal map over the entire scalp with sufficient detail to allow source localization, it required many hours of data acquisition (often at night to reduce environmental noise). Imagine the stress for the volunteer subjects! Another major paper was published by the NYU group in 1982: an extensive review of biomagnetic instrumentation and modeling that in the years since has been considered a useful tool for both experts and

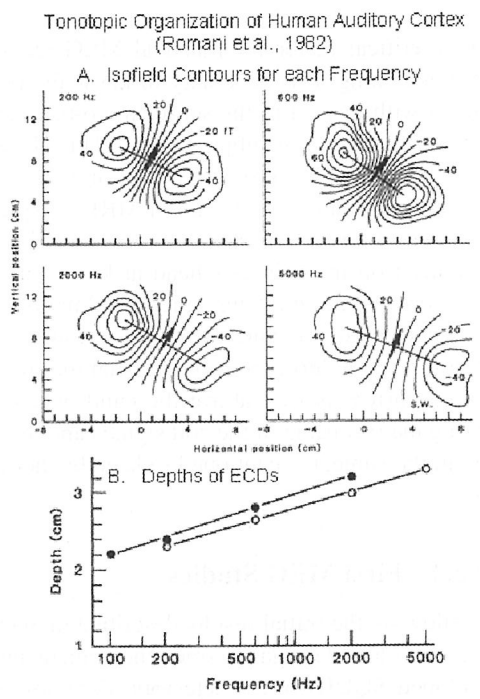

FIGURE 10.5: Upper: Isofield contours recorded over right hemisphere of subject SW. Arrows reflect position and orientation of sources for 200, 600, 2000, and 5000 Hz tones. The origin is at the ear canal. Lower: Depths of equivalent current dipoles (ECDs) for 2 subjects as a function of the logarithm of the frequency. Modified from Romani et al., 1982[9].

[9] M. Reite, J. Edrich, J. T. Zimmerman, J. E. Zimmerman, *Electroenceph. Clin. Neurophysiol.* 45 (1978) 114
[10] D. E. Farrell, J. H. Tripp, R. Nogren, T. J. Teyler, *Electroenceph. Clin. Neurophysiol.* 49 (1980) 31
[11] C. Elberling, C. Bak, B. Kofoed, J. Lebech, K. Soermark, *Acta Neurol Scandinav* 65 (1982) 553
[12] S.J. Williamson, L. Kaufman, *Mag. and Mag. Mat.* 22, (1981) 129
[13] G.L. Romani et al., *Science* 216 (1982) 1339

newcomers to the field[14].

Other studies performed in the ensuing years using similar localization procedures yielded new results in complementary fields: Maclin and coworkers[15] observed — albeit qualitatively — retinotopic organization of the visual cortex; Okada and coworkers[16] revealed somatotopic organization of the somatosensory cortex, namely the somatosensory homunculus, and Hari and coworkers[17] observed signals originating from the (human) second somatosensory cortex. All of these new observations were later confirmed and extended using commercial instruments as well as self-made sensors, as the number of groups becoming involved in this "new" field of research was growing. New results were generated around the world, and with international collaboration. For example, an investigation of the spontaneous cerebral alpha rhythm was carried out in Rome in 1983 by Chapman and coworkers, providing the first tentative identification of widespread generators inside the occipital cortex.

In Figure 10.6 we see most of the experimenters participating in that study depicted around the self-constructed system featuring a DC SQUID for sensing.

FIGURE 10.6: Some of the researchers working in the biomagnetics group at the Solid State Institute of the National Research Council in Rome in 1983. (second and third from left: Cosimo Del Gratta and Vittorio Pizzella; sixth and seventh: Bob Chapman and Gian Luca Romani)

Probably the first use of clinically relevant MEG was in the study of epilepsy. The possibility of studying the relatively strong magnetic signals originating from interictal "spikes" was intriguing, although the major difficulty experimenters faced was that quite often this activity is not localized. It involves a relatively large area in a cerebral lobe, then rapidly spreads to the rest of the brain. Identifying and following this activity with a single-channel system was definitely a challenge, even with the relatively large amplitude of epileptic signals. Nevertheless in 1982, Barth and coworkers[18] initiated a procedure that provided a solution to this problem. The "trick" was to record just the very first epileptic spike that initiates the more complex activity, and average it with similar initial spikes. When averaged data produced an acceptable S/N ratio, the sensor was moved to an adjacent position, with the same process repeated at that location. In this manner, the field distribution over the scalp was obtained, as well as the location of one source in one hemisphere. The authors also could identify a mirror focus in the contralateral hemisphere. In a subsequent paper the same authors were able to observe the spread of activity from one source to another in the same hemisphere.

During this pioneering period, enthusiasm for this new technique encouraged scientists to initiate a series of periodic meetings. The inaugural International Conference on Biomagnetism took place in Boston in 1976 and was repeated biennially around the world in subsequent years in such places as Berlin, Rome and Vancouver, and it continues to the present time, with an average of about 700 attendees. Last, but not least, a NATO Advanced Study Institute on Biomagnetism was organized by Williamson and Romani in Grottaferrata (Italy) in 1982, the proceedings of which have been used to

[14] G.L. Romani et al., *Rev. Sci. Instrum.* 53 (1982) 1815
[15] Maclin et al., *Il Nuovo Cimento D*, 2 (1983) 410
[16] YC Okada et al., *Exp. Brain Res.*, 56 (1984) 197
[17] R Hari et al., Acta *Neurologica Scandinavica*, 68 (1983) 207
[18] D.S. Barth et al., *Science* 218 (1982) 891

help train numerous students in biomagnetism in succeeding years. Additionally, the International Conference on Functional Source Imaging was held in 1986 at Villa Gualino, Torino (Italy). It attracted leading experts in the field and marked the first attempt to establish standards for MEG source identification.

10.2.4 A Step Ahead: Technological Developments

Modeling

As shown in a previous section, the magnetic field pattern generated by a current dipole over the scalp features a maximum and a minimum, with the distance separating them proportional to the current dipole depth. Conversely, in order to localize a small area of activated cortex, it is necessary to map the magnetic field over a surface including both the maximum and minimum. Therefore, the deeper the activation, the larger is the area that should be mapped. This is a simple example of the principle that, in order to increase the information content, it is necessary not only to collect more data points, but also to enlarge the area to be mapped. As one maps over a larger area, the assumption of a plane boundary for the conductive medium, which may be valid locally, is no longer valid globally, so one must resort to volume conductor models bounded in space. In particular, a spherical model is a better approximation of the head as a volume conductor. More generally, for the practical application of MEG, there is a need for more flexible models for data interpretation that, on the one hand, remove simplifying assumptions that may be unjustified in practice, and on the other hand, represent the biological medium more realistically. For example, the question arises as to whether the skull, as a source of inhomogeneous conductivity, has a strong influence on the magnitude and direction of the magnetic field at each point. Another example is the difference between the actual head shape and a sphere: Is a spherical conductor model accurate if the activity is in the temporal area, which is an area that clearly deviates from a spherical shape? Does one need a more realistic conductor model? In that case, if many sensors are located on a rigid surface (in the cryostat), it is not possible to place them all orthogonal to the scalp, so that the formula for the magnetic field of only primary currents is no longer accurate, and a more general formula including the magnetic field of volume currents is needed. Finally, it is possible that complex patterns of a magnetic field may be measured, likely due to the simultaneous activation of multiple areas. In some cases the resulting magnetic field map may not be interpreted in terms of a single ECD, and more complex current patterns must be envisaged, such as multiple ECDs, or higher-order terms of the multipole expansion of the current. We now present a few examples of volume conductor and neural activation models. A simple way to describe the inhomogeneity of the head as a volume conductor is to segment it into three compartments: brain, skull, and scalp. Although gross, this subdivision allows one to account for the presence of the skull which can influence volume currents due to its low conductivity with respect to the other tissues. A general equation for the magnetic field of currents inside a piecewise homogeneous conductor was given by Geselowitz[19]:

$$\mathbf{B}(\mathbf{r}) = \mathbf{B}_0(\mathbf{r}) + \frac{\mu_0}{4\pi}\sum_{j=0}^{k}(\sigma_{j+1}-\sigma_j)\int_{S_j}\frac{\Phi\mathbf{n}_j'\times(\mathbf{r}-\mathbf{r}')}{|\mathbf{r}-\mathbf{r}'|^3}da'. \tag{10.5}$$

In this relation, the homogeneous compartments are assumed to be nested, with the impressed currents flowing into the innermost compartment only. The field is given at a point $\mathbf{x}$ outside the outermost compartment. The total magnetic field $\mathbf{B}(\mathbf{r})$ at point $\mathbf{r}$ is the sum of the magnetic field of the impressed currents $\mathbf{B}_0(\mathbf{r})$. For the case of an ECD, this is equal to equation 10.3 and to the magnetic field due to volume currents. The latter term is expressed as a sum of surface integrals, one over each of the interfaces S_j between adjacent homogeneous compartments (where $\mathbf{n}_j'$ is the unit vector lo-

[19] D.B. Geselowitz, *IEEE Trans. Magn.* 6(1970) 346

cally orthogonal to the surface and pointing outward). The sum is obtained from the innermost to the outermost surface. A comparison of the integrand with Equation 10.1 shows that each integral represents the total magnetic field of an array of current dipoles, orthogonal to the surface, of intensity $\Delta\sigma\Phi$ per unit area, where $\Delta\sigma$ is the conductivity difference across the surface, and Φ is the electric potential over the surface. Therefore, the calculation of the magnetic field of volume currents requires knowledge of the electric potential over the interfaces between compartments with different conductivity. The electric potential may be obtained by solving an integral equation[20]. Note that the current dipole distribution over the interfaces is fictitious; it is merely a practical means for calculation. The only real currents are the impressed and volume currents. Although seemingly complex, Equation 10.5 leads to a great simplification: First, it replaces a volume integral (the integral of the Biot-Savart law over the entire conductor), with a sum of surface integrals; second, it replaces the problem of solving for the volume current distribution inside the conductor with the problem of solving for the electric potential above the interfaces.

If the piecewise homogeneous conductor is spherical, the contribution of the volume currents is a vector tangential to the sphere, as may be understood by noting that the projection of the numerator of the integrand onto a radial vector $\mathbf{e}_r$ at point $\mathbf{r}$, $\Phi\mathbf{n}_j'\times(\mathbf{r}-\mathbf{r}')\bullet\mathbf{e}_r$ vanishes because these three vectors lie in a plane (with the origin taken as the center of the sphere). The radial component of the magnetic field depends only on the impressed currents. In the spherical case, it is possible to circumvent the calculation of the electric potential, and to obtain the magnetic field of a current dipole in closed form[21] by deriving it from the scalar magnetic potential, which in turn may be calculated by integrating the radial component of the field from a sphere's surface to infinity. Since the latter does not depend on conductivity, neither does the total field depend on conductivity. It is remarkable that, in this case, the difference in conductivity between compartments does affect the volume current distribution, but not the magnetic field outside the sphere

$$\mathbf{B}(\mathbf{r}) = \frac{\mu_0}{4\pi F^2}(F\mathbf{Q}\times\mathbf{r}_0 - \mathbf{Q}\times\mathbf{r}_0\bullet\mathbf{r}\,\mathrm{grad}\,\mathrm{F}) \tag{10.6}$$

where F depends only on $\mathbf{r}$ and $\mathbf{r}_0$ (not on $\mathbf{Q}$).

Equation 10.6 gives the total magnetic field (i.e., the sum of impressed and volume current contributions) at point $\mathbf{r}$, generated outside the sphere by a current dipole at point $\mathbf{r}_0$ with current dipole moment $\mathbf{Q}$. Note that, as already observed for a plane conductor, a radially-oriented current dipole does not generate a field outside the sphere, since in that case $\mathbf{Q}\times\mathbf{r}_0$ vanishes. Although this feature is true for a spherical conductor, it gives a hint of what can happen in a real head: Currents that are oriented "radially" will generate a very low field, and will be undetectable by MEG due to noise. Conversely, MEG will be most sensitive to currents flowing orthogonal to the radial direction, i.e., tangentially. As a consequence, since most PSP currents flow orthogonal to the cortex surface in the apical dendrites of neurons, MEG will be most sensitive to activations located inside the cortical fissures. On one hand, this limits the sensitivity of MEG because part of the activation is silent; on the other hand, this very limit, by reducing the detectable area of cortical activation, leads to more focused magnetic field patterns and makes the currents easier to localize. Stated informally, with MEG "we see a little less, but what we do see, we see more clearly than with EEG". It should be noted that the reduced sensitivity of MEG has not yet hindered its development, probably because the largest part of the cortex is located in fissures that include the primary sensory regions.

In summary, the spherical volume conductor model is a bounded conductor model that provides an analytical relation for the total magnetic field due to impressed and volume currents. As a consequence, the exact geometry (position and orientation) of the sensors may be incorporated into the model. Despite these advantages, the spherical model may still be inaccurate in some cases. Indeed, the human head does not have a spherical shape, and while a sphere will approximate the

[20] D.B. Geselowitz, *Biophys.* J. 7 (1967) 1

[21] J. Sarvas, *Phys. Med. Biol.* 32 (1987) 11

head surface locally, it will fail globally. Since the deviation from the real head shape may be a source of localization errors, researchers have chosen more realistic models based on numerical representations of an individual subject head.

Geselowitz's Equation 10.5 becomes quite practical for the implementation of realistic head models. In such models the surface integrals must be evaluated on numerically-represented surfaces, and are thus discretized. This is a particular implementation of a more general method called the boundary element method (BEM). From an MRI of the subject undergoing MEG, scalp, skull and brain compartments are segmented based on voxel gray values, and their interfaces reconstructed numerically, then tessellated with a large number of small plane triangular panels. Each triangle vertex is called a node and lies on one of the interfaces; its coordinates are obtained from MRI. Tessellated models of the head typically include several thousand panels, and field computations are costly. The above mentioned integral equation for the electric potential over the interfaces is also discretized into a linear system of equations that yields the electric potential either at the centroid of each panel of the tessellation, or at each node, depending on the particular implementation. The advantage of using nodes over triangles is that on each surface, the former are about half as many as the latter, thereby reducing the matrix size. At each triangle centroid, or at each node, a current dipole of appropriate direction and intensity is placed to represent the fictitious current density orthogonal to the interface. For example, for the case of the centroid-based implementation, the current dipole is orthogonal to the panel, with intensity $A\Delta\sigma\Phi$, where A is the panel area, $\Delta\sigma$ is the conductivity difference across the interface, and Φ is the potential at the centroid. An estimate of the tissue conductivity values also is required. Conductivity values are usually taken from the literature, and are based on post mortem measured values. In this respect, in vivo measurements of conductivity are of great value for improved accuracy. The scalp and brain have similar conductivities, while the skull has a conductivity about one hundred times smaller. Finally, the total magnetic field may be calculated from a discretized version of Equation 10.5[22]. An important issue is the accuracy of the calculation with the BEM. Due to the low conductivity of the skull, the potential values on the two outer surfaces (air-scalp and scalp-skull interfaces) are much lower than the potential on the inner one (brain-skull interface). In the linear system for the electric potential, the potential at one point depends on the potential at all other points from all surfaces. Therefore, inaccuracies in the potential on the brain-skull interface propagate to the potential on the lower-valued surfaces where they are larger in relative value, leading to poor accuracy. To improve the accuracy, one possibility is to increase the number of panels, thus increasing computational cost. Another possibility is to find the solution by a two-step method: First the potential on the brain-skull interface is approximated assuming the skull conductivity is equal to zero (with this assumption the potential on the two outer interfaces is zero), then a correction term is found using the actual skull conductivity and added to the approximate solution[23]. One finds that the correction is small and that the approximate solution with zero skull conductivity is already a good one. For this reason, the model often used in MEG data analysis is a single-compartment homogeneous model, where the boundary is the brain surface. This represents an excellent compromise between numerical accuracy and ease of computation.

In summary, with relatively simple analytical or numerical calculations, it is possible to take into account the gross inhomogeneities of the head as a volume conductor, as well as the complex shape of the head. An important feature of the model is the position and orientation of the magnetic field sensors. These must be recorded together with magnetic field data during the recording session. This is a distinctive feature of MEG — and also of EEG — compared to other brain imaging techniques. The most popular models for MEG data analysis are the homogeneous sphere, and the realistic, single compartment, head model.

To interpret the measured magnetic field data in terms of underlying cortical activity and its

[22] Barnard et al., *Biophys.* J. 7 (1967) 463

[23] M.S. Hämäläinen, J. Sarvas, *IEEE Trans. Biomed.* Eng. 36 (1989) 165

source, the data are usually fitted to the selected model. In addition to a model of the volume conductor (and sensors), a model of the source must be adopted. As described earlier, the basic source model is the ECD, but this may be too specific. For example, if two brain areas are active simultaneously or close to it, the magnetic field pattern will be, by the principle of superposition, the sum of two dipolar patterns. In such a case, a source model consisting of two ECDs would be more appropriate. A multiple ECD model is a useful generalization of the ECD model, with more ECDs used as more areas are activated. However, there are 6 parameters for each ECD: 3 for the position and 3 for the moment (or 5 if the spherical model is used); so that the number of ECDs that can be fitted in a single time sample in the case of 100 noisy data channels is limited. It is usually assumed that the ECD locations remain fixed during the time period of activation, which may last a few tens of milliseconds, while their moments are allowed to vary at each time data point. This reduces the number of position parameters to be estimated, thus increasing the robustness of the fit. Another widely-used source model consists of an array of a large number of fixed dipoles, usually covering the entire cortical surface. In this case the parameters to be estimated are only the ECD moments, so that the relationship between source and field is linear. The problem of source reconstruction is then a problem of linear estimation of an underdetermined system. Such a problem requires the application of a regularization procedure that introduces constraints on the possible solutions[24]. Typical constraints are, for example, the need for the current distribution to have some degree of smoothness[25], or that some dipoles have a higher probability of being activated[26]. Other types of constraints may incorporate information from other imaging techniques such as, for example, fMRI.

Instrumentation

The very first MEG instruments were single-channel ones, usually operated in an open environment using cryostats equipped with local RF shields. The gradiometric detection coils were coupled to RF SQUIDs. A picture of a typical single channel system during set-up and in the measurement position is shown in Figure 10.7. Since mapping of the magnetic field over the entire scalp with

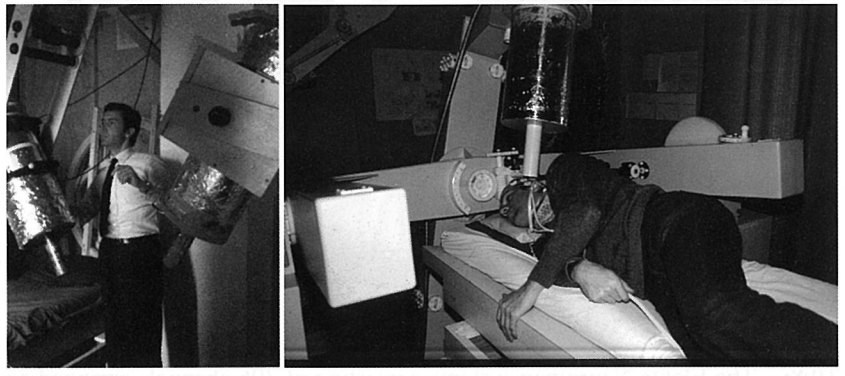

FIGURE 10.7: Left: Gian-Luca Romani setting up two rf-SQUID single-channel MEG systems. Right: Measurements being made by placing the sensor in different positions during repeated auditory stimulation.

[24] A.N. Tikhonov, V.Y. Arsenin, *Solution of Ill-Posed Problems* (1977), Washington, DC: Winston

[25] R.D. Pascual-Marqui et al., *Int. J. Psychophysiol.* 18 (1995) 49

[26] A.A. Iaonnides et al., *Inverse Probl.* 6 (1990) 523

dense sampling is needed to estimate the cerebral sources, usually the tip of the cryostat was placed at each of the sampling points of a regular grid where the evoked magnetic field was recorded. The stimulation sequence was repeated for every sample point; thus it took several hours to complete a set of measurements. Additionally, the recording conditions, such as the subject's attention and environmental noise, might change during measurement. Due to these instrumental limits, MEG in its early stages did not attract the interest of the clinical and neuropsychological communities. Fortunately, advances in SQUID design and fabrication technology produced DC SQUIDs with uniform properties and improved sensitivity ($\sim 20 \times 10^{-15}$ THz$^{-1/2}$), leading in the early 1980s to the first multiple sensor systems with on the order of ten channels. These early multi-channel systems covered part of the scalp so that either single-shot measurements were possible when focal sources were under study, or a reduced number of repositionings were necessary for more extended sampling. At this stage the first commercial systems (i.e., the twin 7-channel systems by BTi) were produced together with self-made systems, each representing a step forward in the development of whole-head systems. Even though these first multi-channel units featured only a small number of channels, they required unique cryostat design, read-out electronics and data acquisition systems. The sensing array, made of wire-wound gradiometers coupled to DC SQUIDs, was arranged on a curved surface, thus requiring larger cryostats with small curved bottoms. Suitable FLL schemes were initiated to reduce crosstalk among channels, for example, coupling of the feedback coil to the gradiometer instead of to the SQUID loop in order to null the supercurrent in the detection coil, or using separate shielded read-out electronics based on flux modulation. The parameters of each SQUID were manually set, and the output stored via the first multichannel ADC boards interfaced with a personal computer.

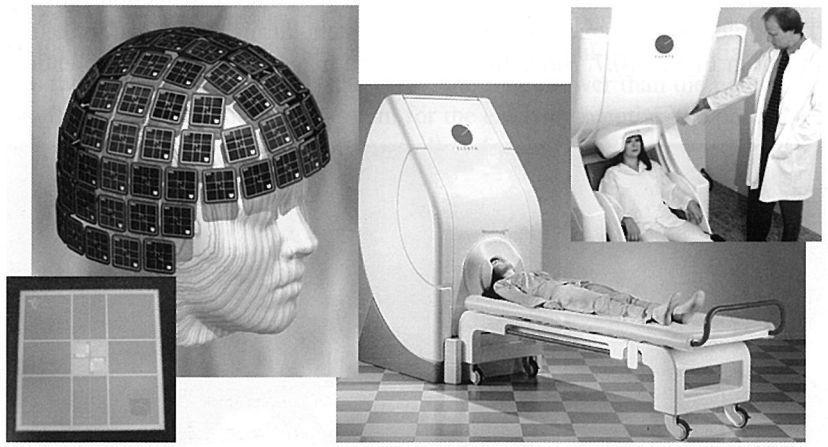

FIGURE 10.8: The Elekta Neuromag systems consisting of 306 channels arranged on 102 sampling positions on a helmet surface. Each measurement module consists of two orthogonal planar gradiometers and one co-planar magnetometer all integrated onto a single chip.

Medium-scale systems were implemented in the early 1990s, comprising about 20 to 40 channels, such as the 28-channel hybrid system in Rome, the 37-channel "Magnes" from BTi, and the 24-channel system in Helsinki. In each, the measurement surface was enlarged yielding a larger number of protocols for which single-shot measurements were possible. Additionally, these larger systems were placed in medium-quality shielded rooms that were made of one to two layers of high magnetic permeability materials and one layer of aluminum. At this stage, the number of MEG systems in the

world increased thanks to their more stable performance. The first whole-helmet MEG systems, the Neuromag 122 and the 64-channel CTF system, entered the market. They represented the next step toward the large-scale systems operating today, one example of which is shown in Figure 10.8. With these systems featuring a few hundred channels, a single-shot measurement of the brain's magnetic field over the entire scalp is possible.

From the 1990s until now, advances in thin-film fabrication led to magnetometers and planar gradiometers integrated on the same chip as the SQUID, suitable to be densely packed over the measurement surface. Additionally, alternate read-out schemes better suited to a large number of channels, e.g., direct read-out with applied positive feedback and voltage bias with noise cancellation, were adopted in place of the standard flux modulation of the FLL. These schemes are simpler, with a smaller number of wires per channel fed through the cryostat and with reduced crosstalk among channels. The read-out electronics is set remotely by a digital interface, integrated in a user-friendly acquisition system. The use of whole-head systems required new cryostat designs to host the extensive number of sensors at the bottom, and as near as possible to the room-temperature surface. In some cryostats the helmet is placed with its axis at 45° to the vessel axis, allowing for measurement in either the supine or seated position. With these systems installed in high-quality shielded rooms, clinical studies are feasible due to advanced engineering and the resultant ease of operation, both from the point of view of the clinical investigator, and from that of the patient.

10.2.5 Brain Mapping and Clinical Studies

The development of multichannel MEG devices improved the quality of MEG studies and allowed scientists to investigate cross-modal sensory interaction or cognitive brain functions such as language or attention. An example of interaction of auditory and visual sensations is described by Sams and coworkers[27]. In that paper the magnetic field generated by the activity of the auditory sensory cortex was recorded while the subject was hearing a Finnish syllable "pa" repeated every second. At the same time the subject was looking at a videotaped face articulating the same syllable. However, in 16% of the cases the face articulated a different syllable: "ka". This discordance caused a clear difference in the measured field about 200 ms after the sound, thus supporting the idea that cross-modal effects can be observed even in primary areas.

One of the features of the human brain is its plasticity, i.e., the ability to change its functional configuration not only during development and maturation, but also whenever deviations from homeostasis are transiently or permanently imposed. This long-term plasticity involves changes in the synaptic configuration of large brain segments. This type of plasticity occurs over weeks or months during which the brain's wiring is profoundly reorganized. However, there must be different and more rapid plasticity. Short-term plasticity takes minutes to become effective and involves a type of software alteration of the brain's functional configuration. The first demonstrations of this form of plasticity using MEG were provided by Rossini and coworkers[28]. In this work the authors induced an anesthetic block of the sensory information from all but one finger of the right hand. Somatosensory-evoked fields (SEFs) were recorded during electrical stimulation of the unanesthetized finger, this finger being the 1st, 3rd or 5th finger. MEG data showed that only 30 minutes after the anesthetic block, the primary cortical area activated by stimulating the unanesthetized finger enlarged to include nearby areas usually responding to the anesthetized fingers (Figure 10.9). A similar study, but involving a long-term plasticity effect, was performed by Elbert and colleagues[29]. In it the somatosensory cortical organization of the hand was measured in nine musicians playing string instruments. Since string players use their left hand differently from the right one, the dif-

[27] M. Sams et al., *Neurosci. Lett.* 127 (1991) 141
[28] P.M. Rossini et al., *Brain Res.* 642 (1994) 169
[29] T. Elbert et al., *Science* 270 (1995) 305

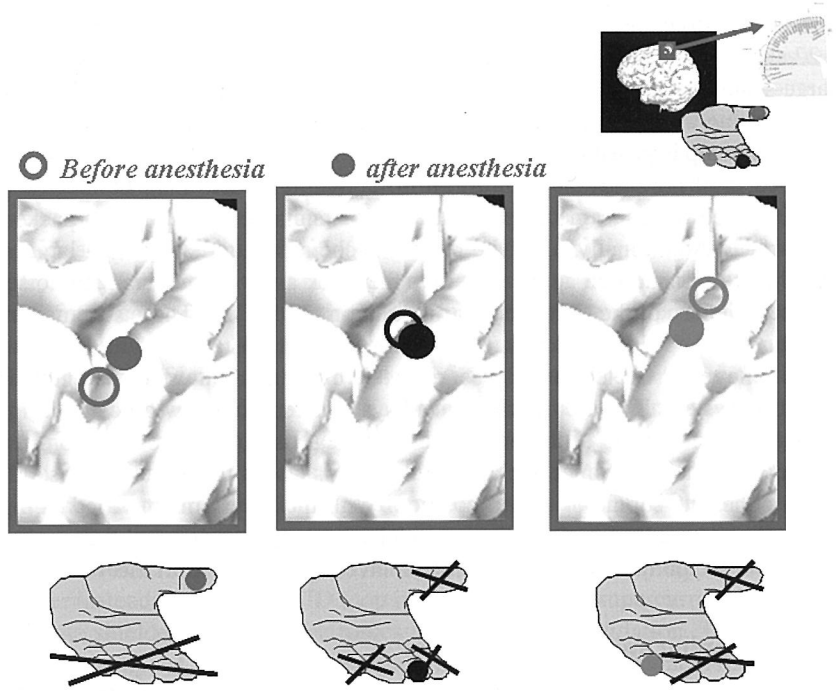

FIGURE 10.9: Top right inset: "homuncular" distribution of the hand representation in the primary sensory cortex is observed by MEG. Bottom: transient rearrangements of finger representation in primary somatosensory cortex induced by an anesthetic block of the sensory inflow from adjacent fingers: the topography of the source responsible for the cortical responses from the unanesthetized finger changed significantly, invading the region devoted to the cortical representation of the other anesthetized fingers.

ference should be found in the brain's somatosensory areas. In fact, MEG measurements showed that the cortical representation of the digits of the left hand was larger than that in a control group, while no differences were observed for the representations of the right-hand digits. Moreover, the amount of cortical reorganization in the representation of the fingering digits was correlated with the age at which the person had begun to play. During the second half of the 1990s the development of whole-head MEG systems gave new vitality to the use of MEG in neuroscience, as well as in clinical studies. The spread of MEG beyond research laboratories matches the marketing of whole-head systems featuring over 100 SQUID sensors. The reason for this is simple: the human brain is very complex, and to understand its organization, one must detect the spatial distribution of the magnetic field associated with its operation as accurately as possible. Moreover, many diseases originate or result from incorrect interplay of different brain areas. Simultaneous detection of the activity of different neuronal pools is therefore necessary to highlight changes in neuronal processing or conduction that may result in dyslexia or more severe forms of cognitive impairment.

Basic Neuroscience

The human brain is comprised of two distinct hemispheres. Each hemisphere mainly collects sensory information from the contralateral side of the body, but there are important exceptions for relevant stimuli, such as those involving pain. Whole-head MEG systems have proven to be very ef-

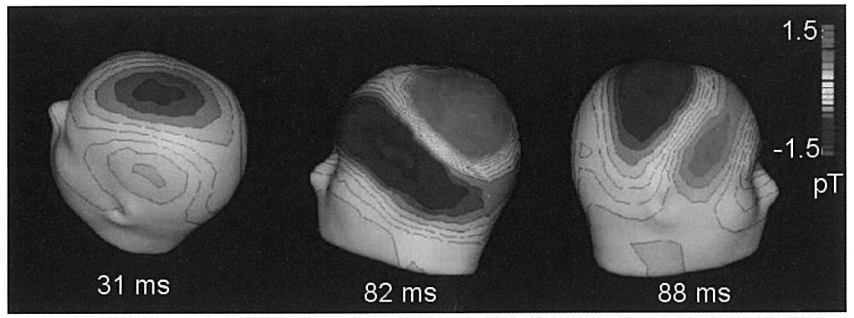

FIGURE 10.10: Isofield contour maps of the magnetic response recorded by magnetometers to galvanic right thumb stimulation at 31 ms, 82 ms and 88 ms after the stimulus. Positive values indicate the magnetic field emerging from the head. The dipolar field distribution suggests the presence of a cortical source in the contralateral primary somatosensory area (left), contralateral (middle) and ipsilateral (right) secondary somatosensory area with different latencies.

fective in detecting cortical activation due to somatosensory stimulation, and most importantly, they serve to quantify the possible difference in latency between the response of the two hemispheres. An example of this ability is provided in one of the simplest MEG protocols: the detection of the magnetic field generated by brain activity after electric stimulation of the thumb. When looking at the brain's response after stimulation of the thumb of the right hand, the following observations are made (Figure 10.10). Complete coverage of the head enables detection of all three major neuronal pools synchronously activated by the stimulus and the quantification of the latency difference between the first response of the left hemisphere (contralateral to the stimulus) and the later response occurring in the so-called "second somatosensory area" of both hemispheres, but with the ipsilateral — meaning same side - responding a few milliseconds later, since information must travel farther to reach the target area. The second somatosensory area response changes with different stimulus intensity. If the stimulating current exceeds the pain threshold, the cortical activation is larger and new areas activate synchronously, thus suggesting a different parallel pathway.

Language studies also benefited from the development of whole-head MEG systems. One of the first studies performed using the Neuromag 122-channel system concerns picture naming. During measurement, the subject looks at simple black and white figures and names them overtly (aloud) or covertly (silently). Through MEG, it was possible not only to identify several brain areas involved in the task, but also to establish precise arrival times. During this naming process, the translation from visual to symbolic representation progressed bilaterally from the occipital cortex, where the visual areas are located, to temporal and frontal lobes. In addition to language areas being involved during overt and covert naming, these areas also exhibited a response to simple passive viewing, although more weakly or after a longer delay[30].

Clinical Studies

One of the first clinical studies made possible by whole-head MEG systems concerns dyslexia. Dyslexia is a learning disability that impairs reading ability, yet it cannot be attributed to diminished intellectual capacity. Dyslexia is distinct from reading difficulties resulting from poor or inadequate reading instruction. MEG measurements during visual presentation of words (passive viewing of concrete/abstract words, pseudowords and letter strings) revealed differences between control and

[30] R. Salmelin et al., *Nature* 368 (1994) 463

dyslexic adults 0–200 ms after word presentation in the left inferior temporo-occipital cortex (word form area) followed by differences of 200–400 ms in the left temporal lobe. These results suggest that dyslexia is related more to the timing of signal processing rather than to a difference in sensory performance[31].

Epilepsy is the brain disease where magnetoencephalography proved to be most effective. The main use of MEG in epilepsy studies is the localization of pathological activity in patients with focal epilepsy. The goal of epilepsy surgery is to remove the epileptogenic tissue while sparing healthy brain areas. Knowing the exact position of important brain regions (such as the primary sensorimotor cortex and areas involved in speech production and comprehension) helps to avoid surgically-induced neurological deficits. Because epileptic activity is not stationary, it is important to record activity of both hemispheres simultaneously. One of the first studies performed with a whole-head MEG system on an epileptic patient proved the importance of this technique. In fact, mirror foci in homotopic areas of the hemispheres were detected. The precise time resolution of MEG led to detection of which area was the primary focus and which was the mirror one[32].

Language function may reside in both or one hemisphere in patients with epilepsy. Determination of laterality is important to preserve as much language and memory function as possible during resective surgery. The intracarotid amobarbital (Wada) test has long been used for language and memory localization. It has both merits and shortcomings when compared to newer forms of testing. It is invasive, uncomfortable and carries some risk. MEG may be used as a substitute or supplement to the Wada test to identify the eloquent cortex, i.e., a part of the cortex that controls various senses or actions, for removal of brain tumors or arteriovenous malformations. This was evaluated in a review by Frye and coworkers[33]. The authors concluded that MEG seems well suited for efficiently mapping language in neurologically-intact individuals. Furthermore, MEG-derived activation profiles appear to be reliable and valid indices of neural activity associated with receptive language function. While certain limitations still preclude MEG from completely replacing invasive diagnostic methods in clinical practice, there is little doubt that the information obtained using this technique is an effective adjunct to existing pre-surgical routines. Today magnetoencephalography or magnetic source imaging (MSI) is considered medically necessary for presurgical evaluation in patients with intractable focal epilepsy, in order to identify and localize areas of epileptiform activity when discordance or continuing questions arise from other techniques designed to localize a focus. In line with this view, the American Medical Association has identified three CPT (Current Procedural Terminology) codes:

95965 Magnetoencephalography (MEG), recording and analysis; for spontaneous brain magnetic activity (e.g., epileptic cerebral cortex localization)

95966 Magnetoencephalography (MEG), recording and analysis; for evoked magnetic fields, single modality (e.g., sensory, motor, language, or visual cortex localization)

95967 Magnetoencephalography (MEG), recording and analysis; for evoked magnetic fields, each additional modality (e.g., sensory, motor, language, or visual cortex localization)

10.2.6 Recent Developments and Perspectives

In the past ten years most of the work performed in the field of magnetoencephalography dealt with data analysis. In fact, the toughest issue for MEG is the identification of multiple magnetic field generators from measurements of the resulting field. Among the various algorithms that have been

[31] R. Salmelin et al., *Ann. Neurol.* 40 (1996) 157
[32] R. Hari et al., *Neuroreport* 5 (1993) 45
[33] R. Frye et al., *Physics of Life Rev.* 6 (2009) 1

developed and successfully used to process MEG data, independent component analysis (ICA) is the most successful. The basic idea of the ICA algorithm is the following: different sources, especially if related to external disturbances, are often independent of each other. In MEG data analysis, ICA can isolate disturbances due to heart activity or an eye blink. Moreover, data regularization is required for a linear estimate of the sources of the magnetic field, and this regularization is easier to achieve if the time series of the different channels are separated into statistically independent components.

A different, but successful, approach to identify the activity of a specific brain region is the so-called "beamforming" approach. This method is borrowed from radar technology, where different "beams" are used to build an image. The beamforming approach falls into the category of adaptive spatial filters. Therefore, it is a data-driven method, whereas the more traditional least squares fit is model-driven.

As a result of new multichannel systems and new data analysis techniques, challenges are being met more successfully. Perhaps the biggest challenge is related to brain functional connectivity. Recently, more importance has been given to the idea that the bases of peculiarity of the human brain should not be sought in its size or cell number, but rather in the specificity and abundance with which neurons are connected. The study of maps of functional cerebral connections has become the basis for understanding how the brain works. Recently, the concept of resting state networks (RSNs) has been introduced for investigating functional connectivity in studies that do not imply external stimuli or task execution. RSNs are defined as neuronal pools activated in spatial patterns that are active, even in the absence of a task. RSNs are thought to reflect the efficacy of anatomical connections present between brain areas. It is surmised that their change during development or aging might reveal changes in brain functional organization. RSNs were first observed (using fMRI) as correlated fluctuations of the transit time from brain areas that are known to belong to the same functional network. These correlated fluctuations show that different nodes of a particular network have similar activations even if they are not engaged in a task, suggesting that some form of ongoing communication is constantly present in the network. fMRI signals have poor temporal resolution: the hemodynamic response is slow and delayed with respect to neuronal activity, and acts as a low-pass filter on the neuronal time interval of an activity. The observed RSN correlations have a one-second temporal resolution, which is quite large compared to the time scale of neuronal events. Recently RSN correlations of electric activity have been observed with MEG[34], taking advantage of its superior temporal resolution, its comparatively high spatial resolution, and by applying advanced data analysis methods. MEG patterns of RSN correlations have shown richer variability over different time scales. It was found in particular that correlation in a single RSN across hemispheres, spans much shorter time intervals (about 10 s) than correlation within a single (stationary) hemisphere, suggesting that RSNs are not really resting, but rather are somewhat restless.

In conclusion, MEG has now reached a level of maturity that ranks it as one of the most important neuroimaging technologies. Although less versatile than MRI, and dependent on MRI for anatomical imaging and model construction, it produces direct detection of neural activity with unrivalled temporal resolution. With better spatial resolution than EEG, comparatively low influence of volume conduction in tissues, and complete noninvasiveness, it is a unique tool for large-scale electrophysiological imaging. Recent results in studies of brain connectivity demonstrate its potential for neurological investigation. The recognition that impaired connectivity is a biomarker of many neurological diseases, such as stroke and degenerative diseases, suggests an important future role for MEG in neurological diagnostics.

[34] F. de Pasquale et al., *PNAS* 107 (2010) 6040

10.3 MCG Instrumentation and Applications

Riccardo Fenici, Donatella Brisinda, Anna Rita Sorbo and Angela Venuti

An invitation to write about the history of something is usually an acknowledgment of competence in the field. However, it creates at least two problems. First, you must accept the fact that you have become old enough to be considered part of that history, and that is usually not a good feeling. Second, it is highly likely that someone else has already written that history and in a better form. So it may be difficult to provide information that cannot be found elsewhere.

The concept of magnetocardiography (MCG) was born in 1963, when Baule and McFee[35] recorded the first magnetic heart signals with a huge set of copper coils with millions of windings arranged in a gradiometer configuration. However, systematic MCG recordings became possible only after the invention of the superconducting quantum interference device (SQUID). Indeed, I missed the beginning of this history, as well as the first decade of superconductive magnetocardiography in the early seventies when a few scientists pioneered basic research in MCG. Their work created the basis of cardiac magnetic field interpretation and explored several potential applications of MCG as a method to improve noninvasive diagnosis of cardiac abnormalities. In addition to many excellent papers, there are many reviews covering the history of the first 10 years of MCG[36,37,38], so it would be difficult for me to find something to add here. Instead, being a small part of MCG history starting in the 1980s, I shall focus on the last three decades. However, since Gerhard Stroink[39] has provided an elegant review of the history of magnetocardiography at the International Conference on Biomagnetism 2010, I shall try to integrate his exhaustive work from the point of view of a clinical cardiologist, whose destiny was to became "gray-haired" expending energy in an attempt to bring MCG to the patient's bedside and to use it daily as a diagnostic tool.

10.3.1 A New Boost in the 1980s

The first time I was introduced to the concept of superconductivity was in late November 1979, thus almost ten years after the first high-quality magnetocardiogram had been recorded in David Cohen's magnetically-shielded room (MSR) at MIT using Jim Zimmerman's SQUID. I received a call from Ivo Modena, head of the Istituto di Elettronica dello Stato Solido (IESS) of the Consiglio Nazionale delle Ricerche (CNR) in Rome, who invited me to visit his laboratory and see the first SQUID-based Italian instrumentation for biomagnetic measurements. At that time I was mostly involved in invasive cardiology with special interest in cardiac arrhythmias and advanced clinical electrophysiology (i.e., monophasic action potential recording, cardiac pacing). I had never heard of biomagnetism or magnetocardiography. At IESS I met Gian Luca Romani, a young physicist who had constructed the Italian SQUID. He gave me a quick introduction to the fundamentals of superconductivity. I learned the SQUID was not only a sea creature, but also a superconducting quantum interference device, invented by Jim Zimmerman and capable of detecting the very weak magnetic field (MF) produced by the electrical activity of biological sources. With Zimmerman's SQUID installed in MIT's 5-layer MSR, Cohen had recorded the first (Zimmerman's) MCG, which was as clear as a conventional ECG. The combination of the SQUID and MIT's MSR provided a high signal-to-noise ratio. However, a MSR was expensive and not easy to install everywhere,

[35] G.M. Baule, R. McFee, *Am. Heart*. J. 55 (1963) 95

[36] D. Cohen, *Neurology and Clinical Neurophysiology* 30 (2004)

[37] P. Siltanen, in: *Comprehensive Electrocardiology,* Pergamon Press 2 (1989) 1405

[38] J.P. Wikswo, Society of Photo-Optical Instrumentation Engineers 167 (1979) 181

[39] G. Stroink, BIOMAG 2010, *IFMBE Proceedings* 28 (2010) 1

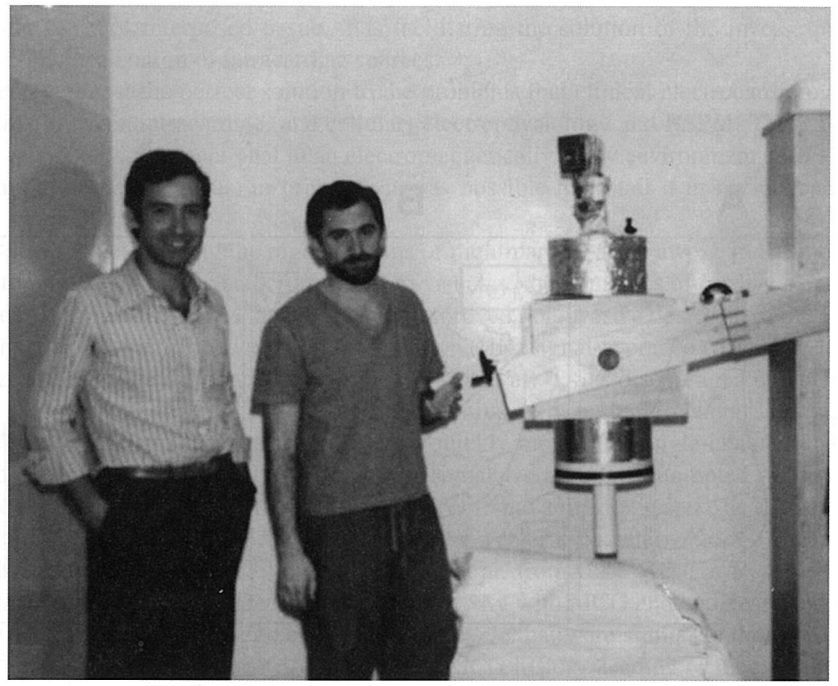

FIGURE 10.11: The original single-channel SQUID-based instrumentation constructed at IESS by Gian Luca Romani (left) and installed, in 1980, by Riccardo Fenici (right) at the Gemelli Hospital of Catholic University, Rome, where the first clinical high-resolution MCG measurements were carried out.

especially in clinical environments. Thus, it was evident that, seeking clinical applications of biomagnetism, a cheaper and simpler solution was needed to damp electromagnetic noise. The first tentative solution to record biomagnetic signals without electromagnetic shielding derived from Zimmerman's invention of the first superconducting gradiometer connected to a SQUID. The unshielded approach offered the potential to involve more scientists in biomagnetism, even those with modest research budgets. This method was used at the Helsinki University of Technology, where MCGs were obtained with a SQUID-based gradiometer in a wooden cottage, as well as below ground at the Helsinki Hospital[40,41] and at Dalhousie University[42], where there was considerable experience and technology available to combine cardiac magnetic recordings with body surface potential mapping (BSPM).

At that time, with only a single channel available, the normal component of the cardiac MF had to be measured sequentially at different locations, typically in a rectangular grid. An alternate approach was developed at Stanford, where the three orthogonal components of cardiac MF (vector magnetocardiography) were measured at a single position over the heart, on the assumption that, as in vector electrocardiography, the 3D motion of the magnetic heart vector represents the overall activity of the heart.

In Rome, Gian Luca Romani had constructed a more sophisticated gradiometer capable of improving the S/N ratio of magnetic signals by accurately balancing the gradient. That solution was

[40] M. Saarinen et al., *Cardiovascular Res*. 8 (1974) 820

[41] M. Saarinen et al., *Ann. Clin. Res*. 10 (1978) 1

[42] G. Stroink et al., *Med. Biol. Eng. Comp*. 23 (1985) 61

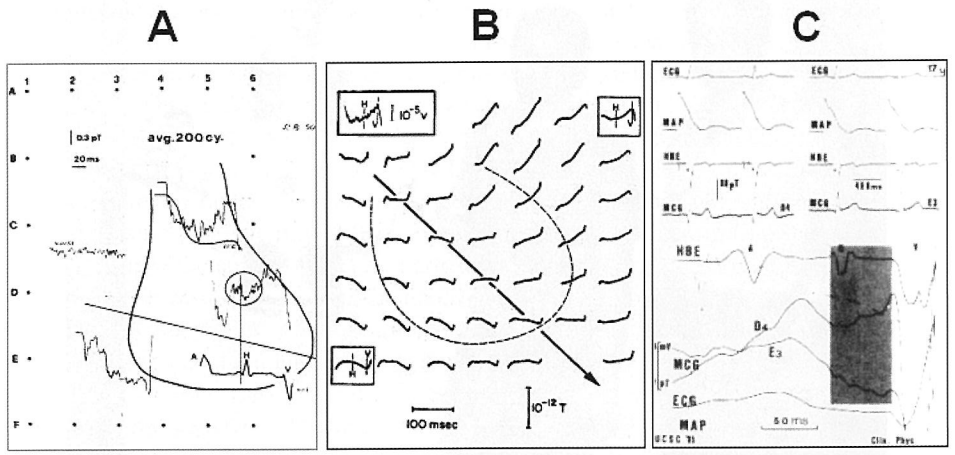

FIGURE 10.12: Three historical high-resolution MCG recordings. (A) The first validation of HR-MCG of His-Purkinje System by comparison with catheter recording of His-Bundle Electrogram in a patient with first degree infra-hisian block [modified from R. Fenici et al., *G. Ital. Cardiol.* 10 (1980) 1366]. (B) First complete mapping of HR-MCG of the P-R segment of a normal subject. The inversion of polarity and asymmetry of the "ramp" pattern from the upper right to the lower left is evident [modified from D.E. Farrell et al., SQID 80: Proc. Of the Second International Conf. on Superconducting Quantum Devices, Berlin 1980 (de Gruyter, NY, 1980) eds: H. D. Hahlböhm + H. Lübbig 273]. (C) First simultaneous recording of MCG and invasive electrophysiological signals with amagnetic catheters [modified from R. Fenici et al., *Med. Biol. Eng. Comp.* 23 (1985) 1475].

very useful in adapting the instrumentation to various noisy environments.

Nevertheless, the appearance of the IESS system (Figure 10.11) was not appealing to a clinical cardiologist! However, that afternoon I was very impressed to see my own cardiac signal, similar to an ECG trace, coming through my shirt and in a noisy physics laboratory. That was my first magnetocardiogram. Ivo and Gian Luca asked me to suggest what could be done with "that thing" in a clinic. As stated earlier, I was unaware that scientists (mostly physicists) elsewhere had followed David Cohen's lead — his pioneering research has been of great value to the field of MCG — and had already explored many potential applications of MCG as an alternative to or as complementary to ECG for noninvasive investigation of cardiac electric activity, nor did I know of the debate on the potential of MCG to provide "unique information" not attainable via ECG. I returned home fascinated by the fact that MCG was a "contactless" technique, thus potentially an easier method to perform cardiac surface mapping without sanding the skin and attaching tens of electrodes. In this way it was theoretically possible to use MCG to map the dynamics of cardiac electrical activity even through the sterile dressing covering the patient during interventional electrophysiological procedures. Another interesting fact I learned from the physicists was that the cardiac MF, directly induced by ionic action currents, reached the sensor unaffected, to a first approximation, by the

varied conductivity of interposed tissue, thus facilitating the solution of the inverse problem for noninvasive 3D localization of intracardiac sources.

This seemed almost the perfect solution to the problems that clinical electrocardiologists had in finding a link between intracardiac (and cellular) electrophysiology and BSPM. The Italian instrumentation was potentially functional in an electromagnetically noisy environment such as a cardiac catheterization laboratory. Thus, in principle it was possible to install it in my hospital on short notice.

I had a "fever attack" during the night (dreams or nightmares?) and I awoke in the morning with proposals to the IESS's physicists to use MCG to visualize the dynamics of cardiac electrophysiology more easily than with BSPM, and to attempt improved noninvasive detection of the His-Bundle electrogram, as it was performed with high-resolution (HR) signal-averaged (SA) ECG, to evaluate noninvasively the infranodal conduction time (H-V interval). I was discouraged about the amount of time it took for MF mapping: rather time-consuming with a single channel and no software available for isofield maps reconstruction, but we quickly moved the single-channel instrument to Gemelli Hospital of the Catholic University. Using signal averaging we attempted the first "clinical" MCG to detect HR signals during the P-R interval. We found a magnetic spike as a function of time correlated with the His-Bundle electrogram recorded via cardiac catheterization[43] (Figure 10.12A). Then we learned that, independently, David Farrell et al. from Case Western Reserve University, had performed a preliminary HR recording of P-R activity with MCG and had described notches in the last 40 ms prior to the QRS segment of the heart cycle that were similar to those recorded with SA-ECG[44]. This was the harbinger of a new era in MCG history, leading to much future research and hot discussions that are still going. In addition to spikes, a "ramp-like" pattern was observed, changing in polarity along the longitudinal diameter of the heart. This was interpreted as the field generated by the His-Purkinje system (HPS)[45] based upon the contemporary findings of Berbari et al. using SA-ECG[46].

10.3.2 The History of High Resolution MCG

At the Third International Conference on Biomagnetism in Berlin in the spring of 1980, Barbanera et al.[47] and Farrell et al.[48] presented the first data on HR-MCG. Farrell et al. showed a complete magnetic mapping of the "ramp-pattern" during the terminal part of the P-R interval (Figure 10.12B) and supported the interpretation of its electrogenesis from HPS activation on the basis of their model of the HPS[49]. We had doubts about the interpretation of the "ramp" as a field generated by the Purkinje system alone because during the terminal part of the P-R interval atrial repolarization, it widely overlaps the activation of the HPS tissue [as demonstrated by simultaneous monophasic action potential recording, (Figure 10.12C)]. However, Tripp's theory was convincing and the "ramp pattern" was accepted as related to HPS activity (Figure 10.13A). I had the opportunity to continue that research also in the Berlin MSR, having been invited to the Physikalisch-Technische Bundesanstalt (PTB) by Sergio Erné — another key person in my personal history of MCG — to work on HR-MCG/ECG (Figure 10.14). At that time the focus was still on HR waveform analysis to give a physiological explanation of the "spikes" and "ramps". In September 1982, at the Fourth Biomagnetism Conference in Rome, theories, models and experimental results were presented[50].

[43] R. Fenici et al., G. *Ital. Cardiol.* 10 (1980) 1366
[44] D.E. Farrell et al., *Pro. Soc. Photo-Opt. Instrum. Eng.* 167 (1978) 173
[45] D.E. Farrel et al., *IEEE Trans. Biomed. Eng.* BME-27 (1980) 345
[46] E.J. Berbari et al., *IEEE Trans. Biomed. Eng.* 26 (1979) 82
[47] S. Barbanera et al., W. de Gruyter & Co, Berlin (1981) 283
[48] D.E. Farrel et al., W. de Gruyter & Co, Berlin (1981) 273
[49] J.H. Tripp, D.E. Farrell, W. de Gruyter & Co, Berlin (1981) 259
[50] J.L. Patrick et al., *Il Nuovo Cimento* 2D 2 (1983) 255

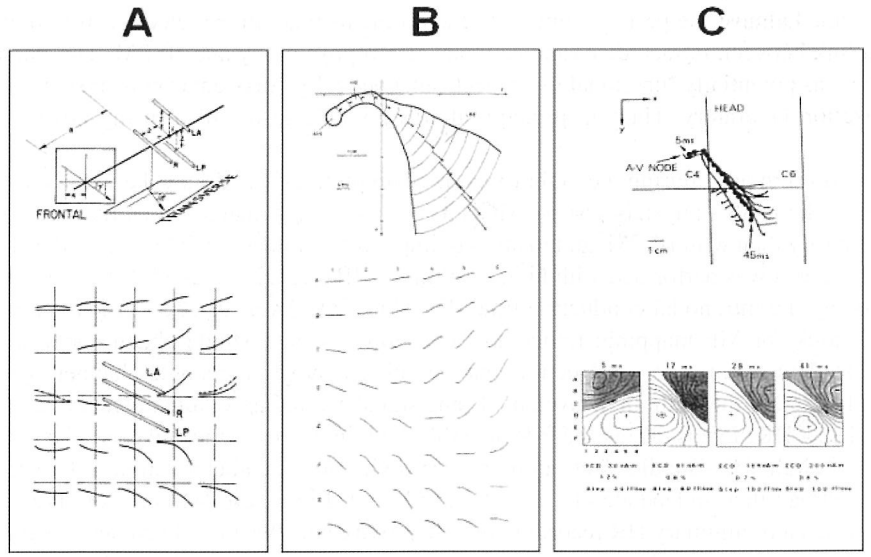

FIGURE 10.13: Mathematical models of the His-Purkinje conduction system. (A) [modified from J.H. Tripp, D.E. Farrell, SQID 80: Proc. Of the Second International Conf. on Superconducting Quantum Devices, Berlin 1980 (de Gruyter, NY, 1980) eds: H. D. Hahlböhm + H. Lübbig 259]; (B) [modified from R. Leoni, G.L. Romani, *Il Nuovo Cimento* D 1 (1982) 737]; (C) [modified from Y. Uchikawa, S.N. Erné, I.S.I. *Word Scientific* (1989) 13].

Mark Leifer from Stanford came with an experimental demonstration that the "ramp" pattern was due to atrial repolarization[51]. Roberto Leoni, at IESS, had developed another model of the HPS[52] that generated both "spikes" and "ramps", in good agreement with experimental findings (Figure 10.13B). We reported the first "manual" reconstruction of "isofield maps" of the P-R interval and calculated 3D localization of equivalent dipoles generated by the HPS[53]. I was sure we needed to adopt that type of analysis to improve the diagnostic potential of magnetic cardiac mapping. After days of discussion a final consensus was reached that additional systematic research was needed to clearly identify and separate the contribution to the MF distribution of the P-R interval arising from the atrial and the HPS fibers.

More advanced and realistic mathematical modeling[54,55,56,57,58] as well as basic experimental

[51] M. Leifer et al., *Il Nuovo Cimento* 2D 2 (1983) 266
[52] R. Leoni, G.L. Romani, *Il Nuovo Cimento* D 1 (1982) 737
[53] R. Fenici et al., *Il Nuovo Cimento* 2D 2 (1983) 280
[54] J. Nenonen, T. Katila, *Int. J. of Cardiovascular Imaging* 7 (1991) 177
[55] A. van Oesterom, G.J. Huiskamp, *Int. J. of Cardiovascular Imaging* 7 (1991) 169
[56] R.S. Gonnelli, M. Agnello, Phys. Med. Biol. 32 (1987) 133
[57] Y. Uchikawa, S.N. Erné, in: *Biomagnetism* 87 Tokyo Denki University Press (1987) 322
[58] M. De Melis, Y. Uchikawa, BIOMAG2010, *IFMBE Proceedings* 28 (2010) 420

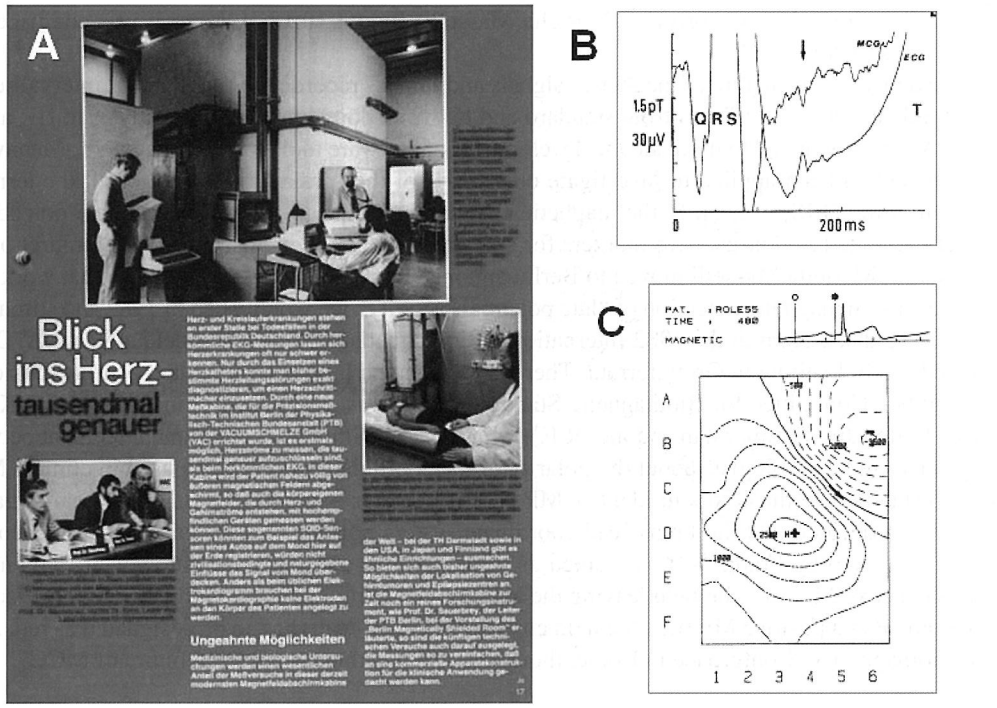

FIGURE 10.14: High resolution MCG at the Physikalisch Technische Bundesanstalt, in 1981. (A) The Berlin MSR with Sergio Erné (center), Z. Trontelj (left) and Hans Lehmann (right). (B) Simultaneous HR-MCG and ECG recordings of the P-R interval in the MSR. Both "spikes" and "ramps" were appreciable [modified from S. Erné et al., *Journal of Electrocardiology*. 16 (1983) 355]. (C) First automatic isofield map reconstruction and ECD localization at an instant of the P-R interval.

research[59] were required to understand the fundamentals of biomagnetic localization of cardiac sources. Although there were hot tempers and sleepless nights in Berlin, Erné agreed that simple HR waveform analysis was a limitation and accepted the task of writing software to image quickly and automatically HR isomagnetic maps of the P-R interval and to localize three-dimensionally the corresponding cardiac sources using the equivalent current dipole (ECD) model. When we finally were able to examine the dynamics of MF maps along the P-R interval, it became evident that the "ramp-like" MF pattern was mostly due to atrial repolarization. In fact, that MF was opposite in polarity to the one generated during atrial depolarization (the P wave). I then convinced Erné to write the software to subtract the atrial repolarization field component from the P-R segment. We found that after this subtraction, it was possible to identify a weaker (remaining) MF generated by sources (localized with the ECD inverse solution) that moved from the A-V junction downward along the interventricular septum[60]. That MF was consistent with the activation of the HPS. The correctness of this interpretation was validated by comparison with the MF pattern generated by a more realistic mathematical model of the HPS, developed at the PTB by Yoshinori Uchikawa[61,62]

[59] J.P. Wikswo et al., *Il Nuovo Cimento* 2D 2 (1983) 368
[60] S.N. Erné et al., in: *Biomagnetism Application and Theory*. Pergamon Press NY (1985) 132
[61] S.N. Erné et al., in: *Biomagnetism: Application and Theory*. Pergamon Press NY (1985) 123
[62] Y. Uchikawa, S.N. Erné, I.S.I. *World Scientific* (1989) 13

in collaboration with my coworker Mariella Masselli (Figure 10.13C). Later it was confirmed by other investigators[63,64,65,66].

The debate on the nature of magnetic "signals and ramps" recorded during the P-R interval served to stimulate a change of focus from standard and HR time-domain waveform analysis to HR analysis of MF mapping and to motivate the development of software tools for MF imaging[67]. Meanwhile HR MCG had been applied to investigate other parts of the cardiac cycle, first of all the terminal portion of the QRS, to identify the magnetic counterpart of the so-called "electric late-potentials", widely accepted as non-invasive markers for arrhythmogenic risk in post-myocardial infarction patients[68,69]. Mariella Masselli moved to Berlin and made a significant contribution to that work. The first results on magnetic detection of "late potentials activity" were published in 1982 and stimulated interesting discussions at the 1982 International Biomagnetism Conference, held after a NATO Advanced Study Institute in Grottaferrata. There, accompanied by much guitar and ocarina music, the first ad hoc Committee for Biomagnetic Standardization was established. It included Toivo Katila, Mark Leifer, Jim Zimmerman and me (R.F.), with the very difficult task "to find agreement between physicists and cardiologists about the polarity of the coordinate system to be used in clinical MCG and to standardize the colors to identify MF polarity". After hours of discussion in a cafeteria, the committee decided that the Frank lead coordinate system polarity—a convention for ECG coordinates suggested by Frank[70]—be accepted as a standard for cardiomagnetism as well. This means that a negative MF (i.e., the field leaving the anterior chest wall) had to be indicated by blue isofield lines, and that a positive MF (i.e., the field entering the chest wall) had to be designated as red. After the Biomagnetism Conference in Rome, there was much enthusiasm for the future of MCG!

10.3.3 From Magnetic Field Mapping to 3D Cardiac Source Localization

As stated earlier, one of the most appealing aspects of MCG was that it could, at least in theory, provide accurate 3D localization of intracardiac sources. This meant for a cardiologist that it could be used to localize arrhythmogenic substrates noninvasively. This was particularly important at a time when experience with antiarrhythmic surgery had shown that the outcome of antiarrhythmic interventions depended very much on preoperative knowledge about the localization and stability of the arrhythmogenic substrate to treat. It is obviously more important now, with catheter ablation proposed as the first line of therapy for several forms of arrhythmias. Although single-channel mapping was quite time-consuming, we thought that it was worth investigating. After successful localization of the His-Bundle activity using ECD[71] analysis, and validation by comparison with invasive recording of the His bundle electrogram[72], we attempted the first noninvasive localization of accessory pathways in patients with the Wolff-Parkinson-White (WPW) syndrome and paroxysmal tachycardias with MCG[73]. Also the localization of accessory pathways was validated with catheter recording of the Kent Bundle's electrogram, invasive cardiac mapping and pacing[74]. That work created the basis for future application of MCG for pre-interventional localization of arrhythmogenic substrates susceptible to interventional ablation[75,76]. Other authors reproduced this type of measurement, validating the accuracy of MCG by comparison with the results of invasive electrophysiological procedures or surgery[77,78,79].

Source localization was a promising application, but a major problem in the 1980s was the lack of software adequate to visualize MF maps and localization data quickly and directly on the computer screen. Post-processing of MCG data was terribly slow, time consuming and definitely not adequate for "clinical use". Unfortunately, at least in Italy, the growing success of neuromagnetism had absorbed the major part of manpower and research funding. Thus, while in other labs physicists had difficulty finding cardiologists interested in MCG, a cardiologist (me) who seriously believed in MCG and wished to bring it to a patient's bedside was unable to find physicists interested in developing software appropriate for clinical work. Luckily, in 1987 I was invited by Hannes Novak to give a lecture on MCG in Jena. There I met a young physicist, Martin Burghoff. I was surprised when he showed me that he was able to visualize isofield maps on the screen of a "homemade"

63 C. MacAulay et al., *Med. Biol. Eng. and Com.* 23 (1985) 1479
64 S. Yamada et al., *Circ.* J. 67 (2003) 622
65 B.J. Ten Voorde et al., *Med. Biol. Eng. and Com.* 26 (1988) 130
66 H.E. Lorenzana et al., *Biomagnetism: Applications and Theory*. Pergamon Press NY (1984)
67 S.N. Erné et al., *Il Nuovo Cimento* 2D 2 (1983) 291
68 S.N. Erné et al., *Jap. Heart* J. 23 (1982) 703
69 S.N. Erné et al., *Il Nuovo Cimento* 2D 2 (1983) 340
70 E. Frank, *Circulation* 13 (1956) 737
71 R. Fenici et al., *Il Nuovo Cimento* 2D 2 (1983) 280
72 R. Fenici et al., *Med. Biol. Eng. Comp.* 23 (1985) 1483
73 R. Fenici et al., *Med. Biol. Eng. Comp.* 23 (1985) 1475
74 R. Fenici et al., *New Trends in Arrhythmias* 3 (1985) 455
75 R. Fenici et al., *J. Interv. Cardiol.* 8 (1995) 825
76 R. Fenici et al., I.S.I. *World Scientific* (1989) 102
77 J. Nenonen et al., *Eur. Heart J.* 14 (1993) 168
78 M. Makijarvi et al., *Eur. Heart J.* 14 (1993) 46
79 M. Nomura, *Clin. Cardiol.* 17 (1994) 239

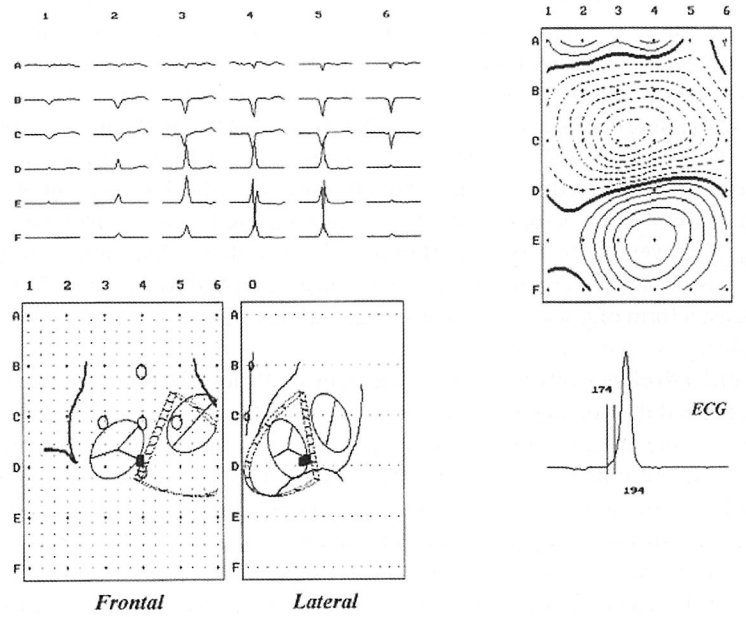

FIGURE 10.15: Typical output of the software written by Martin Burghoff in 1989, providing MF distribution pattern and 3D localization of a right paraseptal accessory pathway, in a patient with WPW syndrome. All kinds of elaboration were analyzable in an interactive and dynamic way directly on the PC screen. The heart silhouette, interventricular septum and atrioventricular plane drawings were derived from fluoroscopy and ultrasound imaging of the individual patient. At that time it was a significant step forward to speed-up clinical evaluation of MCG data.

PC-like computer. I suggested that he come to Rome. It took us almost two years to get all necessary permissions, but in the end Martin arrived in Rome on the last week of September 1989, and he stayed in my laboratory for several months. In less than three weeks he was able to adapt his original software to almost all of my multiple requests. We were soon able to upload our averaged MCG data to a PC and perform interactively all analytic procedures (filtering, high-resolution analysis and butterfly presentation of signals, movies of MF maps and localization results obtained with different models, etc.) almost in real time. This was a significant step forward to evaluate MCG clinically. I was enthusiastic and already dreaming about the next step: the development of an automatic procedure for data fusion with anatomical cardiac images inferred from fluoroscopy and echocardiography, when, on November 9, 1989, the Berlin Wall came down. Martin had to rush home to Jena, and my dreams of new developments for MCG once again had to be put on hold. We did on our own have at least a form of a scaled 3D anatomical outline of the heart superimposed on the MF maps (Figure 10.15).

Meanwhile, in order to objectively validate the accuracy of 3D localization of intracardiac sources with MCG, I had refined the nonmagnetic catheter technique[80], constructed different types of nonmagnetic catheters for electrophysiology studies and collected a number of maps during nonmagnetic pacing with different types of dipoles in tanks filled with saline and in patients during electrophysiology studies[81]. In our unshielded catheterization laboratory the average 3D uncertainty of the catheter source localizations in patients was on the order of 12 mm — not bad for an experiment to link noninvasive MCG to invasive clinical electrophysiology. At the end of 1989, a patent application was made based upon using MCG in combination with a nonmagnetic catheter, as a minimally invasive method for magnetically-guided electrophysiology studies, endomyocardial biopsy and ablation, directly aimed at an arrhythmogenic substrate[82]. Experiments with a dog and in vitro had provided data about the MF maps generated by a current dipole implanted at different distances from the sensor[83].

On December 1990 a workshop was organized in Rome by the European Concerted Action on Biomagnetism, on "Non-pharmacological treatment of cardiac arrhythmias: present and future" to inform interventional cardiologists and cardiac surgeons about the potential use of MCG as a method to guide ablation of arrhythmias. The results of several research groups were in good agreement and substantially confirmed that localization of cardiac arrhythmias was a major application of MCG with good prospects. However, the consensus was that simultaneous mapping from multiple locations was mandatory for clinical application and that MCG had to be available in the hospital and utilized routinely by clinicians. Preliminary clinical results, independently reported by Werner Moshage[84] and Vinzenz Hombach[85], obtained with the first multichannel system of 37 first-order axial gradiometers arranged on a flat hexagonal grid (with an instrument named KRENIKON®) were outstanding. This system produced accurate localization of arrhythmogenic substrates and provided data fusion for MRI images of patients with WPW syndrome and with ventricular tachycardia[86]. The accuracy of localization was validated by comparison with ISPECT-radionuclide ventriculography, intracardiac mapping/pacing and with successful catheter ablation. We saw for the first time that, with additional refinements, MCG could yield a new method for 3D imaging during interventional electrophysiology. Later, we had the opportunity to compare our localization results with those obtained with the KRENIKON® on the same patient, who was afflicted with WPW syndrome (Figure 10.16).

[80] R. Fenici et al., *New Trends in Arrhythmias*. 2 (1986) 357
[81] R. Fenici et al., Plenum Press New York, (1989) 361
[82] R. Fenici, CNR, US Patent 5,056,517 (1991)
[83] E. Costa Monteiro et al., *Phys. Med. Biol*. 32 (1987) 65
[84] W. Moshage et al., *Int. J. Cardiac Imaging* 7 (1991) 217
[85] V. Hombach et al., *Int. J. Cardiac Imaging* 7 (1991) 225
[86] P. Weissmüller et al., *Eur. Heart J.* 14 (1993) 61

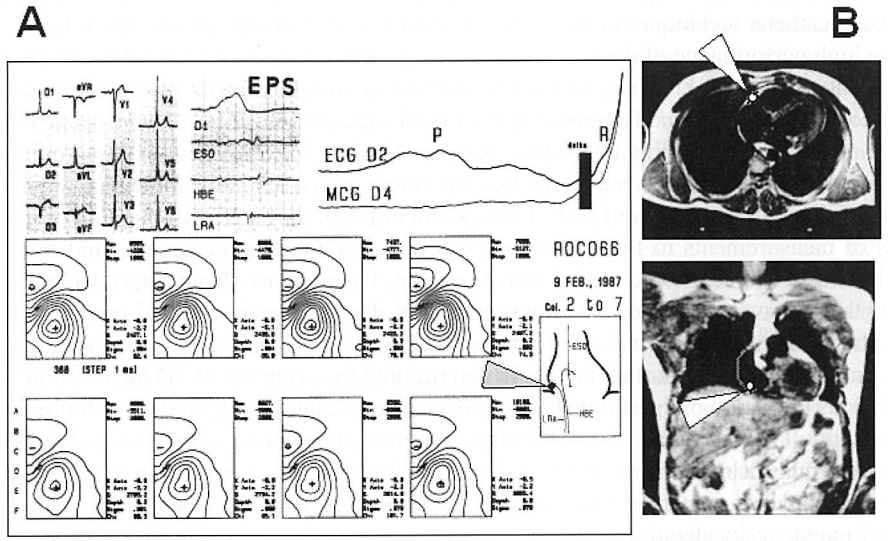

FIGURE 10.16: Patient with the WPW syndrome, studied in Rome with single-channel unshielded MCG on February 9, 1987. (A) MF maps and ECD localization were obtained with Erné's software installed in Rome. The accuracy of localization of the accessory right lateral pathway was validated by catheter mapping (EPS) and marked with the grey arrow onto the heart silhouette inferred by fluoroscopy. In 1992 the same patient was restudied in Erlangen with the 37-channel KRENIKON® system. (B) The localization results, automatically transferred into the patient MRI, marked with white arrows, confirmed the accuracy achievable even with single-channel in an unshielded catheterization laboratory.

10.3.4 From 3D localization to Magnetic Source Imaging

Since the beginning of the 1990s, an increasing number of multichannel systems for MCG mapping were constructed. Some were developed in academic institutions, others as commercial products[87]. Unfortunately, all multichannel systems at that time required electromagnetic shielding. That was the most efficient strategy to reduce ambient electromagnetic noise. For quite some time this had been an expensive drawback to installation of MCG in hospitals for routine daily investigation of a large number of patients. Furthermore, complexity related to cooling via a liquid helium transfer system required coupling to physicists in practically all biomagnetic laboratories, including those in hospitals. This probably created ambivalence toward MCG even among the most interested clinicians because it was not considered something that they could handle on their own, and that at best it was considered as research to be assigned to Ph.D. students. In spite of those drawbacks, since the second half of the 1990s, the increasing availability of high-performance multichannel systems in hospitals has significantly changed the scenario, providing a tool for advanced research in clinical MCG. One typical example of optimal multidisciplinary integration was the set-up of

[87] J. Nenonen, *SQUID Handbook*. Berlin Whiley-VCH, 2 (2005)

the BioMag Laboratory at the Helsinki University Hospital by scientists of the Helsinki University of Technology. In 1995 I had the opportunity to join the Helsinki Group, in the framework of the BIRCH Cardiomagnetism Program, with a research project to validate the accuracy of the improved nonmagnetic catheter technique for magnetically-guided interventional electrophysiology[88], profiting by the high performance of their new multichannel Neuromag system for MCG, installed at the BioMag Center. In Helsinki I enjoyed the friendship and professionalism of top scientists such as Jukka Nenonen (who developed almost in real-time all software interfaces that we needed) and who taught me much about modeling and signal analysis. Markku Makijarvi, in addition to performing interventional procedures in the catheterization laboratory, was a fundamental clinical partner. Katja Pesola was fully dedicated and did part of her excellent Ph.D. thesis working on that project. After hundreds of measurements to test the accuracy of catheter imaging in patients and in a patient-specific boundary element torso model constructed by Uwe Tenner (from Jena), we were able to determine that the average 3D localization precision of the catheter tip was 6–7 mm in patients and 2 mm in phantoms[89,90]. It also was demonstrated that the use of a realistic and patient-tailored torso model is one of the most important factors in determining the accuracy of 3D localization[91,92].

The obvious limitation of the simple ECD model is that it cannot be applied when multiple current sources are simultaneously activated. Under this condition, it is more convenient to solve the inverse problem for a current distribution in terms of the lead fields with a minimum-norm estimate and appropriate techniques to stabilize the solution. Those experiments initiated the transition from the concept of magnetic localization of cardiac sources to that of magnetic source imaging (or MSI) with current density reconstruction. Current density reconstruction from MCG was used to localize the origin of ventricular late fields, atrial reentry circuits, accessory pathways and ischemic regions induced by exercise in patients with ischemic heart disease (IHD)[93,94]. Further refinement of source modeling was the implementation of the uniform double-layer sources model to define the sequence of cardiac excitation, which was validated with intra-operative epicardial recordings in patients undergoing open-chest surgery[95].

High-performance multichannel systems and progressive development in mathematical techniques by combining magnetocardiographic functional imaging with patients' cardiac 3D models obtained with MRI or CT scans, allowed for higher level validation of previous findings on localization of arrhythmias with MCG[96].

10.3.5 To Shield or Not to Shield? The History of Unshielded MCG

One of the most debated issues among investors and people involved in industrial development has been the perennial question of why clinicians did not trust MCG and what should be the best approach to gain their favor? The choice was between highly reliable large-scale MCG systems providing the best signal quality in MSRs and the compromise of less sensitive but budget-priced unshielded MCG-systems. In the 1990s the majority of companies favored the former approach, but costs and space needed for the installation of shielded systems have been major drawbacks for the acceptance of MCG in clinical environments. Indeed, no system was readily available at a patient's bedside, nor was MCG user friendly in the view of clinicians. Furthermore, the sophisticated technology and the complexity of system management (cooling, liquid helium transfer, maintenance, etc.) implied that MCG systems were driven by physicists, since even when a system was installed in a hospital, medical personnel were uncomfortable and skeptical. The lack of "clinical" equipment and of evidence-based clinical benefits in using MCG impeded the creation of a market thus leading to a vicious cycle: No market ⇒ No investments ⇒ No development of "clinical" equipment ⇒ No market.

Only a few people, including myself, were convinced that the only way to break the vicious cycle and promote MCG as a clinical tool was to favor the development of user-friendly multichannel instrumentation capable of working routinely in unshielded hospital cardiology departments and to place this instrument directly in the hands of clinicians. My conviction was based on the Italian experience in which neuromagnetism had absorbed most of the research funding, and there was no way to get institutional support to install an expensive MSR mandatory for commercial multichannel MCG systems available at that time. On the other hand, based on our 10 years' experience with the IESS's single channel, I was sure that it was possible to construct a gradiometer-based multichannel system capable of working even in an unshielded catheterization laboratory. Having a goal of using MCG as an ambulatory diagnostic tool and as a real-time method to assist interventional electrophysiology, I continued to publicize my vision, but with little success. It took almost ten years to find someone willing to provide resources to construct an unshielded multichannel MCG system. Meanwhile, thanks to the Helmholtz reciprocity theorem, someone else invented and commercialized the first "magnetic" method for 3D catheter-based electro-anatomical imaging[97], which became a "best seller", and these days is used in all catheterization laboratories for interventional electrophysiology.

Unexpectedly, in 1997, I received an invitation to speak about MCG to a small group of experts in cardiac electrophysiology, at a meeting organized by Cryogenic Electronic Systems (CES), in connection with a meeting of the American College of Cardiology in Anaheim, to stimulate the interest of American cardiologists for MCG. As always, I faced more skepticism than real interest. However, I also had the opportunity to visit Alexander Bakharev's company in Springfield, MA and to play with his 7-channel prototype for unshielded MCG. With some manipulation of the system and much discussion, we considered scientific cooperation to develop "my" multichannel system, which became a reality a few years later after receiving a grant from the National Ministry of Research. This provided me the opportunity to co-finance the project thanks to the trust of Carl Rosner, CEO of the newborn CardioMag Imaging Inc., the successor company to CES. We had to proceed step-by-step. First a 9-channel prototype was installed in my lab as a test system. The 9-channel prototype was ready to record clinical MCG at the beginning of 2001[98]. Based on that experience, the unique unshielded 36-channel system was constructed and installed in our catheterization laboratory in 2002[99]. With that instrumentation it was finally possible to study many patients a day on an ambulatory basis, with immediate diagnostic feedback (the time required for a standard ambulatory mapping was only 90 seconds and post-processing for 3D imaging took less than a minute). We soon confirmed that imaging of the cardiac MF was possible, even on a beat-to-beat basis, during interventional electrophysiology. Preoperative localization of arrhythmogenic substrates was successful to guide ablation in patients with WPW syndrome, atrial fibrillation and ventricular arrhythmias. It also was proven that biomagnetic driving of an nonmagnetic catheter for action potential recording of an arrhythmogenic target was possible, and useful to define arrhythmogenic mechanisms[100] (Figure 10.16). These features also were confirmed by extensive experimental research on small animals. They underwent multiple magnetic mappings with simultaneous invasive electrophysiologic

[88] R. Fenici, CNR US Patent 6,527,724, (2003)
[89] R. Fenici et al., *Pacing Clin. Electrophysiol.* 21 (1998) 2492
[90] R. Fenici et al., *Pacing Clin. Electrophysiol.* 21 (1998) 2485
[91] R. Fenici et al., *Pacing Clin. Electrophysiol.* 21 (1998) 2485
[92] K. Pesola et al., *Phys. Med. Biol.* 44 (1999) 2565
[93] U. Leder et al., *Int. J. Cardiol.* 64 (1998) 83
[94] J. Nenonen et al., *J. Electrocardiol.* 34 (2001) 37
[95] T. Oostendorp, K. Pesola, *Proc. 12th Int. Conf. Biomagn.* (2001)
[96] W. Moshage et al., *Radiology* 180 (1991) 685
[97] S.A. Ben-Haim et al., *Nature Medicine* 2 (1996) 1396
[98] R. Fenici et al., *Biomedizinische Technik* 2 (2001) 219
[99] R. Fenici R et al., *Int. J. Bioelectromagnetism* 5 (2003) 80
[100] R. Fenici, D. Brisinda, *J Electrocard.* 40 (2007) S47

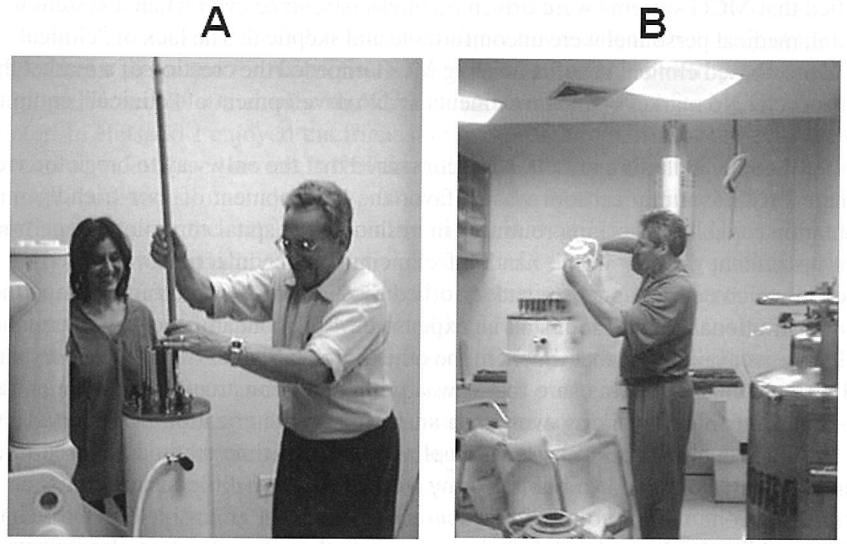

FIGURE 10.17: History of unshielded multichannel MCG in the catheterization laboratory of the Biomagnetism Center, at the Catholic University of Rome. (A) Alexander Braginski and Donatella Brisinda working at the installation of the 9-channel "scout" system in 2001. (B) Alexander Bakharev is starting the cooling procedure of the 36-channel system in 2002.

procedures, carried out with nonmagnetic catheters 3D and localized via MCG[101,102,103]. The next mandatory step was the development of appropriate software for real-time 3D and 4D biomagnetic imaging of the nonmagnetic catheter during interventions, but this was unfortunately considered a "low priority" by venture capitalists, who focused investment on development on automatic diagnosis of myocardial ischemia[104]. A (9-channel) scaled-down version for unshielded MCG, received the approval of the US Food and Drug Administration (FDA) as a tool for clinical analysis of cardiac health. The 9-channel system was installed in leading hospitals and research centers of the US, Germany and China, especially in intensive care units or emergency rooms, where it was successfully tested for the triage of patients with chest pain, with or without myocardial ischemia (see below). At the same time, similarly downscaled systems with different numbers of channels were used in Germany and Russia[105,106]. Those systems for unshielded MCG have been mostly disregarded by the supporters of huge supersensitive shielded installations, but these unshielded systems have made a significant contribution to bringing MCG closer to the patient's bedside, to increase the number of patients investigated in clinical environments, and to enhance the interest of cardiologists for this di-

[101] D. Brisinda et al., *Basic Res. Cardiol.* 99 (2004) 193
[102] D. Brisinda et al., *Am. J. Physiol. Heart Circ. Physiol.* 291 (2006) H368
[103] D. Brisinda et al., *Physiological Measurement* 28 (207) 773
[104] A.A. Bakharev, PCT Application U.S. Prov. Appl. No.: 60/228,640 (2001)
[105] A. Gapelyuk et al., *J. Electrocardiol.* 40 (2007) 401
[106] R. Fischer et al., *Am. J. Physiol. Heart Cir., Physiol.* 293 (2007) H1242

agnostic tool, at least for its use for early detection of ischemic heart disease[107,108,109]. On the other hand, clinicians acknowledging the usefulness of MCG have realized that they needed a "real" multichannel system for clinical use. Unfortunately, no such system was commercially available, so unshielded MCG has not taken-off. That is a brief history of unshielded MCG. However, now the debate "to shield or not" is becoming obsolete. In fact, technological progress can provide more flexible shielding solutions which are more easily adaptable in almost all clinical environments at an affordable cost. Thus, the answer to the title question of this section is no longer "yes" or "no", but rather what kind of shielding might be necessary to guarantee optimal reliability and sensitivity in various clinical environments.

10.3.6 Clinical Perspectives

Although from an analysis of the literature the number of patients so far investigated with MCG is on the order of thousands, clinical validation of MCG is still far from the standard required on the basis of the AHA/ACC/ESC recommendations for the acceptance of new technologies. In fact, with few recent exceptions, reported clinical experience is based on studies that have rarely enrolled more than 250 patients. Furthermore, randomized controlled multicenter trials of MCG haven't been done. On the other hand, the safety and reproducibility of human recordings have been successfully demonstrated, and the FDA has approved MCG as a clinical method to measure the cardiac MF since 2004. Meanwhile, thanks to the increasing number of trials, clinical experience in MCG is progressively growing worldwide and new insights have been provided[110,111]. Successful results have been reported in several clinically-relevant applications that are summarized in Table 10.1.

TABLE 10.1: Most Relevant Clinical Applications of Magnetocardiography

Detection of myocardial ischemia and viability (rest and stress MCG)
Arrhythmogenic risk assessment
Noninvasive electroanatomical imaging of arrhythmogenic substrates
- WPW syndrome
- Ventricular arrhythmias
- Atrial fibrillation
- Brugada syndrome
Preoperative programming of robotic ablation systems
Fetal magnetocardiography

10.3.7 Detection of Myocardial Ischemia and Viability (Rest and Stress MCG)

By far, the major focus of research in clinical MCG has been the definition of its predictive value for early diagnosis of IHD and myocardial viability. This is understandable since IHD is the leading cause of death in western countries. Moreover, noninvasive early detection of myocardial ischemia is still a major clinical problem, because early ischemia induces changes in the electrophysiological properties of the myocardium that often are not visible in at-rest ECG, but which are detectable

[107] K. Tolstrup et al., *Cardiology* 106 (2006) 270
[108] J.W. Park et al., *Critical Path. Cardiology* 1 (2002) 253
[109] W.W. Quan et al., *Chin. Med.* J. 121 (2008) 22
[110] R. Fenici et al., *Expert Review of Molecular Diagnostics* 5 (2005) 291
[111] I. Tavarozzi et al., *Ital. Heart* J. 3 (2002) 151

by MCG. In fact, compared with ECG, MCG is more sensitive to tangential currents, curl currents and transmural current flow; and it can detect a closed-looped current that is invisible to ECG[112]. A first demonstration of the unique potential of MCG for the study of acute myocardial ischemia was provided in the 1070s by Cohen et al., who used experimental measurements to reveal near-DC changes related to ischemic injury currents, and which were not detected by ECG[113]. Further studies have subsequently confirmed the reproducibility of MCG for longitudinal investigation of acute and chronic ischemia-induced alteration of myocardial electrophysiological properties[114,115,116]. Saarinen et al. and later Savard et al. were the first to explore S-T shifts in MCG due to exercise tests[117]. Unfortunately, although the method was feasible in patients, it had no follow-up until the end of the 1990s when Brockmeier et al. demonstrated that pharmacological stress in normal subjects showed more distinct repolarization changes in multichannel MCG than in simultaneously recorded 32-lead ECG[118].

In 2000, Hänninen et al. described, in IHD patients, a rotation of the maximum spatial gradient of the MF pattern at the S-T-segment (α angle) induced by exercise, which slowly reverts to the basal pattern during the recovery phase. Such exercise-induced rotation of the "α angle" parameter was useful to differentiate patients with coronary artery lesions.

In patients with multi-vessel coronary artery disease, equivalent current-density estimation, computed from MCG after exercise-induced ischemia, showed good agreement between segments of high current density and viable myocardium in PET, as well as between low current density and scars[119]. It also was reported that percutaneous transluminal coronary angioplasty (PTCA) reperfusion is characterized by a more homogeneous current density distribution during repolarization as early as one month after the procedure[120]. In 2003, Kanzaki et al. reported 83% diagnostic accuracy for exercise MCG and concluded that the MF in the depolarization process can detect the subtle myocardial ischemia induced by exercise[121]. Brisinda et al. confirmed that the same exercise-induced ischemic alteration of MCG parameters described by Hänninen was detectable also with unshielded MCG[122]. Many other studies, carried out in both shielded and unshielded laboratories, have confirmed that several parameters, calculated along the ST interval and T-wave, were typically abnormal in at-rest MCG for patients with IHD, and they seem to be sensitive diagnostic markers of early ischemia. On this basis MCG recently has been proposed as the front-line method for non-invasive triage of patients with chest pain, but who exhibit normal ECG and cardiac enzyme screening[123,124,125,126,127,128,129,130]. Hailer et al. studied 177 patients with no prior myocardial infarction and with stable angina and coronary artery disease (CAD) documented by coronary angiography. They also studied 123 patients admitted to hospital with typical chest pain, but without hemodynamic relevant stenosis of the coronary arteries. They concluded that, contrary to ECG, unshielded MCG identified CAD patients at rest with satisfactory sensitivity (73.3%) and specificity (70.1%)[131]. Tolstrup et al. reported two multicenter studies from 2 sites in the US, one in Germany and one in Italy, evaluating ventricular repolarization by MCG, in more than 100 subjects with chest-pain syndrome. All had a normal or nonspecific 12-lead ECG and normal troponin level. They concluded that at-rest MCG accurately detects myocardial ischemia in chest pain patients when 12-lead ECG and troponin appear normal or nonspecific[132,133]. Similar results were cited by other authors[134], even investigating non-STEMI patients[135], i.e., patients with partially blocked arteries.

Several attempts have been reported aimed at reliable methods for automatic computing of MCG

[112] J.P. Wikswo, J. Barach, *J. Theor. Biol.* 95 (1982) 721
[113] D. Cohen et al., *Science* 172 (1970) 1329
[114] E.C. Monteiro et al., *Physiol. Meas.* 18 (1997)191
[115] R. Fischer et al., *Int. Cong. Series* 1300 (2007) 484
[116] A. Brazdeikis et al., *Neurol. Clin. Neurophysiol.* 30 (2004) 16
[117] M. Saarinen et al., *Cardiovascular Res.* 8 (1974) 820
[118] K. Brockmeier et al., *J. Cardiovasc. Electrophysiol.* 18 (1997) 615
[119] J. Nenonen et al., *J. Electrocardiol.* 34 Suppl (2001) 37
[120] T. Hecker et al., *Proc. 12th Int. Conf. Biomagn.* (2001) 572
[121] H. Kanzaki et al., *Basic Res. Cardiol.* 98 (2003) 124
[122] D. Brisinda et al., *Biomed. Tech.* 48 (2004) 137
[123] K. Tsukada et al., *Int. J. Card. Imaging*. 16 (2000) 55
[124] J. Shiono et al., *Pacing Clin. Electrophysiol.* 25 (2002) 915
[125]. Van Leeuwen et al., *Pacing Clin Electrophysiol.* 26 (2003) 1706
[126] H. Kanzaki et al., *Basic Res. Cardiol.* 98 (2003) 124
[127] D. Brisinda et al., *Lect. Notes Comput.* Sc. 2674 (2003) 122
[128] B. Hailer et al., *Clin. Cardiol.* 26 (2003) 465
[129] B.G. Schless et al., *J. Med. Eng. Technol.* 28(2004) 56
[130] J.W. Park et al., *ANE* 3 (2005) 312

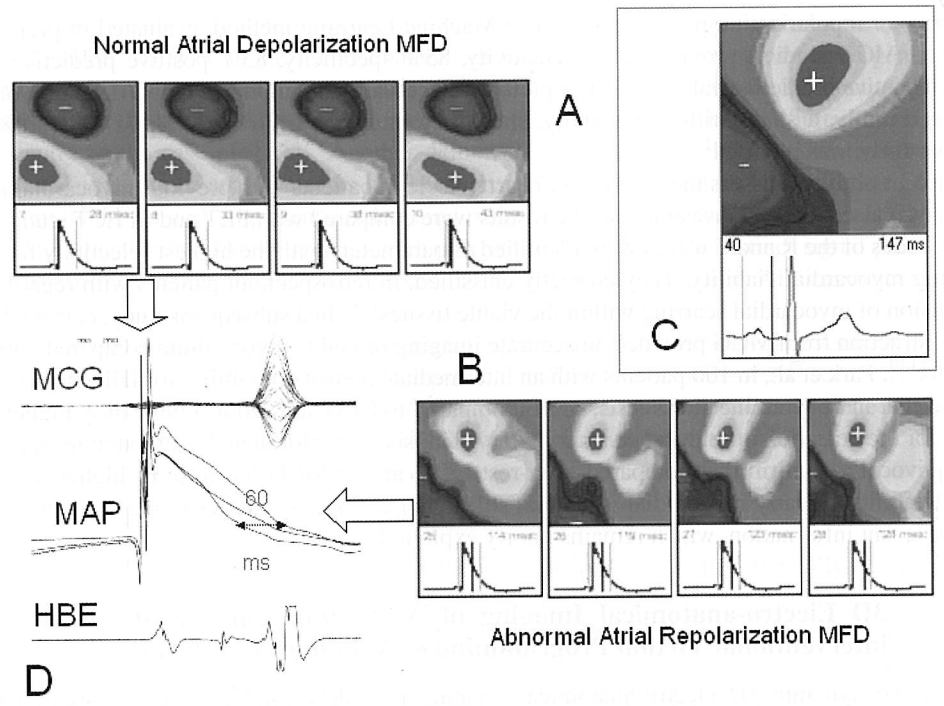

FIGURE 10.18: Example of MCG detection of atrial electrophysiological abnormality in a patient with paroxysmal atrial flutter. High-resolution MCG of atrial activation evidences a normal MF distribution during atrial depolarization (A), but abnormal MF distribution during atrial repolarization (B); for comparison an example of normal atrial repolarization MF is shown in the upper right square (C). The simultaneous recording of multiple monophasic action potentials with an amagnetic catheter (MAP in D) validates the noninvasive MCG finding as related to an abnormal (60 ms) local dispersion of atrial repolarization [modified from R. Fenici, D. Brisinda, *J. Electrocardiol.* 40 (Suppl. 1) (2007) 47].

[131] B. Hailer et al., *Pacing Clin. Electrophysiol.* 28 (2005) 8
[132] K. K. Tolstrup et al., *Circulation* suppl 110 (2004) 743
[133] K. Tolstrup et al., *Cardiology* 106 (2006) 270
[134] K. On et al., *Circ.* J. 71 (2007) 1586
[135] H.K. Lim et al., *Ann. Med.*39 (2007) 617

ventricular repolarization parameters[136]. The Machine Learning method, evaluated in preliminary clinical MCG studies, provided 75% sensitivity, 85% specificity, 83% positive predictive value, 78% negative predictive value, and 80% predictive accuracy for automatic MCG detection of IHD. More recently, a study with a sensitivity, specificity and accuracy of 86.2%, 72.7% and 80.4%, respectively, was reported[137].

MCG's ability to assess the viability of heart muscle in patients with previous myocardial infarction (MI) also has been investigated. The results were compared with PET and SPECT studies. The amplitudes of the R and T waves were identified as parameters with the highest selectivity for determining myocardial viability. They correctly classified, in retrospect, all patients with regard to the extension of myocardial scarring within the viable tissues[138]. In a subsequent study, current density reconstruction from MCG provided an accurate imaging of viable myocardium compared with PET results[139]. Park et al., in 100 patients with an intermediate pretest probability for IHD, have recently found that in dobutamine stress tests, MCG compared to ECG showed a significantly higher accuracy for the detection of relevant coronary artery stenosis[140]. Unfortunately, although recent studies unequivocally confirm that compared to at-rest ECG, at-rest MCG has a much higher diagnostic predictability of early myocardial ischemia, still major cardiology journals give "low priority" to this relevant information, which remains poorly exploited.

10.3.8 3D Electro-anatomical Imaging of Arrhythmogenic Substrates and Pre-interventional Virtual Programming of Ablation Procedures

Invasive dynamic 3D electro-anatomical imaging is widely used for precise ablation of arrhythmogenic substrates[141] and to visualize robotic navigation of electro-catheters from a remote radiation-free location[142]. Noninvasive MCG 3D imaging of the patient's heart obtained from cardiac MDCT (Multi-Detector Computed Tomography) or MRI is envisioned as a means to provide a virtual model to plan the ablation procedure non-invasively and to test non-invasively its efficacy prior to the intervention. This already has been proven effective for the targeted ablation of accessory pathways and ventricular arrhythmias[143]. The new challenge is to develop pre-interventional classification of patients with AF, an arrhythmia that impairs quality of life, leading to increased risk of cardiovascular complications in millions of patients. Although the HRS/ECAS/EHRA expert Task Force agrees that catheter ablation of AF in general should not be considered as the first choice for therapy[144], there is a consensus that symptomatic AF is an indication for catheter ablation. Catheter ablation of AF is a demanding intervention that may result in complications, thus it should be planned only after carefully weighing the risks and benefits of the procedure.

A first tentative MCG recording of paroxysmal supraventricular tachyarrhythmias was reported in 1994[145], but real imaging of atrial re-entry arrhythmias with MCG appeared only after 2000. Since then several authors have shown that magneto-cardiographic mapping is able to identify different activation patterns in the sinus rhythm and during atrial arrhythmias, with accuracy good enough to improve clinical understanding of AF pathogenesis and to select subgroups for patient-tailored therapy. Yamada et al. reported that the time-motion of the tangential component of the atrial MF

[136] F.E. Smith et al., *Pacing Clin. Electrophysiol.* 26 (2003) 2096
[137] T. Tantimongcolwat et al., *Computers in Biology and Medicine* 38 (2008) 817
[138] A. J. Morguet et al., *Coronary Artery Dis.* 15 (2004) 155
[139] M. Goernig et al., *Comput. Med. Imaging Graph.* 33 (2008) 1
[140] J.W. Park et al., *Clin. Hemorheol. Microcirc.* 39 (2008) 21
[141] C. Blomstrom-Lundqvist et al., *Circulation* 108 (2003) 1871
[142] S. Ernst et al., *Circulation* 109 (2004) 1472
[143] D. Brisinda, R. Fenici, *Pacing Clin. Electrophysiol.* 30 (Suppl 1) (2007) S151
[144] H. Calkins et al., *Heart Rhythm* 4 (2007) 816
[145] R. Fenici et al., in: *High-Resolution Electrocardiography Update.* Moduzzi Edizioni (1994) 73

was useful to noninvasively identify the mechanisms responsible for different atrial tachyarrhythmias[146]. In 2005 Nakai et al. used a 64-channel MCG and current density imaging to generate a 3D heart outline in patients with AF and atrial flutter and demonstrated that the conduction pattern generated within the heart had a counterclockwise rotation in patients with atrial flutter and random micro-reentry in the case of AF[147]. Another demonstration that MCG is an efficient method for mapping and imaging of atrial currents has been provided by Kim at al., who used the results to guide minimal AF surgery in patients undergoing mitral valve replacement[148]. MCG was useful to distinguish clinical subclasses of patients with paroxysmal lone AF with distinct signal profiles of atrial depolarization and to demonstrate that susceptibility to paroxysmal lone AF is associated with altered intra-atrial conduction modalities[149].

Numerous other studies suggest that, although needing further technological development, pre-interventional noninvasive characterization of patients with different kinds of AF seems to be one of the most promising clinical applications of MCG in the near future, especially since magnetic imaging of AF activity is possible in an unshielded catheterization laboratory[150].

10.3.9 Arrhythmogenic Risk Assessment

Noninvasive identification of patients at risk of sudden arrhythmic death is typically based on the demonstration of myocardial activation abnormality during ventricular depolarization, on abnormal inhomogeneity of ventricular repolarization, and on abnormal heart rate variability parameters. Each of the above-mentioned parameters can be noninvasively studied with ECG. However, non-contact cardiac mapping with MCG is faster, provides evaluation of all parameters with a single recording session, and might exhibit 3D imaging of arrhythmogenic mechanisms. Moreover, in comparison to ECG, MCG is more sensitive to tangential arrhythmogenic currents predominantly induced by structural alteration occurring after a myocardial infarction[151] and can detect electrically silent sources such as "vortex currents"[152,153,154]. Arrhythmogenic ventricular depolarization abnormalities can be detected with high-resolution MCG as low-amplitude "late magnetic fields" at the end of QRS[155,156], or with intra-QRS fragmentation[157].

Intra-QRS fragmentation analysis, obtained by applying binomial filtering to detect polarity changes inside QRS, was efficient in identifying patients prone to ventricular tachycardia (VT) after a MI[158]. Increased intra-QRS fragmentation also can be an early sign of diabetes-associated cardiomyopathy[159]. MCG identifies abnormal inhomogeneity in ventricular repolarization[160]. An abnormal dispersion of the late part of the T wave interval ($T_{apex} - T_{end}$ interval), which is an index of transmural repolarization inhomogeneity, was found in patients with sustained VT, due to previous MI and with idiopathic dilated cardiomyopathy. Interestingly, MCG simultaneously iden-

[146] S. Yamada et al., *Europace* 5 (2003) 343
[147] K. Nakai et al., *Int. J. Cardiovasc. Imaging* 21 (2005) 555
[148] D. Kim et al., *Interactive Cardiovascular and Thoracic Surgery* 6 (2007) 274
[149] R. Jurkko et al., *Europace* 11 (2009) 169
[150] R. Fenici, D. Brisinda, *The Anatolian J. Card.* 7 (Suppl. 1) (2007) 23
[151] D.R. Bolick et al., *Circulation* 74 (1986) 1266
[152] K. Brockmeier et al., *J. Cardiovasc. Electrophysiol.* 18 (1997) 615
[153] F.J. van Capelle, D. Durrer, *Circ. Res.* 47(1980) 454
[154] M. Liehr et al., *Ann. Biomed. Eng.* 33 (2005) 240
[155] P. Korhonen et al., *J. Cardiovasc. Electrophysiol.* 11 (2000) 413
[156] P. Korhonen et al., *Pacing Clin. Electrophysiol.* 25 (2002) 1339
[157] M.K. Das, E. Masry, *Curr. Opin. Cardiol.* 25 (2010) 59
[158] P. Korhonen et al., *Pacing Clin. Electrophysiol.* 24 (2001) 1179
[159] K. Brockmeier et al., *J. Electrocardiol.* 30 (1997) 239
[160] K. Nakai et al., *Int. Heart J.* 48 (2007) 701

tified late fields and $T_{apex} - T_{end}$ alteration only in post-MI patients. In post-MI patients, both MCG late fields and intra-QRS fragmentation parameters differed significantly between patients with and without a propensity to sustained VT, but the abolition of the arrhythmic substrate with antiarrhythmic surgery rendered both late field and intra-QRS fragmentation parameters almost similar to those of the post-infarction patients without a VT propensity[161,162]. MCG has been used to localize late fields and to investigate their relation to the location of the arrhythmogenic substrate[163]. The prolongation of the QT interval (i.e., the intervals from the QRS onset to the offset of the T-wave) and its inhomogeneity is another indicator of propensity to life-threatening ventricular arrhythmias and sudden death. Automatic calculation of QT interval duration at multiple locations above the heart and the reconstruction of the spatial distribution of QT dispersion from MCG has proven more sensitive than 12-lead ECG recordings in screening post-MI patients at risk to develop sustained VT[164].

In addition to morphological HR analysis of MCG signals, the extraction of the spatial features of MF distribution provides additional information about vulnerability to arrhythmia. Another example of a potential clinical application of non-invasive imaging of myocardial arrhythmogenic currents with MCG is the study of patients with the Brugada syndrome (BS), an inherited arrhythmogenic disease characterized by a typical electrocardiographic pattern with ST-segment elevation in leads V1 through V3, incomplete right bundle-branch block (RBBB) and an enhanced risk of sudden cardiac death because of ventricular fibrillation (VF) or rapid polymorphic VT[165].

10.3.10 Fetal Magnetocardiography

Fetal monitoring is another unquestionable clinical application of MCG, despite recent improvements in detecting fetal ECG, not only during labor,[166,167] but also with surface electrodes during pregnancy[168]. A recent review is available that covers the history of fetal magnetocardiography (FMCG)[169]. Thus we summarize only some key points which are relevant to clinical application. It is well known that FMCG was initiated in Finland in 1974 with an unshielded SQUID system[170]. Thereafter, most FMCG studies have been carried out in MSRs with different MCG systems, including a 151-channel system specifically designed for magnetic study of fetal cerebral, cardiac and uterine activities[171]. Now FMCG is recognized as a reliable method for noninvasive surveillance of fetal cardiac electrophysiology, especially during the second half of pregnancy, when the presence of electrically insulating vernix caseosa impairs the quality of fetal ECG recording with abdominal leads[172].

Shielded FMCG has proven reliable to measure standard cardiac intervals[173,174], heart rate and its variability (HRV)[175,176], to monitor fetal neurodevelopment[177], to detect and classify fetal arrhythmias[178], to identify and treat arrhythmogenic risk factors, such as heart block, ventricular preexcitation[179,180] or long QT syndromes[181] and other pathological conditions which can jeopardize the fetus or the survival of the newborn after the delivery, such as intrauterine growth retardation, fetal distress and congenital heart defects. Although MSRs provide ideal conditions to study the FMCG on a beat-to-beat basis according to established standards, more widespread routine clinical use of this innovative method is expected by bringing FMCG to the patient's bedside and by minimizing its cost. For this reason, several attempts have been reported (since 1982) to record FMCG without employing MSRs[182]. The quality of unshielded FMCG signals was good enough to detect the FMCG waveform, to measure cardiac intervals and to analyze fetal heart rate variability[183] since the 36th week of gestation, with an acceptable signal-to-noise ratio, even using HTS SQUID technology[184]. Additionally, multichannel mapping of FMCG has been successfully performed in unshielded clinical environments on an ambulatory basis. In this clinical arrangement, real-time FMCG signals were noisy, but visually perceptible from the 28th week of gestation. However, after averaging, signal resolution was good enough to measure cardiac intervals, to reconstruct MF maps and to localize fetal ventricular activity[185]. Further improvement of the signal quality was achieved with the Independent Component Analysis approach[186], making it possible to measure cardiac intervals beat-to-beat and to evaluate the HRV parameters.

10.3.11 Conclusions

As stated in the introduction, this review of MCG has been written focusing on personal memories linked to achievements in the field, rather than as a dry scientific monograph. It is worth noting that the number of indexed papers in clinical MCG has increased almost exponentially through the years, and that there are many others that have not appeared in PubMed. Thus, we apologize to those scientists whose work might have been unintentionally forgotten or quoted superficially.

Concerning the future of MCG, we believe that the most important achievements have yet to come. Certainly SQUID development and improvements had a key role for the progress of biomagnetism in general and cardiomagnetism in particular. However, although it might seem unfair to close a review on clinical applications of superconductivity with this statement, we believe that the widespread clinical use of MCG will occur only with the advent of a new generation of multichannel instruments based on non-cryogenic sensors such as, for example, laser-based optically-pumped magnetometers, which should be less expensive, more compact, practically maintenance-free[187] and hopefully available soon at the patient's bedside. Preliminary validation of single-channel optic MCG mapping showed that the method is promising[188]. Since then significant progress has been made with the preliminary clinical testing of a laser-pumped 19-channel second-order magnetome-

[161] L. Oikarinen et al., *J. Cardiovasc. Electrophysiol.* 12 (2001) 1115
[162] P. Korhonen et al., *J. Cardiovasc. Electrophysiol.* 12 (2001) 772
[163] P. Weismüller et al., *Eur. Heart J.* 14 (1993) 61
[164] P. Van Leeuwen P et al., *Pacing Clin. Electrophysiol.* 19 (1996) 1894
[165] P. Brugada et al., *Circulation* 97 (1998) 457
[166] K.G. Rosen, Curr. *Opin. Obstet. Gynecol.* 17 (2005) 147
[167] I. Amer-Wahlin et al., *B.J..O.G.* 112 (2005) 160
[168] F. Mochimaru et al., *Jpn. J. Physiol.* 54 (2004) 457
[169] S. Srinivasan, J. Strasburger, *J. Curr. Opin. Pediatr.* 20 (2008) 522
[170] V. Kariniemi et al., *J. Perinat. Med.* 2 (1974) 214
[171] C.L. Lowery et al., *Am. J. Obstet. Gynecol.* 188 (2003) 1491
[172] S. Comani et al., *Physiol. Meas.* 26 (2005) 193
[173] S. Comani, G. Alleva, *Physiol. Meas.* 28 (2007) 49
[174] P. van Leeuwen et al., *Physiol. Meas.* 25 (2004) 539
[175] S. Lange et al., *Early Hum. Dev.* 85 (2009) 131
[176] U. Schneider et al., *Early Hum. Dev.* 86 (2010) 319
[177] R.B Govindan et al., *Am. J. Obstet. Gynecol.* 196 (2007) 572
[178] A. Fukushima et al., *Heart Vessels* 25 (2010) 270
[179] L.K. Hornberger, K. Collins, *J. Am. Coll. Cardiol.* 51 (2008) 85
[180] H. Zhao et al., J. *Am. Coll. Cardiol.* 2008 51 (2008) 77
[181] T. Menendez et al., *Pacing Clin. Electrophysiol.* 23 (2000) 1305
[182] I. Awano et al., J. *Exp. Med.* 138 (1982) 367
[183] J.A. Crowe et al., *Physiol. Meas.* 16 (1995) 43
[184] Y. Seki et al., *Rev. Sci. Instrum.* 79 (2008) 036106
[185] D. Brisinda et al., *Prenat. Diagn.* 25 (2005) 376
[186] S. Comani et al., *Phys. Med. Biol.* 52 (2007) N87
[187] G. Bison et al., *Appl. Phys.* 76 (2003) 325
[188] R. Fenici et al., *Biomedizinische Technik* 48 (2004) 192

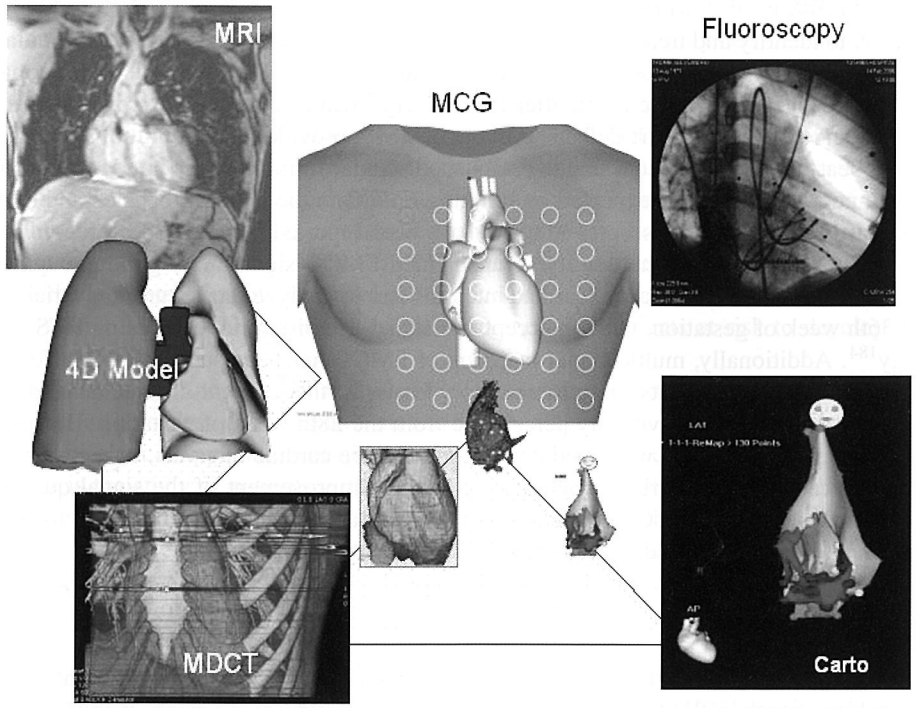

FIGURE 10.19: Future imaging for interventional electrophysiology is foreseen as the multimodal integration between preinterventional MCG-based electro-anatomical imaging into patient's 4D model of beating heart in a breathing chest obtained with cardiac magnetic resonance imaging (MRI) and interventional fluoroscopic and non-fluoroscopic catheter navigation [modified from R. Fenici, D. Brisinda, *The Anatolian Journal of Cardiology* 7 (Suppl. 1) (2007) 23].

ter[189] and the development of new technology for the construction of a compact sensor module for a multichannel sensor head with 57 primary channels to be installed in hospitals[190]. The new sensor head should allow the recording of cardiac MF maps with a spatial resolution comparable to existing SQUID-based systems and with sensitivity adequate to record diagnostically relevant information at least in the QRS-complex and the T-wave. At present optically-based magnetometry still needs some shielding, but the reduction of cost of such systems might favor the acceptance of MCG in clinical environments in the near future.

10.4 MRI (Magnetic Resonance Imaging) Instrumentation and Applications

Jim Bray and Kathleen Amm

MRI provides the largest commercial market using superconductors today, at a size currently of about $3.6 billion/year and growing. Here we discuss how this market arose and how superconductors are employed within it.

[189] A. Weis et al., BIOMAG 2010, *IFMBE Proceedings* 28 (2010) 58
[190] G. Lembke et al., BIOMAG 2010, *IFMBE Proceedings* 28 (2010) 62

10.4.1 Basic Principles of MRI

Since being discovered by Paul Lauterbur[191] in 1973, MRI took only a little over a decade to become a major medical imaging technology. The MR signal has its origin in the spin of atomic nuclei with an odd number of protons or neutrons.

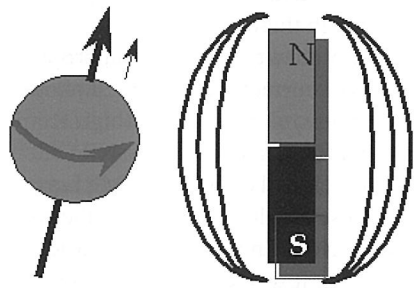

FIGURE 10.20: Dipole magnetic moment.

Spin is a basic property of elementary particles and produces a magnetic dipole in the particle (see Figure 10.20) with a magnetic moment given by the equation

$$\mu = \gamma \hbar \mathbf{I}$$

where γ is the gyromagnetic ratio (the ratio of dipole moment to the angular momentum), $\hbar$ is Planck's constant divided by 2π, $\mathbf{I}$ is the spin and μ is the magnetic moment. When the magnetic moments are placed in a magnetic field B_0, they become partially magnetized. In a 2-state system such as spin = 1/2, the distribution of the magnetic moments will be determined by a Boltzmann distribution:

$$\frac{N^-}{N^+} = e^{\Delta E/k_B T} \qquad \Delta E = \gamma \hbar B_0$$

$N^-/N^+ \approx 0.999993$ for hydrogen at $B_0 = 1.5$ tesla, where N^+ and N^- are the spins aligned parallel to the field and anti-parallel to the field, respectively, T is the absolute temperature, and k_B is Boltzmann's constant. The energy difference between the up and down spins, ΔE, corresponds to a frequency ω of RF radiation by the equation $\Delta E = \hbar\omega$, which specifies a photon energy. Precisely, this energy causes a resonant transition between the two spin states, and this transition is the basis for NMR. The higher energy spin state can be populated by absorption of resonant photons. It will then decay back to its equilibrium population governed by the temperature T and magnetic field B_0, and the emitted photons from this decay process can be detected with appropriate receiving antennas in the vicinity. These decay times are labeled by names such as T_1 and T_2 and are defined by the detailed interactions among the spins and magnetic fields in the system. This absorption and emission of precise photons forms the basis for NMR.

MRI adds to the NMR process the spatial localization of the spins. Since the NMR RF frequency is dictated by the magnetic field at the nucleus, we can add a gradient magnetic field to B_0 to produce a different field at each location in the imaged body. Every location will then have its own resonant NMR frequency that can identify it when it emits from an excited state. Since a certain number of spins are necessary to achieve a practical signal-to-noise ratio (SNR) for each frequency, the imaged body is typically divided into voxels, which are the minimum volume elements required to achieve an acceptable SNR. To date, a plethora of methods have been developed for applying the gradient magnetic fields and RF spin-excitation fields in time and space to achieve optimal desired results in the image. Different features in the human body can be emphasized by various combinations of gradients and RF, which may emphasize spin density or different decay processes of the spins (e.g., T_1, T_2).

In an MRI machine, only the main, large, static field, B_0, is produced by superconductors (SC)[192]. B_0 is produced axially inside the bore of a superconducting solenoidal coil in most MRI machines,

[191] P. C. Lauterbur, *Nature* 242 (1973) 190
[192] Y. Lvovsky and P. Jarvis, *IEEE Trans. Appl. Supercon.* 15 (2005) 1317

although some machines ("open MRI") produce this field with a pair of Helmholtz coils. The open MRI machines allow larger access to a less tunnel-like volume, sometimes relieving patient claustrophobia, but cannot support as large a magnitude of B_0. From the above discussion, it should be apparent that a strong requirement on B_0 is that it be very uniform in the imaging space, since spatial localization of the nuclei depends on knowing precisely the field value at each voxel location. Inhomogeneities in B_0 will also cause loss of SNR from faster decay of excited nuclear spins. Imaging and SNR improve as B_0 increases, and this provides another motivation for using superconducting coils, since they can produce higher fields than copper, although there are limits to this process[193]. The ever-changing gradient and RF fields are produced by copper wires driven by appropriate electronics since superconductors are not lossless under ac fields or currents. The emitted photons from the excited nuclei are also generally received by copper antennas, although HTS (high temperature superconducting) materials have occasionally been employed for this to enhance SNR[194].

The future of HTS in MRI is an interesting question. At present, all commercial MRI systems use LTS (low temperature superconductors), and almost all of these employ NbTi wires, the workhorse of superconductivity. The only uses of HTS in MRI so far have been in experimental RF receiver coils[194] and as current leads for a few low-volume systems. Yet, it would seem obvious that operating at the higher temperatures afforded by HTS would lead to simpler construction of the cryogenic subsystems. The answer lies in the economics: even with the benefit of the cost reduction of the cryogenics, HTS wires are at present too expensive to compete with NbTi, which is easily available in many forms at a cost of around $2/kA-m. HTS wire prices are at present around 100× higher, and this rules out their use. Additional disadvantages of HTS are availability of HTS in limited geometric forms (mostly tapes) and lengths, less manipulability than NbTi, and pinning (current carrying capability in large magnetic fields) which is sub-optimal around 77 K. All of these issues are being addressed in research labs, and it is possible that HTS will one day supersede NbTi in MRI systems.

The human body is mostly fat and water, both containing hydrogen, which comprises ~ 63% of the atoms in the body. Therefore, hydrogen nuclei (protons), which produce a strong NMR signal, are the primary nuclei imaged in MRI.

10.4.2 History of MRI — A General Electric (GE) Perspective

That protons possess a magnetic dipole moment was proposed by Pauli in 1924. The possibility of detecting these moments by NMR was first suggested by Gorter[195] in 1936, and the first successful NMR experiments were done on particle beams moving through a vacuum by Rabi[196] in 1939. In 1946 Purcell[197] at Harvard and Bloch[198] at Stanford were the first to perform NMR in condensed matter (solids or liquids), for which they received the Nobel Prize in Physics in 1952. The possibility of whole-body NMR was suggested by Jackson[199] in 1968. The first images based on proton NMR were obtained by Damadian (using a technique called field-focusing) and by Lauterbur[191] (using the back projection technique used in CT X-ray reconstruction). Lauterbur's introduction of gradient field coils to produce position-dependence in the NMR signal was a crucial innovation. In 1975, Ernst[200] proposed a two-dimensional Fourier transform reconstruction technique using phase and frequency encoding that has become the standard acquisition technique for MRI. In the late 1970s, initial human images using either electromagnets or resistive air core magnets were produced by two

[193] T.W. Redpath, *Br. Jour. Radiology* 71 (1998) 704
[194] http://www.time-medical.com/products_technology_hts.htm
[195] C. J. Gorter, *Physica* 3 (1936) 995
[196] I.I. Rabi et al., *Phys Rev*. 53 (1938) 318
[197] E. M. Prucell et al., *Phys Rev*. 69 (1946) 37
[198] F. Bloch et al., *Phys Rev.* 69 (1946) 127
[199] J. A. Jackson et al., *Rev. Sc. Instrum.* 39 (1968) 510
[200] A. Kumar et al., *J. of Mag. Resonance* 18 (1969) 69

groups at the University of Nottingham, one under Andrew[201], the other under Mansfield[202], and by a group under Mallard[193] at the University of Aberdeen. In 2003, Lauterbur of the University of Illinois and Mansfield of the University of Nottingham were awarded the Nobel Prize in Medicine for their development of MRI.

The first whole body MRI systems were large air-core resistive magnets that required large power supplies and water cooling. Most importantly, these thermal constrainsts limited field strengths to about 0.2 T. This limitation at first did not appear to be particularly significant. In the late 1970s it was commonly believed that human proton MRI would be effective only at frequencies below about 10 MHz due to screening by the human body of the RF fields at higher frequencies[202]. During this period the total worldwide effort on MRI was dwarfed by the development of CT scanning. Near the end of this decade, CT had grown rapidly and was a highly competitive enterprise, as it revolutionized the practice of radiology. After a late start, GE become a major force in the CT marketplace after a 2-year period of R&D at its Central Research Lab in Niskayuna NY. The CT research effort, which had been led by physicist Dr. Rowland Redington, was reduced rapidly as the technology was transferred to GE's imaging business headquartered in Milwaukee, WI. A small group of investigators, including Redington, another physicist, Howard Hart, and a computer scientist, Bill Leue, began to follow MRI developments elsewhere and to formulate some new approaches, but initially there was little or no experimental imaging being done. As part of this work, Richard Likes, who was working at the GE labs while preparing for graduate school, developed some advanced MR imaging concepts, including the introduction of k-space.

In 1978, a physicist, John Schenck, who had temporarily left the company to complete a medical degree, returned to GE and was asked by Redington to investigate the desirability of an expanded MRI effort. Within a few weeks of his return, he attended a 1978 NMR Gordon Conference where a session was devoted to recent work on NMR imaging. This lively session generated intense interest and skepticism about the practicality of MRI. By this time, CT had become a major business facing intense competition, generating significant revenue and numerous technological innovations. In this climate, MRI, with numerous impediments, was viewed as a distraction. One comment was that "MRI is the technique of the future — and probably always will be." Nonetheless, it was decided to make a significant investment to investigate improving the resolution of proton imaging and the possibility of metabolic studies using phosphorus NMR. Permission was obtained to commission a high-field superconducting magnet and to hire two additional staff members. Several possible magnets were considered. A resistive magnet with a (barely) human-size bore and operating at 0.12 T was ordered from the Walker magnet company for initial imaging. It was known that more powerful magnets could be built using superconducting technology, but it was expensive, there were uncertainties about RF field penetration at higher frequencies, and much of the work that had been done on them involved nuclear weapons research and was classified. On the other hand, high fields offered the possibility of improved signal-to-noise ratio, leading to improved imaging resolution, and the ability to detect low concentration metabolites.

In the UK, Oxford Instruments (OI) was in the process of constructing two whole-body MRI superconducting magnets operating at about 0.3 T. These systems were eventually installed at Hammersmith Hospital in London and at University of California, San Francisco (UCSF)/Diasonics facility in San Francisco. The options considered at GE included 0.3-0.5 T systems similar to the Hammersmith and UCSF systems, and medium-bore, high-field magnets that could be used for animal imaging studies. In the midst of a huge snowstorm in the winter of 1980, OI executives visited GE. They said they were confident it was feasible to make a whole-body magnet operating at a field strength on the order of 1.5 to 2 T. Although this increased the cost and risk involved in the magnet acquisition, it also offered the possibility of achieving a leadership position in this new field.

[201] R. Andrew et al., *Phys. Med. Biol.* 22 (1977) 971
[202] P. Mansfield, *J. Phys. C: Solid State Physics* 10 (1977) L55

After considering bids from OI and another company, Intermagnetics General Corporation (IGC), OI was judged to have the edge in technical magnet performance and experience, and in July 1980, OI was awarded the contract for a one-meter clear-bore system to be delivered in 18 months. The agreement was that the magnet would be designed to reach 2 T but only contractually required to operate at 1.5 T. Offers were made to researchers who had been active in MRI developments. Bill Edelstein had been a leading member of Mallard's team at Aberdeen and Paul Bottomley had been a leader in Andrew's team at Nottingham. They joined Redington's team in late summer and early fall of 1980. The group constructed an initial imaging system with a 0.12 T Walker magnet, which was eventually transferred to the University of Pennsylvania for early clinical evaluation. The OI magnet arrived in 1982, and Redington's team assembled an imaging system to operate with it. However, when the magnet was ramped to about 1.6 T, a significant downward drift was evident. The magnet drifted so fast at higher fields that it never reached 2.0 T. However, the drift rate decreased as the field was lowered, and Hart calculated that at 1.5 T he could ramp the shim coil enough to balance the drift for about a day. To prepare for imaging every few days, Hart had to ramp the field to just above 1.5 T, a tedious and scary process that involved inserting the leads and heating up the superconductive switches with the potential risk of quenching the magnet. Late one night, between 3 a.m. and 4 a.m., with John Schenck lying in the magnet on a wooden plank and Hart operating the scanner, a 1.5 T brain image was acquired at 63.4 MHz. To Hart's surprise, he noted that the entire brain was present in the image, and there was no evidence for the hypothesized shielding of the deep tissues by skin-effect processes. Thus, the team at the GE labs became the first in the world to take an MRI image in a 1.5 T MRI whole-body magnet and experimentally dispel the concerns that proton imaging of humans would be severely limited above 10 MHz.

John Schenck presented these imaging results at a conference in Colorado Springs in February 1983 to a group that was a precursor to today's International Society for Medical Imaging (ISMRM) in a talk which received the best paper award. This presentation was somewhat disruptive to the plans of several groups who had pioneered and were planning to commercialize MRI at lower field strengths using resistive magnets. One of the investigators from another group told Schenck that customers would be confused with regard to what field strength and type of magnet would be relevant clinically. Subsequently, the GE imaging business in Milwaukee decided to introduce a clinical 1.5 T scanner which had the effect of freezing the MRI market for about two years. The first GE 1.5 T products, based on magnets purchased from OI, were introduced in 1984, two years after the first images in 1982. The first systems were placed at the University of Pennsylvania, Duke, and UCSF, and these groups rapidly established the clinical utility of MRI using 1.5 T superconducting magnets. Subsequent magnets easily achieved stable operation at 2 T, but by about 1985, 1.5 T scanners had become a standard product in radiology and remained so even in 2010 when on the order of 10,000 of these magnets are in use worldwide. It is ironic that the quirks of a single early magnet, and the ability of its users to obtain sufficient short-term stability to conduct initial imaging studies, played a major role in establishing this standard field strength. The issue of the penetration of RF fields into human subjects is substantially more complex than at first appreciated. It is relatively unimportant at or below 1.5 T. However, whole-body magnets of 3 T (128 MHz), 7 T (300 MHz) and higher, have been introduced into clinical medicine. Often these high-field systems show stronger, rather than attenuated signals from deep-lying tissues.

GE made the decision that magnet technology was a critical technology for MRI, as 80% of the system cost was from the OI magnet. So in 1982, GE developed its first 0.8 T magnet to demonstrate proof of concept with a superconducting magnet team led by Evangelos (Trifon) Laskaris, who had been working on superconducting generators for GE Energy. GE developed the magnet, and CVI developed the cryostat. Once the business decision was made to go to 1.5 T after the successful first images, a program was launched to develop an MRI magnet at 1.5 T in 1983 and was completed in 1984. During the development of the first cryostats, engineers had many challenges with regard to the suspension systems, which could be damaged easily during transport. GE convened a meeting of experts from its research center and its aerospace business, to design a suspension system, allowing

GE to launch a robust MRI product.

Once it had launched its 1.5 T MRI product, GE began to design a variety of MRI products to address a broad and rapidly developing MRI marketplace. It developed technologies for a low-cost MR system called MR Max, a passively-shielded system launched at a meeting of the Radiological Society of North America (RSNA) with a fully-powered MRI on display. The MR Max sold 25 systems at its launch. With the advent of high performance cryocoolers operating at 10 K, the team began looking at conduction-cooled Nb_3Sn magnets.

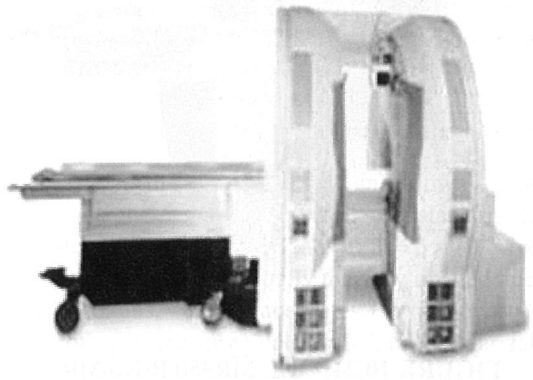

FIGURE 10.21: MRT system magnet.

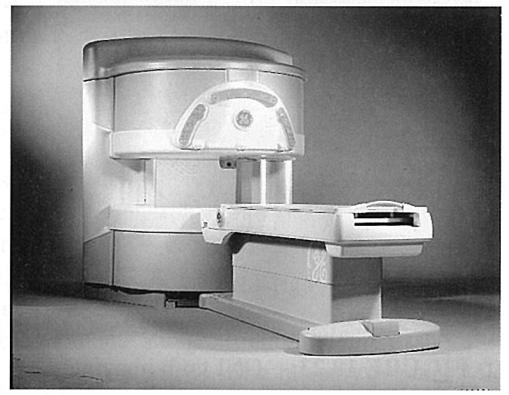

FIGURE 10.22: Openspeed 0.7T MRI System.

The head of MR marketing in the late 1980s asked the team to look at interventional systems. The team then began looking at different MR configurations that could enable surgery and therapies to be done in an MR system. This led to the MRT system, a conduction-cooled Nb_3Sn MR system that consisted of a "double donut" vertical Helmholtz pair — see Figure 10.21. These systems enabled surgery and other therapies to take place in MR systems and led to the development of interventional MR. The installation of the first system took place at the Brigham and Women's (B&W) hospital in Boston in the middle of a huge snowstorm with -20 F temperatures. During the installation, Trifon and Bijan Dorri, who were in Boston to help with the installation, heard a large explosion and were concerned about the magnet. The magnet had been transported from GE's Global Research Center to Boston on an inflatable suspension system. What they soon realized was that the magnet was not damaged, but due to the cold temperatures, the inflatable transport system had become brittle and failed. Despite the transport system issues and the snowstorm, they were able to install the magnet in B&W Hospital, where the system was used for 13 years to save many lives with advanced, image-guided MR surgery. Advances continued in MR technology into the 1990s. Bill Chen identified an emerging cryocooler technology being developed by Sumitomo. He then fostered a partnership between GE and Sumitomo Heavy Industries to develop the first zero boil-off system for MR imaging. This has greatly expanded the MR market into markets where the cost of helium service previously made MR impossible. The technology that enabled MR Max to be a low-cost, passively-shielded system was extended to develop a low-cost actively-shielded 1.5 T MR system. GE introduced the highest-field open MRI system with the introduction of the 0.7 T Openspeed system in 1999 — see Figure 10.22.

In the late 1990s and early 2000s, GE acquired key MR magnet companies Elscint and portions of Magnex. In the early 2000s, GE developed the first whole body 3 T MR system with the acquisition of the technology from Magnex. The mid-2000s saw the introduction of a new type of open system with a 1.5 T 70 cm wide-bore system by Siemens called the Espree and later a 3 T wide-bore system.

GE introduced the first full field-of-view 1.5 T wide-bore system in 2009 with the introduction of the MR450W. GE acquired ONI in 2009, a specialty MR company founded by Peter Roemer, a GE alumnus, that specializes in limb MRI imaging — see Figure 10.23.

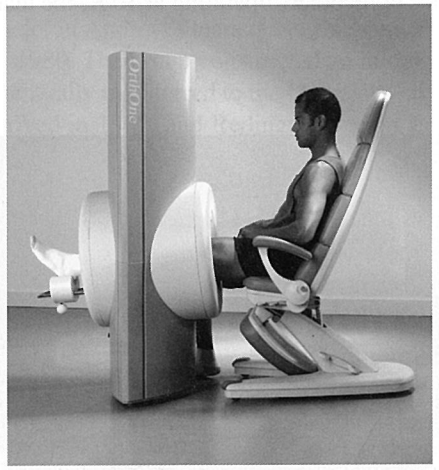

FIGURE 10.23: ONI limb imaging system.

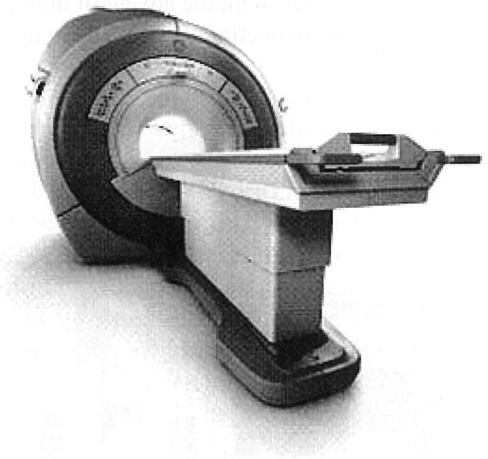

FIGURE 10.24: GE MR350 Brivo MR value system.

Innovations continue in the development of MRI magnets — see Figure 10.24. GE, Siemens, Philips, Toshiba and other MRI companies have begun introducing value systems that address the challenges of making MR cost attractive for emerging markets. Companies around the world are focused on developing MR that can address the clinical needs of both emerging and developed markets and that can help to enable MR become more accessible to thus improve patient care globally.

The Expansion of MRI and Its Effect on Superconductors

MRI has proven to be a rich tool for biological research and medical applications, and its utilization has expanded. Examples are flow imaging (MRI angiography)[203,204], magnetic transfer contrast[205], magnetic resonance elastography (MRE)[206], functional magnetic resonance imaging (fMRI)[207], and magnetic resonance spectroscopy (MRS)[208]. Some of these have led to increased demand on the superconductors used to construct MRI machines and will be discussed further here.

fMRI is used for brain function analysis in humans and animals. The basic premise is that neural activity will cause increased associated metabolic activity and blood flow in the adjacent vessels to feed the activity, and this metabolic activity will increase the use of oxygen from the blood hemoglobin by active neurons. Unoxygenated hemoglobin (deoxyhemoglobin), which is paramagnetic, results from the metabolic loss of oxygen from the hemoglobin, which is diamagnetic. The magnetic fields from the paramagnetic deoxyhemoglobin will affect the MRI signal (especially,

[203] D.G. Nishimura, *Magn. Reson. Med.* 14 (1990) 194.
[204] C.L. Dumoulin et al., *Magn. Reson. Med.* 9 (1989) 139
[205] J. Eng et al., *Magn. Reson. Med.* 17 (1991) 304
[206] T. Wu et al., *Magn. Reson. Med.* 43 (2000) 111
[207] Scott A. Huettel et al., *Functional Magnetic Resonance Imaging*, Sinauer Associates, 2004
[208] G.B. Matson and M.W. Weiner, *Magnetic Resonance Imaging*, D.D. Stark & W.G. Bradley, Jr. Mosby Year Book, St. Louis, (1992) 438

spin-echo T_2 or gradient echo T_2^*), thereby labeling the location of the neural activity in the MRI scan[209]. The study of the location of brain activity using this method (often called BOLD for blood oxygen level dependence fMRI) is now a significant research area and has various medical applications to identify brain pathologies. The association of neural activity with BOLD has been established recently[210]. The MRI signal change is small, however, and this requires MRI base fields (B_0) of 4 T or higher, and the imaging voxel size is usually larger than in a standard image (e.g., 3 mm as opposed to 1 mm) to help compensate for this small signal and get good signal-to-noise (SNR) ratios.

In normal MRI procedures, the ^{1}H nuclei (protons) have their spins polarized in thermal equilibrium in the base field B_0 of the MRI system, usually 1.5 or 3 T. A very small fraction of the spins become polarized in this situation, and the polarization P is given by

$$P = \frac{N^+ - N^-}{N^+ + N^-} = \tanh \frac{\gamma \hbar B_0}{2k_B T}$$

where $N^{+,-}$ is the number of "up" and "down" spins (relative to the applied magnetic field B_0,), γ is the gyromagnetic ratio, $\hbar$ is Planck's constant divided by 2π, k_B is Boltzmann's constant, and T is the absolute temperature. This leads to $P = 5 \times 10^{-6}$ for protons in $B_0 = 1.5$ T at room temperature, and this is why protons are usually the only imaged nuclei, since their abundance in living tissue (water, lipids, proteins, etc.) compensates for the low value of P. A problem arises when one wishes to image other interesting nuclei which have polarizable moments and are found in living tissue, such as ^{13}C, ^{19}F, ^{23}Na, ^{31}P, and ^{15}N, but which are far less dense than ^{1}H. One recently popular MRI technique invented to deal with this problem and requiring additional superconducting magnets is hyperpolarization.It is possible with hyperpolarization[211] to overcome the problems of dealing with some low-volumetric-density nuclei like ^{13}C. At room temperature and 1.5 T, $P(^{13}\text{C}) = 1 \times 10^{-6}$. Hyperpolarization can increase P to near 1, and this hyperpolarization can be maintained at room temperature within useful (in-vivo-compatible) molecules (such as pyruvic acid) long enough to make useful MRI images of ^{13}C, giving new insight into its role in various living tissues and in-vivo processes. Hyperpolarization also can be used with some inert gases, ^{3}He and ^{129}Xe, which are of course not normally found in the body, but can be safely breathed into the lungs to make detailed MRI images of the interior of the lungs, which normally are invisible to MRI since they just contain air. All of these hyperpolarization techniques require a polarizing magnetic field from 0.3 to over 3 T, and these are best made by superconducting magnets quite apart from the MRI imaging system.

When hyperpolarization is not available to enhance signals from the nuclei other than ^{1}H, one is left with 2 methods to make the signal-to noise (SNR) acceptable for imaging: increasing the voxel volume (which makes the image more grainy and less localized), and increasing B_0. Imaging chemical-shift aspects of the various NMR-accessible nuclei in living tissue is often called MRS. One encounters this need for enhanced SNR when one wishes to perform MRS which examines the NMR chemical shifts of ^{1}H in order to distinguish and image the different tissue environments in which ^{1}H is bonded. Dividing the available ^{1}H this way not only lowers the signal available for each chemical shift in a voxel, but the chemical shifts are small and proportional to B_0, again calling for high-field magnets. This need for higher fields has led to creating human-size MRI magnets up to the 10 T range. At this field range, the preferred LTS superconductor of choice switches from NbTi to Nb_3Sn, despite less favorable mechanical properties, in order to increase field capability. Since full-body magnets with this field are expensive and difficult to construct, only a few have been built, and only for research purposes.

[209] S. Ogawa et al., *Proc. Natl. Acad. Sci.* USA 89 (1992) 5951
[210] J. H. Lee et al., *Nat. Lett.* 465 (2010) 788
[211] K Golman et al., *British J. Radiology* 76 (2003) S118

10.5 Ultralow Field NMR and MRI

John Clarke

10.5.1 Introduction

Nuclear magnetic resonance (NMR) and magnetic resonance imaging (MRI) are wonderfully successful technologies. High-field NMR machines are widely used, for example, to determine the structure of new pharmaceutical molecules with exquisite accuracy; Bruker has recently introduced a system operating at 1 GHz in a magnetic field of about 23.5 T. There are perhaps 30,000 MRI machines deployed worldwide[212], capable of imaging most parts of the human body with a spatial resolution of about 1 mm. Probably few patients are aware that they are surrounded by roughly 100 km of NbTi wire wound in a persistent-current solenoid and immersed in about 1000 L of liquid helium! The majority of MRI machines operate at a magnetic field of 1.5 T but there is an increasing use of 3-T machines. MRI machines are expensive, however, roughly $2 M for a 1.5-T system, have a large footprint, and are heavy: it is not unknown for the cost of reinforcing the building to exceed the cost of the machine.

Despite the trend to higher fields, in this section I take a contrarian approach and discuss what would happen if we tried to image at much lower fields. Would it be possible to image in fields, say, four orders of magnitude lower? If so, would the images be better in some way?

10.5.2 Background

MRI[213] is based on NMR[214,215], almost always of protons, which have magnetic moment μ_p and spin 1/2. In the presence of an applied magnetic field B_0, the protons align either parallel or antiparallel to B_0, the energy level splitting being given (in angular frequency units) by the Larmor frequency $\omega = \gamma B_0$; γ is the gyromagnetic ratio. The NMR frequency is 42.58 MHz/T. The magnetic moment of N protons is $M_0 = N\mu_p^2 B_0/k_B T$ in the limit $\mu_p B_0 \ll k_B T$ (Curie Law). At room temperature and in achievable magnetic fields, the magnetic moment is very small. For example, for $B_0 = 1$ T and $T = 300$ K, $M_0/N\mu_p = \mu_p B_0/k_B T \simeq 3.6\times10^{-6}$.

In NMR, M_0 is initially in thermal equilibrium, aligned with B_0 along the z-axis. The application of a "$\pi/2$ pulse" along the x-axis at the Larmor frequency tips M_0 into the x-y plane in which it precesses about the z-axis at frequency $\omega_0/2\pi$. During this precession, M_0 undergoes two relaxation processes. First, it relaxes its direction towards the z-axis, where it eventually regains thermal equilibrium in a characteristic longitudinal (spin-lattice) relaxation time T_1. Second, individual spins dephase via local field fluctuations produced at each site by neighboring spins in the transverse (spin-spin) relaxation time T_2. In water at room temperature, T_1 and T_2 are about 1 s; $T_1 \geq T_2$ always. The full-width at half-maximum (FWHM) linewidth of the NMR line is $\Delta f = 1/\pi T_2$ ("homogeneous broadening"). Inhomogeneities in the magnetic field, however, can substantially broaden the linewidth ("inhomogeneous broadening"), and reduce T_2 to a value T_2^* given by $1/T_2^* = 1/T_2 + 1/T_2'$; T_2' is the inhomogeneous lifetime. The very important spin echo technique invented by Erwin Hahn[216] — used in virtually all NMR and MRI pulse sequences — eliminates inhomogeneous broadening but not homogeneous broadening. In MRI, one uses NMR to determine spatial structure by means of three orthogonal magnetic field gradients that define the magnetic field B_0 in a small volume or "voxel". Gradient switching translates the voxel through the patient to construct the magnetic resonance image of a specified region.

[212] See *Section* 10.4

[213] E.M. Haacke, et al., *Magnetic Resonance Imaging: Physical Principles and Sequence Design.* Wiley & Sons, New York, 1999

[214] A. Abragam, *The Principles of Nuclear Magnetism.* Clarendon Press, Oxford, 1961

[215] C.P. Slichter, *Principles of Magnetic Resonance*, 3rd ed. (Springer, New York, 1989)

10.5.3 Why ULF NMR and MRI?

Given the success of high-field MRI, why would one consider ultralow-field (ULF) imaging? Part of the answer relies on the very low magnetic field noise of detectors based on the SQUID (Superconducting QUantum Interference Device)[217] and the fact that it responds to magnetic flux rather than the rate of change of magnetic flux. As a result, the response of the SQUID to an oscillating magnetic field is frequency independent. In conventional NMR the oscillating magnetic signal induces a voltage across an inductor shunted with a capacitor to form a resonant circuit. The voltage across the tank circuit, by Faraday's Law, scales as $\omega_0 M_0$, that is, as B_0^2. Thus, at first sight, reducing B_0 would seem to be exactly the wrong thing to do. Two factors counter this thinking. First, consider replacing the tank circuit with a SQUID-based detector. Its frequency independent sensitivity eliminates one factor of B_0 in the response, so that the output voltage scales as B_0 rather than B_0^2. Second, one can prepolarize[218] the spins in a magnetic field B_p much greater than B_0. After B_p has been turned off, the spins retain a corresponding magnetic moment $M_p \gg M_0$ that decays in a time T_1, so that, although the spins precess at frequency $\gamma B_0/2\pi$, they produce a signal amplitude proportional to B_p. Thus, the amplitude of the SQUID-detected NMR signal becomes independent of B_0; one can choose B_0 at will provided $B_0 \ll B_p$.

There is an immediate advantage of low-field NMR and MRI. For a given inhomogeneity ΔB_0 and a fixed relative inhomogeneity $\Delta B_0/B_0$, the inhomogeneous linewidth $\Delta f'$ scales as $(\Delta B_0/B_0)B_0$, that is, as B_0. Thus, narrow linewidths—and high spatial resolution—can be achieved in relatively inhomogeneous fields. For example, to obtain a 1-Hz linewidth in a 1-GHz NMR system, it is necessary to shim the magnetic field homogeneity to 1 part in 10^9 over the volume of the sample. Although achievable, this is challenging. Furthermore, spatial variations in magnetic susceptibility within a sample produce linewidth broadening—and a loss of spatial resolution in MRI—that cannot be compensated. In contrast, at an NMR frequency of 2 kHz (for protons, corresponding roughly to the Earth's field), the field homogeneity required for a 1-Hz linewidth is only 1 part in 2,000, which is easily obtainable; in addition, the effects of susceptibility variation are negligible.

10.5.4 Ultralow Field NMR

In 2001, in a collaboration with Erwin Hahn and Alex Pines, Robert McDermott—then a graduate student in my group—built a SQUID-based system for experiments on low-field NMR and NQR (nuclear quadrupole resonance). The essence of the system is shown in Figure 10.25. The magnetic flux signal is detected by a dc-SQUID—two Josephson junctions connected in parallel on a superconducting loop[217]. The SQUID—cooled in liquid helium to 4.2 K—is current-biased in the voltage state, and the voltage is periodic in the applied magnetic flux with a period of one flux quantum, Φ_0. The flux in the SQUID is kept constant by means of a current fed back into a coil by a flux-locked loop (not shown). Typically, the flux noise is on the order of $10^{-6}\Phi_0$ Hz$^{-1/2}$. The superconducting input coil on the SQUID washer[219] is coupled to a superconducting flux transformer configured as

[216] E.L. Hahn, *Phys. Rev.* 80 (1950) 580

[217] See Chapter 5 "SQUIDs and Detectors"

[218] M. Packard and R. Varian, *Phys. Rev.* 93 (1954) 941

[219] See Chapter 5, Figure 5.13(b)

a first-derivative, axial gradiometer. When a magnetic flux is applied to the lower pickup loop of the gradiometer, a current is induced in the transformer that in turn induces a magnetic flux in the SQUID. Both the transformer and SQUID respond at arbitrarily low frequencies. Ideally, the gradiometer is insensitive to uniform magnetic field fluctuations, and thus attenuates external magnetic field noise. As indicated in Figure 10.25, room-temperature access enables one to maintain samples at room temperature. Michael Mück at the University of Giessen fabricated the low-noise SQUID.

Our thinking of what to do with our new system, however, was diverted by the arrival of Andreas Trabesinger as a postdoctoral scholar with Alex Pines. Andreas became intrigued with the notion of NMR in liquids at very low fields, and we set up an experiment to study the NMR of protons in mineral oil[220]. We placed the sample, maintained near room temperature, in the lower loop of the first-derivative gradiometer. Separate coils supplied B_p, an oscillating field to tip the spins through $\pi/2$, and B_0—which was deliberately made relatively inhomogeneous. Figure 10.26(a) shows the results of a conventional spin echo measurement with B_0 = 1.8 mT. The signal-to-noise ratio is poor, despite the 10,000 averages, and the linewidth is broad, about 1 kHz. In contrast, the spectrum in Figure 10.26(b) was obtained at 1.8 μT following prepolarization of the spins at 1.8 mT. To obtain this spectrum, B_p was turned off nonadiabatically (in a time short compared with the NMR period) so that the spins precessed about B_0. After a time τ, we reversed the direction of B_0, producing a spin echo at 2τ. As expected, the linewidth was reduced by a factor of 1,000, and, even with only 100 averages, the signal-to-noise ratio of the spectrum was greatly increased. This result vividly illustrates the increase in signal amplitude and reduction in linewidth one can achieve by reducing the magnetic field for a given relative inhomogeneity.

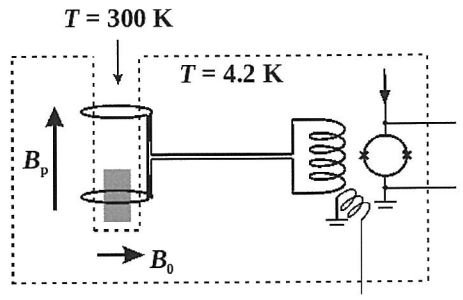

FIGURE 10.25: Configuration of ULF NMR system. The sample, which is nominally at room temperature, is lowered into the lower loop of a superconducting, first-derivative gradiometer inductively coupled to a dc SQUID operated in a flux-locked loop. The directions of the polarizing field B_p and Larmor field B_0 are indicated.

10.5.5 Ultralow Field MRI

Our next step was to apply our ULF NMR methodology to the rather more complicated technique of ULF MRI. Robert constructed an MRI system[221,222,223] made from wood with copper wire coils and assembled the required electronics. The wooden cube, 1.8 m on a side, supports two pairs of coils that cancel the Earth's magnetic field in the vertical (x) direction and one horizontal (y) direction. A Helmholtz pair provides a horizontal measurement field in the z-direction that adds to the z-component of the Earth's field to produce a field of 132 μT at the center of the cube. The corresponding Larmor frequency for protons is 5.6 kHz. The cube also supports three sets of coils that produce the gradients $G_z = \partial B_z/\partial z$, $G_x = \partial B_z/\partial x$ and $G_y = \partial B_z/\partial y$, typically 200 μT/m. A copper-wire coil, placed immediately below the sample, produces a polarizing field in the x-direction, and a Helmholz pair produces the $\pi/2$ and π pulses required to create a spin echo. The NMR signal is

[220] R. McDermott et al., *Science* 295 (2002) 2247
[221] R. McDermott et al., *Proc. Natl. Acad. Sci* 101 (2004) 7857
[222] R. McDermott et al., *J. Low Temp. Phys.* 135 (2004) 793
[223] J. Clarke et al., *Annu. Rev. Biomed. Eng.* 9 (2007) 389

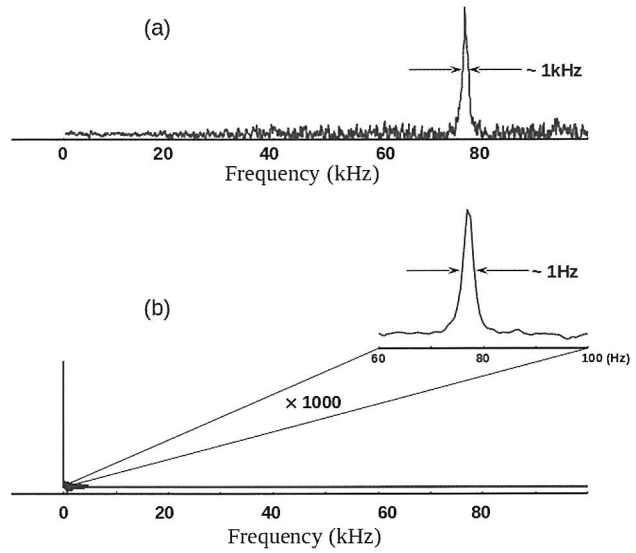

FIGURE 10.26: NMR spectra of 5 mL of mineral oil obtained with the circuit shown in Figure 10.25. (a) Spectrum obtained using a conventional Hahn spin echo with B_0 = 1.8 mT and 10,000 acquisitions. The linewidth is about 1 kHz. (b) Spectrum obtained with B_p = 1.8 mT and B_0 = 1.8 μT using 100 acquisitions. The linewidth is about 1 Hz, and the signal-to-noise ratio is greatly improved compared to that in (a).

detected by a second-derivative gradiometer contained in a fiberglass dewar mounted immediately above the sample. The dewar, built by Robert, has very low magnetic noise, following the design of Seton et al.[224] Instead of the traditional aluminized mylar, the superinsulation consists of aluminized polyester cloth. The finely divided aluminum coating reflects well in the infrared, thus giving a low liquid helium boil-off, while producing much lower magnetic noise generated by Nyquist noise currents. An important feature is an array of 25 Josephson tunnel junctions in series with the gradiometer and the input coil of the SQUID. These junctions switch rapidly to the voltage state to protect the SQUID from the large currents that would otherwise be induced when the various fields are pulsed. Once the fields stabilize, the junctions rapidly revert to the superconducting state, enabling us to acquire the data. The magnetic field noise referred to the lowest loop of the gradiometer is typically 1 fTHz$^{-1/2}$. Later, Robert and Bennie ten Haken, who was on leave from the University of Twente in The Netherlands, surrounded the entire system with a 3-mm thick aluminum shield to reduce both radiofrequency interference and 5.6-kHz magnetic field noise.

To obtain 3-D images, we proceed as follows. The measurement field, B_0 = 132 μT, is applied in the z-direction throughout the image acquisition. The pulse sequence begins with the application of the polarizing field along the x-axis for a time several times longer than T_1, so that the proton spins are fully polarized. This field is turned off adiabatically (in a time longer than the NMR period) so that the spins reorient to align with B_0, retaining their initial polarization. Subsequently, a $\pi/2$ pulse at the 5.6-kHz Larmor frequency is applied along the x-axis, causing the spins to precess about the z-axis. Shortly after, the frequency encoding and phase encoding gradients are switched on; these persist until the π pulse is applied to form the spin echo. In the x-direction, the image is frequency encoded, that is, a gradient G_x produces a frequency variation $\omega = \gamma(B_0 + xG_x)$. In the

[224] H.C. Seton et al., *Cryogenics* 45 (2005) 348

y- and z-directions, the image is phase encoded: gradient pulses G_y and G_z produce phase changes $\Delta\phi(z) = \gamma z G_y \tau$ and $\Delta\phi(y) = \gamma y G_z \tau$, respectively. Each complete pulse sequence involves one value of G_x and one value of G_y. The SQUID electronics is enabled shortly after the π pulse is complete, so that it is not saturated when the magnetic fields are switched. The data are subsequently decoded to reconstruct the image. The entire sequence is repeated as necessary to improve the signal-to-noise ratio.

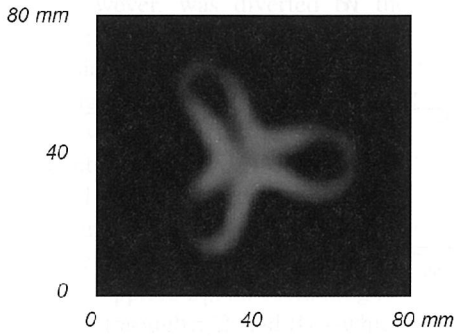

FIGURE 10.27: Image of red pepper slice obtained at 132 μT.

Our first 2-D image was of a pepper slice, shown in Figure 10.27. Notice that the outer edges of the pepper fade out—this is because of the somewhat restricted field of view set by the diameter of the superconducting pickup loop. Subsequent images of "phantoms" demonstrated an in-plane resolution of better than 1 mm in an acquisition time of a few minutes. In one set of experiments we placed a titanium rod on top of the phantom[225]. In high field, the magnetic susceptibility of the rod introduced a substantial distortion of the local magnetic field, and hence of the image of the phantom. In ULF, however, the distortion was unobservable. This result is entirely expected from the earlier discussion showing that linewidth broadening scales as B_0 for a given relative inhomogeneity $\Delta B_0/B_0$. Thus, another potential advantage of ULF MRI is its ability to obtain undistorted images in the vicinity of, say, a titanium screw.

Michael Mößle, a postdoctoral scholar from Tübingen, Germany, joined the group, and we set about obtaining 3-D images in vivo. Figure 10.28a shows Michael's arm being imaged[226], and the resulting images are shown in Figure 10.28b. Each of the six slices is 10 mm thick, the in-plane resolution is about 2 mm and the total acquisition time was 6 minutes. The two small white dots in each image represent bone marrow, and the black annuli around them are bone. The narrow white region on the underside of each slice arises from a fat layer. The white regions are prominent because T_1 is relatively long in fatty tissue. The arm muscle is poorly defined. This is because its T_1 is short, typically 40 ms, so that the signal amplitude diminishes significantly during the imaging sequence. As we shall see, differences in T_1 turn out to be a major strength of ULF MRI.

10.5.6 T_1-weighted Contrast Imaging

An important issue in MRI is distinguishing different tissue types, e.g., healthy and cancerous tissues, even though the proton densities may be identical. In high-field MRI this distinction can, in principle, be made using the fact that T_1 differs in different tissue types so that one can resolve them by weighting the image with T_1. In practice, this technique is not always successful. For example, to image a breast tumor it is necessary to inject a contrast agent—usually a Gd salt–into the bloodstream. The blood tends to flow preferentially to the tumor, where the paramagnetic Gd ions increase the NMR relaxation rate, shortening T_1. However, this technique tends to produce a high rate of false positives. On the other hand, it is known that T_1 contrast can be significantly

[225] M. Mößle et al., *J. Magn. Reson.* 179 (2006) 146

[226] Our protocol was approved by both the environmental health and safety and the human subjects committees.

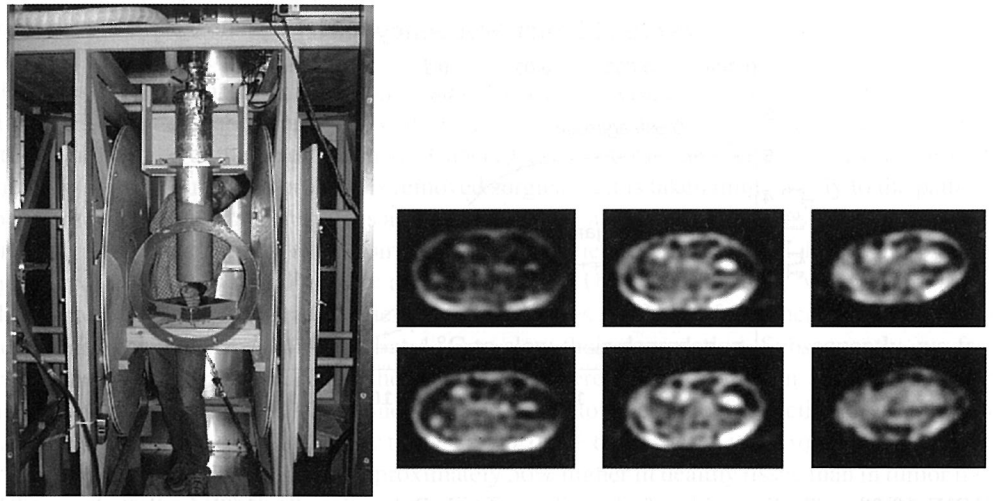

FIGURE 10.28: (a) Imaging Michael Mößle's arm. Fiberglass dewar containing the SQUID and gradiometer is suspended immediately above his arm. Polarizing coil is below his arm, blue coil is one of the Helmholtz pair of coils that provides $\pi/2$ and π pulses. The innermost pair of larger coils with axis in the z-plane provides B_0; outside these are the biplanar coils that provide $\partial B_z/\partial x$ and $\partial B_z/\partial y$ and the Maxwell pair that provides $\partial B_z/\partial z$. (b) Six arm slices acquired with the system shown in (a). Slice thickness 10 mm, B_0 = 132 μT, field gradients 150 μT/m, in-plane resolution ~ 2 mm, acquisition time 6 min.

enhanced in low fields[227], and ULF MRI is readily adapted to this modality.

SeungKyun Lee , Whit Myers and Nathan Kelso joined our project to develop ULF T_1-weighted contrast imaging[228]. The essence of the technique is as follows. Suppose two regions, A and B, have relaxation times T_{1A} and T_{1B}, with $T_{1A} > T_{1B}$. After polarizing the proton spins fully in a polarizing field B_p, we reduce B_p adiabatically to an intermediate value B_{pi}. Following a delay of a few tens of milliseconds during which the spins decay toward equilibrium at different rates in the field $(B_{pi}^2 + B_0^2)^{1/2}$, we reduce B_{pi} adiabatically to zero and apply the imaging sequence in the field B_0. The image of region A will be brighter than that of region B since the magnetization at the beginning of the imaging sequence is higher. To illustrate this principle, we studied samples with 0.25% and 0.5% concentrations of agarose gel in water; this jelly-like substance is often used to replicate tissue in MRI phantoms. Figure 10.29 shows the variation of the relaxation rate $1/T_1$ versus the intermediate magnetic field and Larmor frequency in which the spins were allowed to relax; for reference, we have included the relaxation rate of protons in water. We see immediately that, while $1/T_1$ in water remains constant, in the two gel solutions the rates are almost identical at high field (above about 30 mT), whereas below about 500 μT the T_1 value for the 0.25% concentration is a factor of two longer than for the 0.50% concentration. This plot shows graphically the enhancement in T_1 contrast at ultralow fields.

As a further illustration of the enhanced T_1-weighted contrast achievable at low fields, Figure 10.30(a) shows a phantom consisting of a tube of 0.5% agarose gel containing nine plastic straws filled with water. The inner diameter of the tubes ranges from 1 mm to 6 mm. Figure 10.30(b) shows

[227] S.H. Koenig and R.D. Brown, III in R.K. Gupta (ed.) *NMR Spectroscopy of Cells and Organisms* Vol. II (CRC Press, Boca Raton, Florida, 1987) p. 75

[228] S-K. Lee et al., *Magn. Reson. Med.* 53 (2005) 9

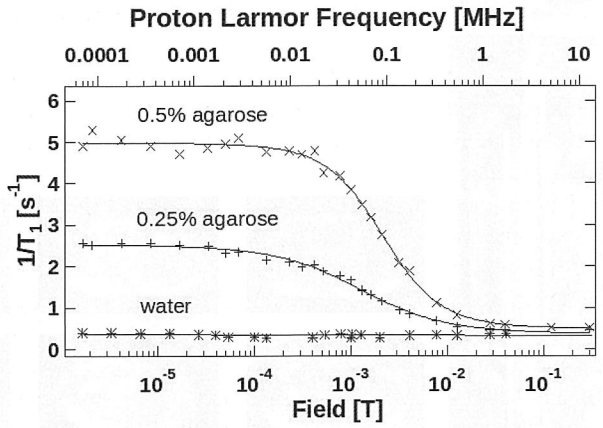

FIGURE 10.29: T_1 dispersion of water agarose gel. Relaxation rate $1/T_1$ is plotted versus B_0 (lower abscissa) and Lamor frequency (upper abscissa).

an image of the phantom acquired with an intermediate field of 100 mT where the T_1 values of water and gel are approximately 1.6 s and 1.5 s, respectively. The largest of the water columns is barely distinguished. In contrast, in the image acquired—see Figure 10.30(c)—with an intermediate field of 132 μT where T_1 is reduced to 0.3 s for gel and is unchanged for water, the contrast is stark: all nine straws are clearly visible. These results indicate the potential of T_1-weighted contrast imaging at low fields for distinguishing different tissue types in the human body.

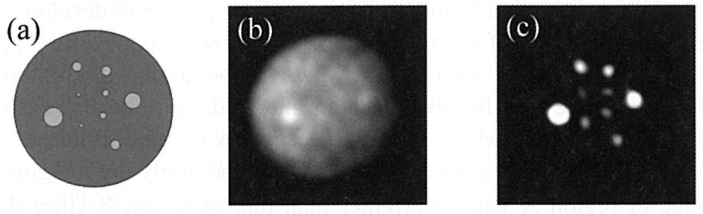

FIGURE 10.30: MRI of phantom at different fields. (a) Phantom consists of column of 0.5% agarose gel in water with 9 plastic straws containing water with diameters ranging from 1-6 mm. (b) T_1-weighted contrast image at 100 mT. (c) T_1-weighted contrast image at 132 μT.

10.5.7 T_1 Contrast in Ex Vivo Prostate Tissue

Prostate cancer is generally diagnosed by means of a PSA (prostate specific antigen) test or a digital rectal examination. Imaging the extent of the cancer is, unfortunately, extremely difficult: in particular, high-field MRI—with or without a contrast agent—is unable to distinguish cancerous and healthy tissues by means of T_1 contrast. Treatment of the disease poses a dilemma because of the wide range of malignancy, and is usually based on biopsy. Treatments include "active surveillance", surgery, radiation therapy and cryosurgery. Thus, reliable, cost-effective imaging would greatly benefit the diagnosis of prostate cancer. In fact, there are MRI-based techniques that can image prostate

cancer[229], but these techniques require a 3-T system, and their complexity unfortunately results in a cost that is too high for routine clinical use.

For these reasons, and encouraged by our ULF MRI results on T_1-contrast, Sarah Busch and Michael Hatridge embarked on a study of ex vivo prostate tissue[230]. This study is in collaboration with Dr. Jeff Simko at the Comprehensive Cancer Care Center at the University of California, San Francisco. After a cancerous prostate is removed surgically, it is taken immediately to the pathology laboratory where two small specimens are excised. One is judged (by expert visual inspection) to be nominally cancerous and the other nominally healthy. The specimens are enclosed in a biohazard bag, placed on ice, rushed to Berkeley and placed in our ULF MRI machine. We measure their T_1 values simultaneously in a gradient field which separates the NMR frequencies of the two specimens. The specimens are maintained at 4 °C to slow their degradation. Subsequently, we freeze the specimens on dry ice and return them to UCSF, where they are formalin fixed, sectioned and stained. Jeff examines the thin slices under a microscope to determine the fraction of tumor cells.

Although the values of T_1 in healthy tissue and in 100% tumor tissue vary from patient to patient, for a given patient we find that T_1 is approximately 50% higher in healthy tissue than in tumor tissue. Furthermore, we find that the "image contrast" $(T_{1A} - T_{1B})/T_{1A}$ scales approximately linearly with $(\%\text{tumor})_B - (\%\text{tumor})_A$; T_{1A} and T_{1B} ($T_{1A} > T_{1B}$) are the relaxation times of two tissue specimens A and B from the same patient, where A contains less tumor than B.

In separate experiments, we obtained "T_1 maps" of several larger specimens on which Jeff subsequently performed the histology. As expected from the measurements of T_1 in the small specimens, the maximum image contrast was about 1/3.

These ex vivo results suggest that microtesla MRI with T_1 contrast may be a viable technique for in vivo imaging of prostate cancer. Only in vivo studies, however, can determine the spatial resolution, sensitivity and specificity. We simply do not know how measurements of T_1 made on tissue specimens a few hours after surgery and cooled to 4 °C relate to in vivo values of T_1. If, indeed, the method proves successful in imaging prostate cancer with reasonable resolution—say 2 mm—what might its role be? One application would be in assessing the severity of the disease following the initial diagnosis, e.g., as an intermediate step between initial diagnosis and biopsy. ULF MRI could provide a reference image to guide subsequent biopsy. Because of its potentially low cost per image, it could be used routinely to monitor the progression of prostate cancer during active surveillance or radiation therapy. Since radiation therapy involves the accurate placement of metallic radioactive seeds, ULF MRI—with its insensitivity to the presence of metallic objects—could be used to monitor the insertion of the seeds with the aid of a previously acquired reference image. A broader issue concerns the applicability of ULF MRI to imaging other cancers, for example, breast or brain tumors.

10.5.8 Research in Other Institutions

Numerous other groups have established research programs on microtesla NMR and MRI, and I give a few examples. Qiu et al.[231] measured a proton linewidth of 0.034 Hz in benzene in the Earth's field using a high-T_c SQUID, and Bernarding et al.[232] a linewidth of 0.34 Hz in a J-coupling spectrum. Volegov and coworkers[233] made simultaneous measurements of a somatosensory response and microtesla NMR from the brain — no claim was made that the two are correlated. Zotev et al.[234]

[229] J. Kurhanewicz et al., *Curr. Opin. Urol.* 18 (2008) 71
[230] S. Busch, M. Hatridge, M. Mößle, W. Myers, T. Wong, M. Mück, K. Chew, J. Simko, A. Pines and J. Clarke *(unpublished)
[231] L. Qiu et al., *Appl. Phys. Lett.* 91 (2007) 072505
[232] J. Bernarding et al., *J. Am. Chem. Soc.* 128 (2006) 714
[233] P. Volegov et al., *Magn. Reson. Med.* 52 (2004) 467
[234] V.S. Zotev et al., *J. Magn. Reson.* 194 (2008) 115

used a 7-channel SQUID system to acquire 3-D images of the brain at 46 μT using a polarizing field of 30 mT.

On the technical front, a European-Union consortium involving a dozen institutions and led by Aalto University in Helsinki, Finland, is focused on combining microtesla MRI with a 300-channel system for magnetoencephalography (MEG). Such a system would allow one to perform MRI and MEG with the same system, eliminating co-registration problems and potentially reducing costs. The use of 300-SQUID gradiometers to acquire the same NMR signal could greatly increase the signal-to-noise ratio. Inseob Hahn and coworkers[235] at the Jet Propulsion Laboratory/Caltech and the University of California, Los Angeles have developed a SQUID MRI system involving a cryocooler that runs continuously and achieves a temperature of 3.5 K. In preliminary experiments on a phantom, using an imaging frequency of 5.7 kHz and a polarizing field of 10 mT, they achieved an in-plane resolution of 3.5 mm × 3.5 mm. This is a significant step towards implementing clinical systems. Alternative magnetic field sensors are being investigated. Savukov et al.[236] at Los Alamos National Laboratory used an atomic magnetometer with a magnetic field noise of 12 fTHz$^{-1/2}$ to image a phantom. Myriam Pannetier, Claude Fermon and coworkers[237] at Saclay, France are developing a "mixed sensor"—a thin-film loop of YBCO coupled to a giant magnetoresistance (GMR) detector. They have achieved a magnetic field noise of a few fTHz$^{-1/2}$ at frequencies f above the $1/f$ noise, and imaged water phantoms.

10.5.9 A Perspective

We have seen that it is possible to obtain MR images in magnetic fields four orders of magnitude lower than in clinical MRI machines, and yes, ULF MRI does have a distinct advantage in terms of enhanced T_1 contrast. But what would it take to develop a ULF MRI machine that would have some impact on clinically-important imaging?

First of all, it should be realized that ULF MRI will never compete with high-field MRI in terms of the combination of speed and spatial resolution. Furthermore, high-field MRI has the great advantage that one can place an appropriately-shaped, room-temperature pickup coil over or around any part of the human body to obtain an image. In this respect, the use of a cryogenic detector is restrictive. In addition, the field of view of a single detector is limited to a few centimeters, although the use of multiple detectors—already very well developed for 300-channel, whole-head systems for MEG—would overcome this problem.

The major hurdle in developing a useful ULF MRI system is to improve the signal-to-noise-ratio. To achieve a given spatial resolution, the required imaging time scales as $S_B(f_0)/B_p^2$, where $S_B(f_0)$ is the spectral density of the magnetic field noise of the detector at the Larmor frequency. This scaling factor has tremendous leverage. Currently, the best SQUID-based detectors used in our ULF MRI system have a noise of about 0.5 fTHz$^{-1/2}$. However, in our experience, this noise level is generally increased by radiofrequency interference coupled in via various leads and by noise at the Larmor frequency resulting from an imperfectly balanced gradiometer. With improved rejection of these parasitic noise sources and the use of a lower noise SQUID, I believe it is possible to achieve a noise as low as 0.2 fTHz$^{-1/2}$ or conceivably 0.1 fTHz$^{-1/2}$—roughly the noise produced by Nyquist noise currents in the human body at about 5 kHz. Evidently, an order-of-magnitude reduction in the noise would decrease the imaging time by two orders of magnitude.

Similarly, one must accept the fact that higher polarizing fields are going to be a way of life. We have recently implemented a 150-mT water-cooled polarizing coil, kindly donated by Steve Conolly at UC Berkeley. The coil, consisting of 240 turns of 4 mm × 4 mm copper tube, has an

[235] I. Hahn et al. (unpublished)

[236] L.M. Savukov et al., *J. Magn. Reson.* 199 (2009) 188

[237] M. Pannetier et al., *Science* 304 (2004) 1648

outer diameter of 400 mm and a mass of 31 kg. A 20-kW power supply is required to supply the 200-A current pulse that produces the 150-mT field in the center of the coil. The use of such a coil leads to some challenges, the most serious of which are the eddy currents produced in the aluminum shield when the field is ramped down and the need to make the coil utterly safe for human subjects. Both difficulties have recently been overcome.

I believe there is significant potential to develop a practical, relatively inexpensive, clinically useful ULF MRI system with an initial focus on imaging cancer. As always with new technologies, realizing such a system will require major investments of time and money in science and engineering.

10.6 Superconductivity in Medical Accelerators for Cancer Therapy

Peter A. Zavodszky

In the developed world cancer is the second leading cause of death. During 1990–2006 the cancer mortality rate in the USA decreased from the peak value of 215 to 175 (per 100,000 population), mainly due to earlier detection and better treatment methods. About 50% of cancer patients receive some form of radiotherapy. The success rate of this method of treatment is second only to that for surgery in the case of localized tumors.

Ideally, radiation should kill only the cancerous cells and spare the surrounding healthy tissue. In reality, there is no such radiation treatment, and the total maximum dose deliverable to the tumor is determined by the radiation tolerance of the surrounding area. Over the past 100 years great effort was made to increase the precision of the irradiation to minimize the chance of inducing negative effects (secondary cancers) in the surrounding area of the tumor. Today 90% of radiation therapy involves high energy Bremsstrahlung radiation from electron linear accelerators. This has replaced low energy X-ray sources and ^{60}Co gamma ray sources because of a better depth-dose distribution. Utilizing multi-leaf collimators, intensity modulation and multiple irradiation directions, modern treatment facilities can achieve significantly better dose distribution, and, consequently, better clinical results.

Particle accelerators played an important role in fighting cancer since their invention. John Lawrence and Robert Stone began clinical trials in 1938 to treat cancer with neutrons produced using protons accelerated with the 37-inch cyclotron at the Radiation Laboratory at the University of California, Berkeley[238]. This was the origin of a different mode to use radiation with increased biological effectiveness. Photons have low linear energy transfer, primarily breaking one strand of DNA, which can be repaired by the damaged cell. In contrast, neutrons interact primarily through nuclear reactions, breaking both strands in the DNA helix, which can not be repaired.

It was in 1946 that Robert R. Wilson realized that charged heavy particles, such as protons or carbon ions, have superior characteristics, which make them more suitable than photons or neutrons to kill deep-seated tumors. In his seminal paper[239] he showed that protons and ions lose 85% of their energy near the end of their range, making them suitable to spare healthy tissue surrounding the tumor and killing only cells that are located at the end of that range in the human body. This increase in ionization density had been measured in 1903 for alpha particles by Sir William Bragg and is known as the Bragg profile. Figure 10.31 compares the relative dose at different depths of water—the human body contains mainly water—deposited by 18 MeV photons, 135 MeV protons,

[238] J. L. Heilbron and R. W. Seidel, *Lawrence and His Laboratory: A History of the Lawrence Berkeley Laboratory*, Volume I. Berkeley: University of California Press, (1989)

[239] R. R. Wilson, *Radiology* 47 (1946) 487

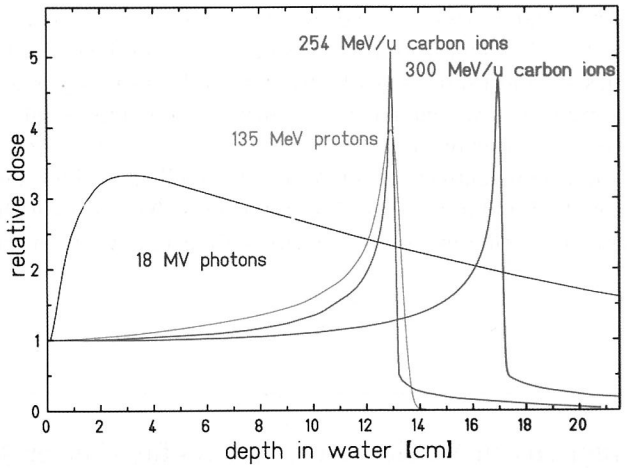

FIGURE 10.31: Comparison of the depth-dose distribution of (conventionally used) photons, protons and carbon ions. With photons the dose decreases exponentially with increasing depth, i.e., the dose in the target volume of deep-seated tumors is smaller than the dose delivered to the healthy tissue above it. Protons and carbon ions exhibit an inverse dose profile, i.e., the dose increases with increasing penetration depth. This profile can be shifted by energy variation over the target volume, leading to a much higher dose deposition inside the tumor than outside in the healthy tissue (see G. Kraft, *Prog. Part. Nucl. Phys.* 45 (2000) S473).

254 and 300 MeV/u ^{12}C ions. By adjusting the energy of the ions, the location of the damage caused by the energy deposition can be controlled with high precision.

The first direct use of ions in cancer treatment took place at the Radiation Laboratory at Berkeley in 1952. Cornelius Tobias and John Lawrence used the 184-inch synchrocyclotron to accelerate deuterium and helium ions to several hundred MeV/u energies, beginning a new era in fighting cancer[240].

The completion of the Bevalac, an accelerator complex formed from a 6 GeV synchrotron (Bevatron), and the SuperHILAC (Heavy Ion Linac) led to a major program of clinical trials to treat human cancer using light ion beams (^{4}He to ^{28}Si with ^{20}Ne most commonly used). From 1977 to 1992 (when the Bevalac became inactive, about 700 patients were treated with ^{4}He ions and about 300 patients, with ^{20}Ne ion beams[241].

Soon after the invention of the cyclotron by Ernest O. Lawrence[242], these accelerators played a crucial role in a variety of biological, medical and industrial applications. The final energy (T) of a given ion with charge $Q = Ze$ and mass Am_0 accelerated in a cyclotron of radius (r) and magnetic field (B) can be calculated with the following simple formula:

$$T = \frac{Q^2}{A}\frac{e^2}{2m_0}r^2B^2.$$

This shows that for a particular type of charged particle and final energy, a cyclotron can be more compact if the operating magnetic field is stronger. However, the maximum field attainable with room temperature magnets is typically less than 2 tesla. Fraser and colleagues at Chalk River Nuclear Laboratories proposed that by using superconducting magnets to exceed 3 T, one can reduce

[240] C.A. Tobias, H.O. Anger, J.H. Lawrence, *Am. J. Roentgenol., Radium Ther., and Nucl. Med.* 67(1) (1952) 1
[241] W.T. Chu, *Proc. of the 1st Int. Conf. on Particle Accelerators*, Kyoto (2010) 21
[242] E.O Lawrence and N.E. Edlefsen, *Science* 72 (1930) 376

the size and the cost of the cyclotron significantly[243].

Although the initial treatments using neutrons produced poor results, later Mary Catterall[244] obtained encouraging results treating cancer patients with fast neutrons produced in the Medical Research Council Cyclotron Facility at Hammersmith Hospital in London, UK. The National Cancer Institute in the USA in 1979 initiated a 10-year program to design, develop and build hospital-based neutron therapy machines, and to conduct phase III clinical trials[245]. These machines were all room-temperature, magnet-based cyclotrons producing neutrons via the bombardment of a beryllium target with high energy protons ($E_p > 42$ MeV). The use of isocentric gantries allowed irradiations from several directions, spreading the unwanted dose to a larger tissue volume. Neutrons could be produced more easily with deuterium projectiles, due to the larger production cross section, but the size of the cyclotron and gantry capable of producing sufficiently energetic deuterons was deemed excessively large and expensive.

After constructing the world's first superconducting cyclotron in 1982 (the K500, still in service for research as an injector for the larger K1200 superconducting cyclotron completed in 1988) at Michigan State University's National Superconducting Cyclotron Laboratory (NSCL), Henry Blosser and his team designed a more compact cyclotron equipped with superconducting magnets and capable of operating on a rotating gantry[246]. This K100 superconducting cyclotron was built jointly by NSCL and the MedCyc Corporation, commissioned at NSCL in April 1989, and installed the following year at Harper Grace Hospital in Detroit, Michigan[247]. The superconducting magnet produced a field of 4.6 T in the center of the cyclotron and of 5.4 T in the "hill region", with 206 A current in its coils. The coils were potted windings located in a specially designed cryostat that contained liquid He even when the cyclotron was rotated 360° by the gantry. The liquid He consumption was 2.5 l/h with no beam and 6 l/h with a maximum deuterium beam of 15 μA, up to 50 MeV final energy. It was not necessary to extract the beam from the cyclotron, greatly simplifying the design. The neutrons were produced bombarding an internal beryllium target, being collimated and shaped with a specially designed multi-leaf collimator. This cyclotron is shown during the assembly on the gantry in Figure 10.32. Neutron radiotherapy never became a mainstream oncology therapy, but this machine was in clinical operation until 2008, when the neutron radiotherapy program at Harper Grace was discontinued, mainly due to a lack of funding.

As particle therapy slowly gained acceptance as an effective tool fighting cancer, it was realized that treatment can be performed most efficiently in a dedicated, hospital-based facility. In the United States the first such facility was inaugurated at the Loma Linda University Medical Center (LLUMC) in 1990. The accelerator is a synchrotron, designed and built at the Fermi National Accelerator Laboratory, whose first director was R.R. Wilson. This center treats 140–160 patients every day in five treatment rooms, three of them equipped with isocentric gantries. It was generally believed that synchrotrons had certain advantages in particle therapy.

In 1991 IBA, a Belgian company specializing in cyclotron design and fabrication, entered the particle therapy business. They introduced an effective cyclotron design, the C230, and today most particle therapy centers use cyclotron technology. Some of the advantages of cyclotrons are simplicity, reliability, lower cost, smaller size, and the ability to modulate the particle beam current rapidly and accurately, which is required for intensity-modulated particle therapy (IMPT). Since commissioning the first C230 at Massachusetts General Hospital in 2002, IBA has installed a total of 13 additional facilities worldwide, 60% of the total number of commercial proton therapy facilities (30) installed or under construction as of 2009.

[243] C. B. Bingham, J.S. Fraser and H. R. Schneider, Chalk River Nuclear Laboratories Report AECL-4654 (1973)
[244] Mary Catterall and D.D. Vonberg, *Brit. Med. J.* 3 (1974) 137
[245] S. Zink, J. Antoine and F. J. Mahoney, *Am. J. Clin. Oncol.* 12 (1989) 277
[246] H.G. Blosser, et al., *IEEE Trans. Nucl. Sci.* NS-32 (1985) 3287
[247] R.L. Maugan, W.E Powers and H. G. Blosser, *Med. Phys.* 21 (1994) 779

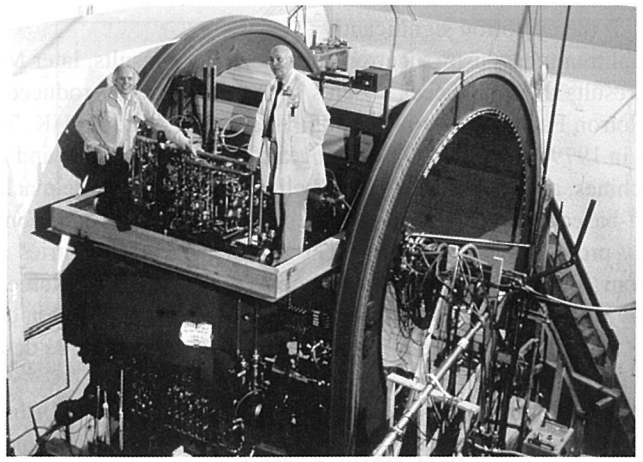

FIGURE 10.32: The K100 superconducting cyclotron during assembly on the rotating gantry at Harper Grace Hospital, Detroit, Michigan. Prof. Henry Blosser, the inventor of the superconducting cyclotrons, is on the left; on the right is Prof. William Powers, the chief physician of the neutron treatment program.

After the successful completion of the Harper Grace Hospital neutron therapy system, the NSCL team led by Prof. Blosser performed a detailed design study of a 250 MeV superconducting cyclotron for proton therapy[248]. This energy is required to reach deep-seated tumors in the human body. This machine was ultimately built by a commercial company, ACCEL, for the Paul Scherrer Institute in Villigen, Switzerland. In parallel, a second unit with gantries and a complete treatment clinic was constructed for the first European commercial proton therapy facility, RPTC, in Munich, Germany. This facility was completed by Varian Medical Systems, which acquired ACCEL in January 2007. The use of superconducting technology in the fabrication of the COMET cyclotron by ACCEL produced an accelerator with considerably less weight and diameter (90 tons, d = 3 m) than the competing IBA room temperature C230 cyclotron (220 tons, d = 4 m), and with decreased electric power consumption[249]. The four cryocoolers used to keep the magnets at liquid He temperature consume 40 kW, compared to the 200 kW needed to operate a similar room-temperature cyclotron. The magnetic field at the center of this cyclotron is 2.4 T, with a 3 T field at the extraction region. The accelerated proton extraction efficiency exceeds 85%, due to a larger pole gap that is enabled by the stronger superconducting magnet. This reduces the unwanted activation of the cyclotron's internal components, allowing for easier maintenance and simpler decommissioning at the end of the useful lifetime of the facility (25–30 years). The machine stays powered overnight, greatly reducing the switch-on time in the morning before patients are treated. This cyclotron is shown in Figure 10.33.

Building on the success of the K100 superconducting cyclotron mounted on a gantry, Henry Blosser began a design study for a 250 MeV proton synchrocyclotron small enough to be mounted on a gantry[250]. An 8 T test magnet was built[251] and demonstrated short–term operation, with plans to transform this magnet to a medical accelerator. This effort was discontinued due to lack of funding, but served as a precursor for a recent project initiated by Timothy Antaya at the Massachusetts Institute of Technology.

In 2003–2004, Blosser introduced a superconducting synchrocyclotron design with a 9 T field for

[248] H.G. Blosser et al. *MSUCL*-874, 1993

[249] D. Krischel, et al., *IEEE Trans. Appl. Supercond.* 17 (2007) 2307

[250] H. G. Blosser, *Nucl. Inst. and Meth.* B40/41 (1989) 1326

[251] J. Kim, et al., *IEEE Trans.Appl. Supercond.* 3 (1993) 266

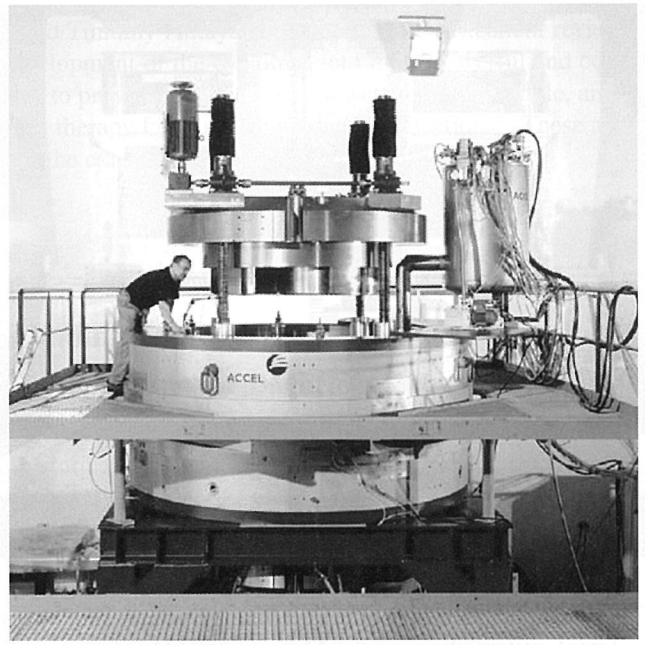

FIGURE 10.33: The COMET superconducting 250 MeV proton cyclotron during the commissioning at the ACCEL facility.

proton beam radiotherapy[252]. This very high field magnet allowed shrinking the mass of the accelerator to less than 25 tons, with an overall diameter of about 1.8 m. This permits mounting the entire synchrocyclotron on a gantry, just as for the K100 neutron therapy machine. A new company, Still Rivers Systems (Littleton, MA.), was formed to commercialize this design. Barnes Jewish Hospital in St. Louis, MO. and the M.D. Anderson Cancer Center in Orlando, FL. have made preliminary commitments to purchase this system, which is anticipated to cost $20M.

A conceptual drawing of the gantry-mounted, high-field 250 MeV proton synchrocyclotron is shown in Figure 10.34. The magnet was successfully tested in February 2009 and the installation was begun in 2010 in the two above-mentioned hospitals. The large cost reduction and single-treatment-room concept will enable many hospitals with existing radiation treatment facilities to procure proton therapy installations. So far the high cost (about $100M–150M for a 3–4 room treatment facility) was the major reason this treatment modality didn't gain wider acceptance in radiation oncology.

Even in the early days of particle therapy it was clear that heavier ions than protons would be more suitable for cancer treatment. Carbon ions were found to be the best compromise between increased relative biological efficiency (RBE) and fragmentation due to nuclear reactions. These ions have a better ratio of the inside/outside of the tumor dose. Due to the larger RBE, they have a smaller lateral scattering in the human tissue compared to protons, making them more suitable to treat deep-seated tumors near sensitive organs, and online dose verification is possible using a positron emission tomography (PET) camera around the patient because a fraction of the ^{12}C projectiles are transformed into ^{11}C, a positron-emitter isotope.

There is considerable evidence for the effectiveness of carbon-ion therapy, mainly accumulated since 1994 at the National Institute of Radiological Science in Chiba, Japan, and the Heavy Ion

[252] T.A. Antaya, US patent no. 7,541,905 B2 (June 2, 2009)

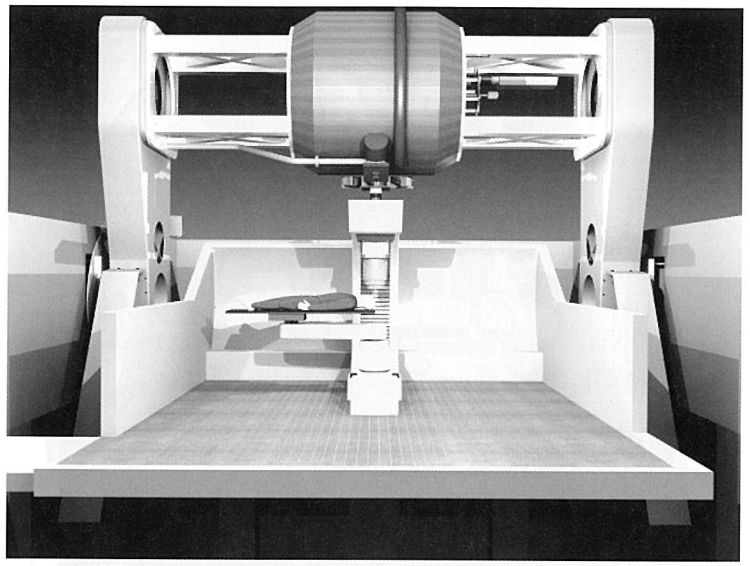

FIGURE 10.34: The conceptual design for the Still Rivers Systems single-treatment-room Proton Beam Radiation Treatment system showing the Monarch250TM mounted on a gantry within the treatment room.

Research Institute, GSI, in Darmstadt, Germany. In all carbon therapy facilities to this day, ions are accelerated by synchrotrons. In order to reach deep-seated tumors, the energy of the carbon ions should be 400 MeV/u, a value not reachable with present medical cyclotrons.

IBA in Belgium has begun the design of a 400 MeV/u superconducting cyclotron in collaboration with physicists from the Joint Institute for Nuclear Research, Dubna, Russia[253]. The main motivation for a cyclotron to produce carbon ions is to reduce the size and the cost of the accelerator, to be able to modulate rapidly the intensity of the ion beam and to have one accelerator instead of three in series, as is the case for synchrotrons, which require a radiofrequency quadrupole (RFQ) magnet and a linear accelerator (LINAC) as injectors. It is expected that in the space and for the cost of a carbon synchrotron, it will be possible to install a cyclotron and a compact carbon gantry, equipped with superconducting dipole magnets. This machine will accelerate ions with Q/A = 1/2 (H^{2+}, He^{2+}, Li^{3+}, B^{5+}, C^{6+}, N^{7+}, O^{8+}, and Ne^{10+}) to 400 MeV/u. The ions will be produced by three external ion sources and will be injected in the cyclotron using an electrostatic spiral inflector. The design of this C400 cyclotron is similar to the IBA C230 proton cyclotron, but with higher magnetic field thanks to superconducting coils, and increased diameter (6.3 m vs. 4.7 m). The C400 cyclotron will operate at fixed energy (400 MeV/u, except for protons at 265 MeV). The energy will be changed in a graphite degrader followed by an electromagnetic energy selector (EES). The nuclear fragments produced during the energy degradation will be eliminated by the EES. Preliminary estimates show that the current on the degrader will be large enough to produce clinically usable beams of ^{11}C, and this would serve for direct, online monitoring with a PET camera of the irradiation received by the patient. The C400 cyclotron will have a magnet with 4 strongly spiraled sectors, 45° at extraction, capable of producing a 4.5 T field on hills and 2.45 T in valleys, and 1.29×10^6 amp-turns produced by superconducting (Nb-Ti) coils. The superconducting coils will have low current density (31.5 Amm^{-2}), with a total stored energy of 60 MJ. The first of these accelerators will be installed in Caen, France, for the ARCHADE Consortium.

[253] Y. Jongen et al. Cyclotrons and Their Applications 2007, Eighteenth International Conference (2007) 151

As Denis Friesel and Timothy Antaya concluded in their excellent review paper on medical cyclotrons[254]: "The development of the cyclotron into more powerful and compact machines is continuing at a rapid pace to provide smaller, more powerful, more flexible, and less expensive isotope production and hadron therapy facilities for medical applications". These advances would not have been possible without the extensive use of superconductors.

10.7 Further Reading

Section 2: Medical Applications of Magnetoencephalography

Several excellent review papers and books have been published on the topic of the present chapter. Some of them are historical landmarks in the field. In some cases, their scope is not restricted to magnetoencephalography but covers the whole field of biomagnetism. In other cases, MEG is presented as an application of SQUID magnetometry. The most recent developments of MEG may be found in the proceedings of the BIOMAG conference published biannually.

1. S.J. Williamson L. Kaufman, Biomagnetism, *J. Magnetism and Magnetic Materials*, 1981, 22, 129-201.

2. Romani G.-L., Williamson S.J., and Kaufman L., Biomagnetic instrumentation, *Rev. Sci. Instr.* 1982, 53, 1815-1845.

3. Hämäläinen M., Hari R., Ilmoniemi R., Knuutila J., and Lounasmaa O., Magnetoencephalography — Theory, instrumentation, and applications to noninvasive studies of the working human brain, *Rev. Mod. Phys.*, 1993, 65, 413-497.

4. Biomagnetism: An Interdisciplinary Approach, NATO ASI series, Williamson S.J., Romani G.-L., Kaufman L., and Modena I. eds., Plenum Press, New York (USA), 1983.

5. SQUID sensors: *Fundamentals, Fabrication and Applications*, NATO ASI series, Weinstock H. ed., Kluwer Academic Publisher, Boston (USA), 1996.

6. *The SQUID Handbook — Fundamentals and Technology of SQUIDs and SQUID Systems*, Clarke J. and Braginski A.I. eds., Wiley-VHC Verlag, Weinheim (Germany), 2004.

Acknowledgements

Section 2: Medical Applications of Magnetoencephalography

The authors are grateful to Laura Marzetti, Filippo Zappasodi and Roberto Guidotti for their assistance in the preparation of this manuscript.

[254] D. L. Friesel and T.A Antaya, *Reviews of Accelerator Science and Technology* 2 (2009) 133

Section 5: Ultralow Field NMR and MRI

I thank Sarah Busch, Erwin Hahn, Bennie ten Haken, Michael Hatridge, SeungKyun Lee, Nathan Kelso, Robert McDermott, Michael Mössle, Michael Mück, Whit Myers, Alex Pines, Jeff Simko, Daniel Slichter, Andreas Trabesinger and Travis Wong for their many contributions. Development of the original NMR and MRI systems was supported by the Director, Office of Science, Office of Basic Energy Sciences, Materials Sciences and Engineering Division, of the U.S. DOE under Contract No. DE-AC02-05CH11231. Acquisition of the ex vivo prostate tissue data was supported by NIH grant R21CA133338.

11

Wires and Tapes

Editor: David Larbalestier

11.1 The Long Road to High Current Density Superconducting Conductors

David Larbalestier

11.1.1 Overview

Multi-tesla, high-field superconducting magnets are possible only when a superconductor can be made into a wire or tape conductor form hundreds of meters or even kilometers long with high current density, acceptable strength, high critical field and affordable price. Thousands of materials are superconducting, yet only six, Nb47wt.%Ti (Section 11.2), Nb_3Sn (11.3), $Bi_2Sr_2CaCu_2O_{8-x}$ and $(Bi,Pb)_2Sr_2Ca_2Cu_3O_{10-x}$ (11.4), $YBa_2Cu_3O_{7-x}$, or more generally any rare-earth (RE) variant of $YBa_2Cu_3O_{7-x}$ (11.5) and MgB_2 (11.6), are available commercially as conductors. Chapter 11 describes many aspects of the development and property evolution in these six conductors, this opening Section 11.1 concentrating on the reasons why the well-developed vision of superconducting magnets of 1913 actually took almost 50 years to implement. It is in many ways a truly remarkable story that intersects with some of the most heartening and terrible aspects of 20^{th} century science and politics. We can define several eras that have governed the development of conductor technology: